

**DETERMINATION OF BACTERIAL CHEMOTAXIS  
RESPONSE FUNCTIONS BY OPTICAL  
TRAPPING**

by

**Tuba Altindal**

B.S. in Physics, Bogazici University, 2003

M.S. in Physics, Bogazici University, 2006

Submitted to the Graduate Faculty of  
the Kenneth P. Dietrich School of Arts and Sciences in partial  
fulfillment

of the requirements for the degree of

**Doctor of Philosophy**

University of Pittsburgh

2012

UNIVERSITY OF PITTSBURGH  
KENNETH P. DIETRICH SCHOOL OF ARTS AND SCIENCES

This dissertation was presented

by

Tuba Altindal

It was defended on

January 23, 2012

and approved by

Xiao-Lun Wu, Department of Physics and Astronomy

Walter I. Goldberg, Department of Physics and Astronomy

Hanna Salman, Department of Physics and Astronomy

Eric S. Swanson, Department of Physics and Astronomy

Robert L. Duda, Department of Biological Sciences

Dissertation Director: Xiao-Lun Wu, Department of Physics and Astronomy

Copyright © by Tuba Altindal  
2012

# DETERMINATION OF BACTERIAL CHEMOTAXIS RESPONSE FUNCTIONS BY OPTICAL TRAPPING

Tuba Altindal, PhD

University of Pittsburgh, 2012

A two-lobe response function is considered as a manifestation of temporal signal comparison in bacterial chemosensing. The second lobe in the response function appears as a result of adaptive behavior of the underlying signaling network, which allows bacteria to stay sensitive over a wide range of background signal levels. It has been argued that this two-lobe response reflects the dual requirements of the bacteria to taxis along a chemical gradient and to localize once the top of the gradient is reached. Calculations based on the run-tumble motility pattern of *Escherichia coli* showed that the second lobe improved the bacterium's localization capability. Intrigued by a recently observed run-reverse-flick motility cycle of a marine bacterium *Vibrio alginolyticus*, we investigate the motility-response relationship in this bacterium. Using a novel optical trapping technique, we measure the response of *V. alginolyticus* to an impulsive stimulus of chemoattractant serine. By exploiting an asymmetry in the rotation of the polar flagellum, we are able to determine for the first time how the bacterium responds to chemical stimuli while swimming forward or backward. Our measurements suggest that this marine bacterium regulates its forward and backward swimming intervals differently, exhibiting behaviors that is consistent with an exploration-exploitation strategy.

In our measurements, we also find that the cell-body  $\Omega(t)$  and the flagellar  $\omega(t)$  rotational angular frequencies oscillate in time and are in synchrony with the forward and backward swimming intervals. Unexpectedly,  $\Omega(t)$  and  $\omega(t)$  are found to be anticorrelated in that the cell body rotates slower in the forward direction than in the backward direction,  $\Omega_f < \Omega_b$ ,

but the flagellum rotates faster in the forward direction than in the backward direction. The change in the rotational load ( $\sim 25\%$ ) is significantly greater than that predicted by flagellum deformation but can be accounted for by the precession of the flagellum about the body axis during the backward swimming interval. We postulate that as a result of the precession, a kink is generated at the base of the flagellum that is subsequently amplified when the flagellum motor reverses direction, leading to the flick, the direction randomization step in *V. alginolyticus*' motility pattern.

## TABLE OF CONTENTS

<b>PREFACE</b> . . . . .	xii
<b>1.0 INTRODUCTION</b> . . . . .	1
1.1 BACTERIAL SWIMMING PATTERNS: RUN-REVERSE-FLICK VS. RUN-TUMBLE . . . . .	2
1.2 BACTERIAL CHEMOTAXIS . . . . .	5
1.3 EXPLORATION AND EXPLOITATION . . . . .	10
<b>2.0 BACTERIAL CHEMOTAXIS IN AN OPTICAL TRAP</b> . . . . .	13
2.1 INTRODUCTION . . . . .	13
2.2 RESULTS . . . . .	14
2.2.1 Bacterial motion in the optical trap . . . . .	14
2.2.2 Characterization of the chemoattractant concentration profile . . . . .	20
2.2.3 The average switching rate . . . . .	23
2.2.4 The time-dependent switching rate . . . . .	25
2.2.4.1 Chemotactic response measurements . . . . .	25
2.2.4.2 Theoretical modeling . . . . .	27
2.2.5 Sensitivity of <i>V. alginolyticus</i> to serine . . . . .	32
2.3 DISCUSSION . . . . .	33
<b>3.0 ADAPTATION IN <i>V. ALGINOLYTICUS</i></b> . . . . .	36
3.0.1 Response of <i>V. alginolyticus</i> to extended exposure to serine . . . . .	36
3.0.2 Analysis . . . . .	38
<b>4.0 IMPLICATIONS OF RUN-REVERSE-FLICK CYCLE IN BACTERIAL CHEMOTAXIS</b> . . . . .	42

4.1	INTRODUCTION . . . . .	42
4.2	RESULTS . . . . .	46
	4.2.1 Independent Chemosensing . . . . .	50
	4.2.2 Shared Chemosensing . . . . .	51
4.3	DISCUSSION . . . . .	53
<b>5.0</b>	<b>ASYMMETRIC RESPONSES OF FORWARD AND BACKWARD SWIMMERS . . . . .</b>	<b>58</b>
5.1	INTRODUCTION . . . . .	58
5.2	THEORY . . . . .	61
5.3	RESULTS . . . . .	65
	5.3.1 Unconditioned switching rate measurements . . . . .	65
	5.3.2 Conditional statistics and motor rotational bias . . . . .	67
	5.3.3 <i>V. alginolyticus</i> employ independent chemosensing . . . . .	77
	5.3.4 Difference between $k_f(t)$ and $k_b(t)$ persists in the case of longer exposure to serine . . . . .	83
5.4	DISCUSSION . . . . .	85
	5.4.1 Important features of the response functions are predictable based on <i>V. alginolyticus</i> motility pattern . . . . .	85
	5.4.2 Independent sensing of 3-step swimmers enables an exploration-exploitation behavior . . . . .	87
	5.4.3 The measured response has strong implications for how the chemotaxis network is wired in <i>V. alginolyticus</i> . . . . .	88
	5.4.4 Chemotactic response is conserved in <i>V. alginolyticus</i> and in <i>E. coli</i> . . . . .	90
5.5	CONCLUSION . . . . .	91
<b>6.0</b>	<b>SYMMETRY PROPERTIES OF BACTERIAL POLAR FLAGELLAR MOTORS . . . . .</b>	<b>93</b>
6.1	INTRODUCTION . . . . .	93
6.2	RESULTS . . . . .	95
	6.2.1 Cell body and flagellar rotation frequencies in different swimming intervals . . . . .	95

6.2.2	Asymmetries in the forward and the backward propulsion . . . . .	99
6.2.3	Bias of flagellar motors in de-energized bacteria . . . . .	102
6.2.4	Unusual motions of tethered <i>V. alginolyticus</i> bacteria . . . . .	104
6.3	THEORETICAL ANALYSIS . . . . .	111
6.3.1	Deformation of flagellum in <i>V. alginolyticus</i> cannot account for the large difference in $D_f$ and $D_b$ . . . . .	111
6.3.2	Precession of flagellum during backward swimming . . . . .	116
6.4	DISCUSSION . . . . .	119
<b>APPENDIX A. MATERIALS AND METHODS . . . . .</b>		<b>123</b>
A.1	Bacterial strains and culture conditions . . . . .	123
A.2	Optical trap and measurement procedures . . . . .	123
A.3	Creation of a localized chemical gradient . . . . .	127
A.4	Tracking of free-swimming cells . . . . .	127
A.5	Video imaging of stuck cells . . . . .	128
<b>APPENDIX B. CALCULATION OF THE MEAN DISPLACEMENT . . . . .</b>		<b>129</b>
<b>APPENDIX C. OPTIMIZATION OF THE DRIFT VELOCITY . . . . .</b>		<b>134</b>
<b>APPENDIX D. WHAT DO WE KNOW ABOUT FLAGELLAR MOTOR SWITCHES? . . . . .</b>		<b>136</b>
<b>APPENDIX E. FORCE AND TORQUE DUE TO TILTING OF THE BAC- TERIAL FLAGELLUM . . . . .</b>		<b>138</b>
<b>BIBLIOGRAPHY . . . . .</b>		<b>140</b>

## LIST OF TABLES

3.1	Response amplitudes . . . . .	41
6.1	Statistics of rotation angular frequencies . . . . .	99
6.2	Statistics of the asymmetry in polar flagellar motors of <i>V. alginolyticus</i> . . . . .	102
6.3	Parameters for calculating flagellar deformation . . . . .	114

## LIST OF FIGURES

1.1 Visualization of flicking . . . . .	4
1.2 <i>E. coli</i> 's chemotactic signaling pathway . . . . .	7
1.3 Perfect adaptation . . . . .	9
1.4 Exploration and exploitation phases of bacterial foraging . . . . .	11
2.1 Probing bacterial chemotactic response with an optical tweezers . . . . .	15
2.2 Experimental setup . . . . .	17
2.3 Bacterial positions in the optical trap . . . . .	18
2.4 Lissajous figures of bacterial trajectories in the optical trap . . . . .	19
2.5 Two rotation states of bacterial flagellar motor in the optical trap . . . . .	21
2.6 The chemoattractant concentration profile . . . . .	24
2.7 Normalized cumulative distribution functions (CDFs) . . . . .	28
2.8 The time-dependent switching rate of <i>V. alginolyticus</i> . . . . .	29
2.9 The response amplitude $R'_0$ vs. serine concentration $c_0$ . . . . .	34
3.1 Experimental timescales . . . . .	37
3.2 Response of <i>V. alginolyticus</i> to the extended exposure to serine . . . . .	39
4.1 Bacterial swimming trajectories . . . . .	45
4.2 Migration of <i>V. alginolyticus</i> in a linear chemical gradient . . . . .	49
4.3 Chemotactic strategy I . . . . .	52
4.4 Chemotactic strategy II . . . . .	54
5.1 Response functions for independent and shared chemosensing revisited . . . . .	60
5.2 Drift velocity ratio for independent and shared chemosensing . . . . .	64
5.3 Experimental setup and signal processing . . . . .	69

5.4	Forward and backward dwell time distributions . . . . .	71
5.5	Pure ensemble measurements . . . . .	73
5.6	Mixed ensemble measurements . . . . .	76
5.7	Amplitudes of the non-dimensional response functions . . . . .	82
5.8	Mixed ensemble measurements for prolonged exposure to serine . . . . .	84
6.1	Simultaneous measurements of the cell-body $\Omega(t)$ and the flagellar $\omega(t)$ rotational frequencies . . . . .	97
6.2	Correlations between cell-body and flagellum rotations . . . . .	98
6.3	Probability density functions (PDFs) of angular frequencies and their ratios .	100
6.4	Swimming velocity, motor power, and rotation load PDFs . . . . .	103
6.5	An hypothetical stretchable component in the flagellar motor of <i>V. alginolyticus</i>	107
6.6	Case I: A horizontally tethered cell . . . . .	108
6.7	Case II: A nearly vertically tethered bacterium . . . . .	109
6.8	Case III: A vertically tethered bacterium . . . . .	110
6.9	Effect of flagellum deformation on bacterial swimming . . . . .	115
6.10	States of flagellum rotation in optical trap . . . . .	117
6.11	Torque-speed relation and motor asymmetry of <i>V.alginolyticus</i> ' polar flagellar motor . . . . .	121

## PREFACE

There is a bunch of people I would like to thank for their contributions to this dissertation and more importantly, to my academic development. Of course, my beloved advisor Xiao-Lun Wu has the lion's share. I am grateful to him for teaching me that progress will be possible only if I reach certain mental flexibility that would help me to see the full half of a half-filled glass.

I would also like to thank my valued committee members Walter Goldberg, Hanna Salman, Bob Duda and Eric Swanson. Walter, with his passion for scientific research and incredible energy, has always been an inspiration to me. I am grateful to him for never getting tired of asking the very same questions about the significance of this research which helped me a lot in grasping the essence of my work. I am also deeply grateful to Bob who has never left me alone in my effort to modify *Vibrio* genetically. Likewise, Hanna and Eric, with their suggestions helped me to improve my research to a great deal.

I would also like to express my gratitude to the senior members of our lab Emily Chapman Mcquiston and Suddhashil Chattopadhyay who taught me everything I needed to get started in the lab. I am indebted to my colleague, dear friend Li Xie, for helping me out whenever I needed her assistance and the relief she brought at the times of misery. I would also like to thank Ildoo Kim, Jing He, Rory Cerbus and Stefanus for their help.

## 1.0 INTRODUCTION

Microorganisms face many challenges in their natural habitats, and they develop different strategies to adapt to the environment they live in. One of the challenges for these microorganisms is to identify what is good or bad for them and to respond appropriately. Thus far the best studied case is the chemotactic behavior of enteric bacterium *Escherichia coli* [53, 64, 15, 18, 74]. This bacterium uses the run-tumble swimming pattern to navigate in an environment, i.e., when the temporal signal is favorable to the bacterium the run interval is lengthened, but when the signal is unfavorable the run interval is shortened [13]. By regulating the length of the swimming intervals, the bacterium executes a biased random walk, directing towards the source of attractant or away from a repellent. However, not all bacteria live in conditions similar to *E. coli*, and it is of great scientific interest to learn and understand how other diverse bacterial species handle challenges in a variety of environments.

This thesis is about our investigation of chemotactic behaviors of *Vibrio alginolyticus*. This bacterium lives in ocean, but it has much in common with *E. coli* such as its physical size, its metabolic needs, and its motility being also powered by rotary motors that rotate either in the counterclockwise (CCW) or clockwise (CW) direction. Unlike *E. coli*, however, the flagellar motor of *V. alginolyticus* is more powerful, which can rotate at an angular frequency of a few kilohertz, pushing the cell body at a speed  $\sim 200 \mu\text{m/s}$  [58]. These values are nearly ten times of those typically seen in *E. coli* [25, 23], perhaps reflecting different physiological requirements for the two bacteria to inhabit different environments. Another significant difference between the two bacteria is that *V. alginolyticus* possesses only a single polar flagellum when it is grown in a liquid medium [2]. For the two-state motor, this suggests that the forward (CCW) and the backward (CW) swimming paths are time-reversal

symmetric when the motor reverses its direction [69]. Our recent observations, however, show that *V. alginolyticus* incorporate an additional movement, which we call a flick, that randomizes cells' swimming trajectories [92]. In the light of these physiological differences (polar vs. peritrichous flagellation) and their varied motility patterns, one wonders if there are also differences in the way the flagellar motors are regulated by the internal chemotaxis networks of these two bacteria.

We developed an optical trapping technique to investigate the chemotactic behavior of *V. alginolyticus* [4]. The technique takes advantage of the fact that the bacterium has only a single polar flagellum, and the two rotation states of the motor can be readily and instantaneously resolved in the optical trap. This allows the flagellar motor switching rate  $S(t)$  and the CCW bias  $\Phi(t)$  to be measured under different chemical stimulations.

## 1.1 BACTERIAL SWIMMING PATTERNS: RUN-REVERSE-FLICK VS. RUN-TUMBLE

A typical bacterium has a dimension  $L$  of a few microns and swims at a speed  $V$  of tens to hundreds of microns per second, which make them low Reynolds number (Re) swimmers with  $Re(=VL/\nu) \simeq 10^{-5} - 10^{-4}$ , where  $\nu \simeq 10^{-2} \text{ cm}^2/\text{s}$  is the kinematic viscosity of water. The bacterial swimming is therefore governed by the Stokes equation that is time-reversal invariant. Thus, a bacterium that tries to swim by a “reciprocal motion”, i.e., by undergoing a deformation and recovering its original shape through the same sequence in reverse, cannot go anywhere. However, a helical flagellum lets bacteria bypass such a reciprocal motion and enables swimming at low Re [69]. Due to its handedness, the rotation of the helix is intrinsically coupled to its translation, i.e., it can function as a propeller. The thrust force generated by the flagellum can push or pull the cell body, enabling the cell to move about in a fluid. Because it is free-body swimming (free of external forces) the net force and torque on the bacterium must be zero, suggesting that (a) the thrust force produced by the flagellum must be balanced by viscous drag on the cell body and on the flagellum, and (b) the flagellum and the cell body must rotate in opposite directions.

The flagellum is driven by a rotary motor embedded in the bacterial membrane. The motor transduces electrochemical energy (membrane potential and ion concentration gradient) into mechanical energy by means of ions flowing through the motor. The flagellar motors of *E. coli* and *V. alginolyticus* are bidirectional, and the sense of motor rotation is determined by the internal chemotaxis network, which will be discussed below.

Different species of bacteria have different numbers and arrangements of flagella. Enteric bacterium *E. coli* is peritrichously flagellated, i.e., it has multiple flagella that are randomly distributed over its body. Since *E. coli*'s flagella are left-handed, when the flagellar motors all rotate in the CCW direction, the flagella form a bundle and push the bacterium forward [12]. The bundle falls apart when one or more motors rotate in the CW direction, and the bacterium tumbles, producing no net displacement [54]. When the flagella rebundle, the cell swims in a new direction. Hence, the motion of *E. coli* can be abstracted as a random walk. By modulating the CCW and CW durations according to extracellular chemical cues, the cells bias their random walk so as to move toward attractants and away from repellents [13].

*V. alginolyticus* has two distinct flagellar systems, the polar and the lateral ones. When grown in a low-viscosity medium, such as in a liquid, the bacterium produces only a single polar flagellum as illustrated in Figure 1.1. If the viscosity of the environment increases, the polar flagellar motor senses this change and triggers the expression of the lateral flagellar system [42]. Although the underlying mechanism for mechanosensing is unknown, it is established that the polar flagellum has an essential role in the transition from the swimmer phenotype to swarmer phenotype [42]. This thesis only deals with the swimmer phenotype. Being single polarly flagellated, low Re hydrodynamics dictates that aside from randomness introduced by thermal fluctuations the bacterium can only backtrack its trajectory when the motor reverses. This raises an interesting question concerning how this polar flagellated bacterium performs chemotaxis.

We found that *V. alginolyticus* employ a unique cyclic three-step (run-reverse-flick) swimming pattern. The time-reversal symmetric trajectories in the consecutive forward and the backward swimming intervals are randomized by the last step, where the flick “steers” the cell to a new direction. Figure 1.1 displays a cell that is labeled with a reagent (NanoOrange) that fluoresces upon interacting with proteins. The technique enables visualization of the

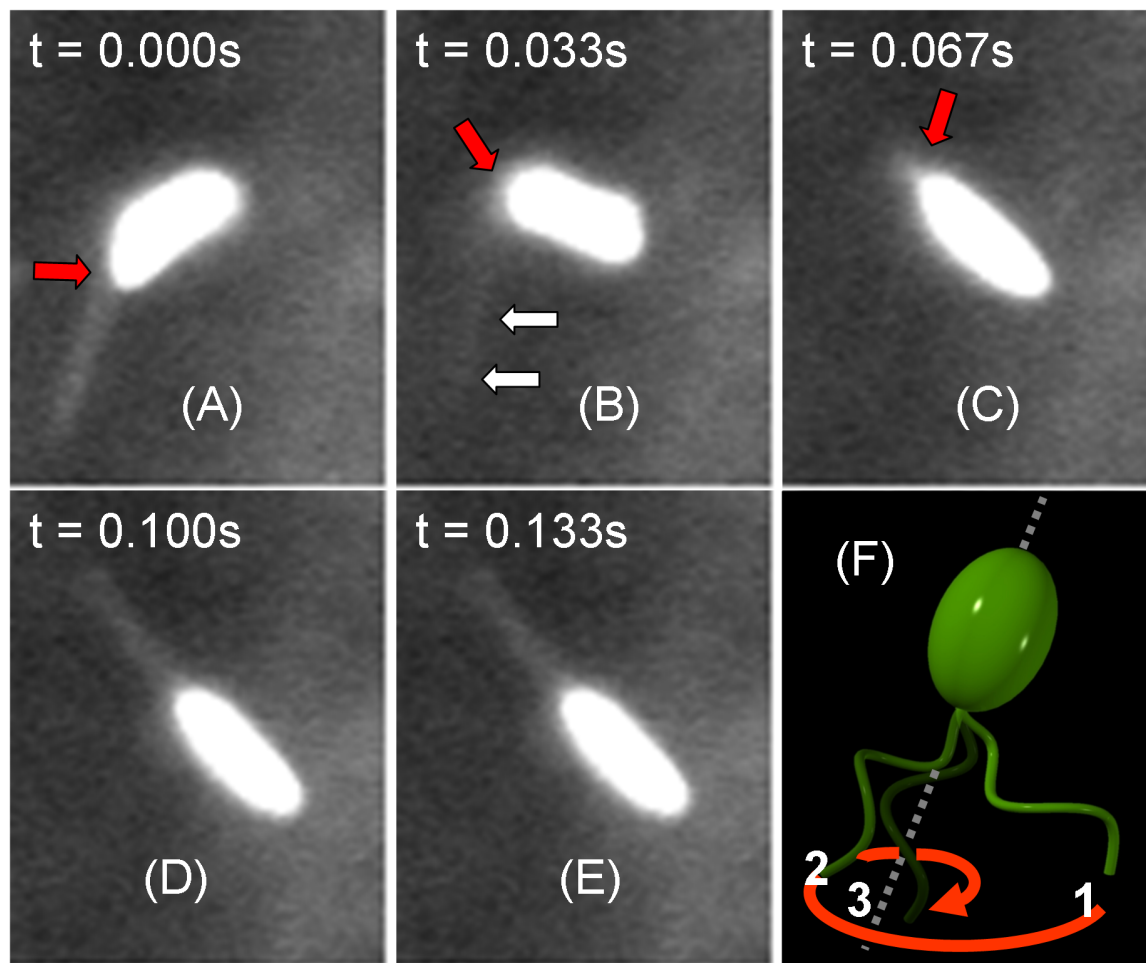


Figure 1.1: Visualization of flicking

flagellum. However, because of its rapid rotation, the fine helical structure is blurred on these images. These fluorescent images demonstrate that upon switching from backward to forward swimming, the flagellum and the cell body are not coaxial, and a small kink forms between them as depicted in (A). This small kink is rapidly amplified by the CCW rotation of the flagellar motor that pushes the cell body at an angle. As shown in (B) and (C), the angular amplification is rapid and efficient; i.e., the cell rotates by  $\sim 90^\circ$  in less than 0.1 s while its center of mass translates only approximately one-half of its body length. After the new direction is selected, the flagellum aligns with the cell body axis via a large swing with its tip tracing out a hyperbolic spiral. As this swinging motion throws the flagellum out of the focal plane, it fades out of view as is evident in (C). This last step in the flicking process is depicted schematically in (F). The entire flicking process includes initiation, amplification, and flagellum alignment. In Chapter 6, a possible mechanism for the kink formation will be discussed, which is motivated by interesting observations made when *V. alginolyticus* are trapped in optical tweezers.

## 1.2 BACTERIAL CHEMOTAXIS

The sensory kinases and their associated response regulators constitute the core of most signal-transducing pathways and are called the two-component signal transduction. A sequence of phosphorylation reactions enables the flow of information from an environment to response-producing components, such as the flagellar motor or a promoter of a gene [90, 83]. By transferring its phosphoryl group to the response regulator, the phosphorylated kinase regulates the interaction between the response regulator and the response-producing components. Bacterial chemotaxis signaling pathways are likewise built on the two-component system. Bacteria sense environmental changes through their receptors that are located at the poles of their rod-like body [1, 55]. These receptors are also called the methyl-accepting chemotaxis proteins (MCPs) for a reason that will become clear below. The periplasmic domain of the chemotaxis receptors bind to signaling molecules such as oxygen, amino acids, peptides, and sugars. The MCPs are linked to the autokinase CheA via a structural protein

CheW. The activity of CheA is modulated by the binding-unbinding of signaling molecules. In particular, the binding (unbinding) of chemoattractants (chemorepellents) suppresses the autokinase activity while the binding (unbinding) of chemorepellents (chemoattractants) enhances it. The autophosphorylated CheA transfers its phosphoryl group to the response regulator CheY. The existing experimental evidence shows that only the phosphorylated form of CheY is able to bind to the flagellar motor, but its effect on the motor is different between species and sometimes even between different flagellar systems of the same species [47]. In *E. coli*, the binding of CheY-P to the flagellar motor biases its CW rotation, forcing the bacterium to change direction when moving down the chemoattractant gradient [90]. For a two-component system, the termination of the signal (dephosphorylation) is just as important as the activation (phosphorylation) of the response regulator. Otherwise, over time the concentration of the response regulator (CheY-P) would increase and would not be able to respond coherently to changes in the external environment. In bacterial chemotaxis, the phosphodiesterase CheZ is responsible for signal termination; it inactivates the response regulator by removing its phosphoryl group [21].

Even though the two-component system described above is sufficient to produce coherent responses to extracellular environments, the bacterial chemotaxis networks can do better by incorporating additional features. For a bacterium that is searching for good places what matters is the temporal change in the chemical level rather than its absolute value. Systems without memory cannot make comparisons. In bacterial chemotaxis the information acquired in the past is registered by the methylation level on the receptors [80]. Two counteracting enzymes are responsible for this memory process: The methyltransferase CheR adds methyl groups to the methyl accepting domains of the receptors (called a methylation process), whereas the methylesterase CheB removes them (called a demethylation process). In *E. coli*, CheB needs to be phosphorylated to become active and therefore it competes with CheY for phosphorylation by CheA. The activity of the MCPs is determined by both the methylation level  $m$ , i.e. the number of methyl groups on them, and the extracellular signal  $[L]$ , the chemoeffector concentration. In particular, the receptor activity  $a$  increases with  $m$ . If one assumes that CheR only methylates inactive receptors and CheB only demethylates active receptors and the rate of (de)methylation depends on  $a$  but not on  $m$  or  $[L]$  [9], the

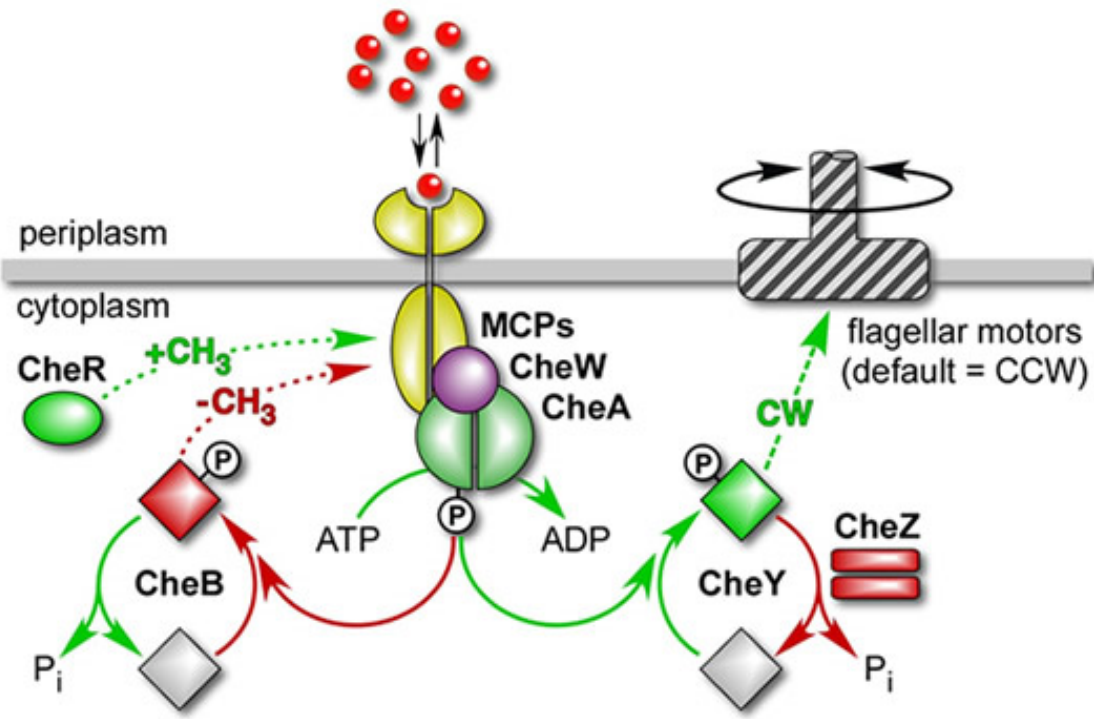


Figure 1.2: *E. coli*'s chemotactic signaling pathway. From Parkinson Lab website.

Michaelis-Menten kinetics leads to the net methylation rate,

$$\begin{aligned} \frac{dm}{dt} &= F(a) \\ &= \frac{V_R(1-a)}{K_R + (1-a)} - \frac{V_B(a)a}{K_B + a}, \end{aligned} \tag{1.1}$$

where  $a$  can be thought of as the fraction of active receptors in a bacterium,  $V_{R(B)}$  are the (de)methylation rate constants and  $K_{R(B)}$  are the Michaelis-Menten constants for the (de)methylation reactions. For moderate values of  $V_{R(B)}$  and  $K_{R(B)}$ ,  $F(a)$  would have a functional form similar to the one depicted in Figure 1.3(A). Perfect adaptation appears as a natural consequence of the fact that  $F(a)$  has a global fixed point at  $a = a_0$  where  $F(a_0) = 0$ , and since  $F(a)$  is a monotonically decreasing function of  $a$  (i.e.  $F'(a) < 0$ ) and  $a$  increases with  $m$  (i.e.  $da/dm > 0$ ), this fixed point is globally stable. Hence, over a long time the system always recovers its steady state activity with  $a = a_0$  as delineated in Figure 1.3(B). Adaptation is an indispensable feature of the bacterial chemotaxis network as is for other sensory systems. It allows the system to stay sensitive over a wide range of background chemoeffector concentrations.

In the adaptive network described above, upon a brief stimulation with a chemoattractant, the response regulator concentration initially drops down and then gradually recovers its steady-state level. However, it overshoots before relaxing back to the steady-state level giving rise to a positive lobe in the response function  $R(t)$  as depicted in Figure 4.1(C) of Chapter 4. Interestingly, the positive and the negative lobes of the response function have equal area, that is,  $R(t)$  integrates to zero over time [86]. This two-lobe response function was recognized by Block, Segall and Berg, the original investigators of the phenomenon, as the bacterium's means of sensing [18]. The presence of the two lobes indicates that the bacterium compares the information received in the recent past to that received earlier. Besides, the null integral shows that an efficient sensing of the gradients is achieved by filtering out the low-frequency variations in the chemical concentration.

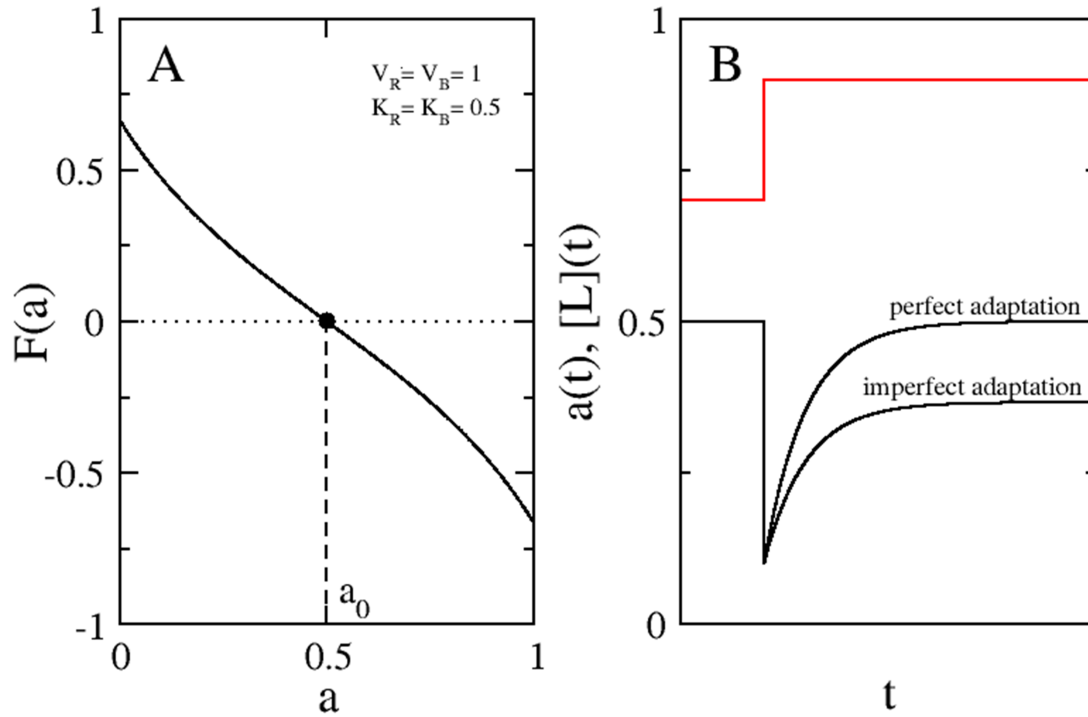


Figure 1.3: Perfect adaptation. In (A), the net methylation rate  $F(a)$  is plotted as a function of the receptor activity  $a$ . For the chosen parameters  $V_R = V_B = 1$  and  $K_R = K_B = 0.5$ , the globally stable fixed point occurs at  $a_0 = 0.5$ . (B) delineates how  $a(t)$  (the black curves) relaxes back to a steady-state level after a step stimulation with chemoattractant (the red broken line).

### 1.3 EXPLORATION AND EXPLOITATION

Motility and signal transduction in bacteria are delineated above in Sections 1.1 and 1.2. The swimming pattern and its regulation determine the bacterial chemotactic search strategy. Of these two aspects of the bacterial chemotaxis, the former can be thought of as the cell’s “hardware” and the latter as its “software”. Here, the critical question is how the distinctive features of the hardware influence the wiring of the software, if it does at all. Such hardware-software relationships deserve studying because it enables us to learn how microorganisms diversify their behaviors by developing niches in different environments, and how laws of physics constrain their evolution.

The main difference between *E. coli*’s and *V. alginolyticus*’ motility is that the CW rotation of the flagellar motor produces no motility for *E. coli* but it does for *V. alginolyticus*. The net effect is that the CW motor rotation causes *V. alginolyticus* to backtrack its previous path but *E. coli* cannot. This seemingly small difference is physiologically significant because *E. coli*’s run-tumble motility pattern determines that it is heavily weighted on exploration. Like a reckless gambler, *E. coli* makes a bet on each tumbling interval, and information attained during the previous run interval cannot be used in subsequent runs. On the other hand, *V. alginolyticus*’ motility pattern appears to be more purposeful; it explores its environment while swimming forward, and then uses the backward interval to reap what it has found. In this sense, we may consider *V. alginolyticus*’ forward run as the “exploration” and its backward run as the “exploitation”. The direction randomization by a flick, which is functionally equivalent to a tumble in *E. coli*, is implemented only after the exploration and exploitation phases are completed. The different search strategies of *E. coli* and *V. alginolyticus* are illustrated schematically in Figure 1.4.

In an aqueous habitat, two extreme cases of nutrient distributions exist. In one, the fluid is quiescent and nutrients are sporadically distributed in small patches. In the other, turbulence stirs up the fluid, giving rise to striated distribution of nutrients as depicted in Figure 1.4. We believe that the run-reverse-flick cycle, commonly seen in marine bacterial species, allows them to deal with both of these cases better than the run-tumble cycle. Particularly, backtracking appears to be beneficial as it enhances nutrient uptake by allowing

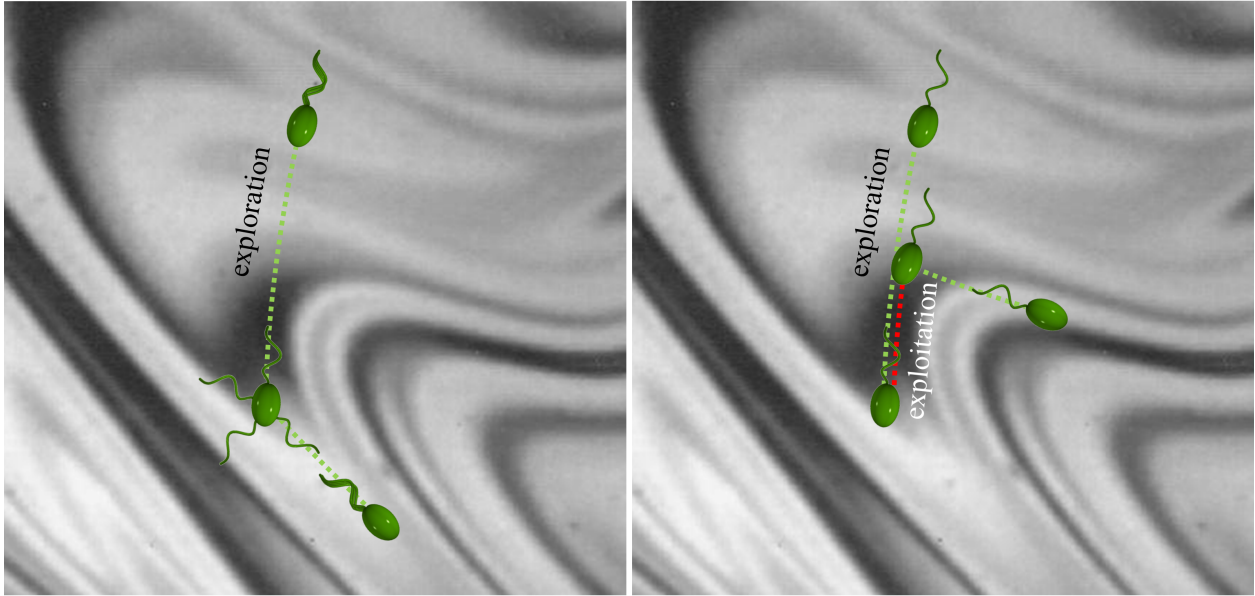


Figure 1.4: Exploration and exploitation phases of bacterial foraging

the cells to exploit the resources they have recently found in the forward swimming (see Figure 1.4). The work presented here is inspired by the new features of *V. alginolyticus*' swimming cycle [92]. In Chapter 5, we report an experiment designed to directly measure the response function of *V. alginolyticus* when the bacterium is either in the forward and backward swimming intervals. Indeed, our finding suggests that this exploration-exploitation strategy is hardwired in *V. alginolyticus*' chemotaxis network.

This thesis is organized as follows. In Chapter 2, we describe measurements of the response of *V. alginolyticus* to an impulse stimulation with chemoattractant serine. These measurements require establishment of a well-defined stable concentration profile. We describe how we created the concentration profile and characterize it using an injection-diffusion model. We discuss how the bacterial motion is detected in the optical trap. The tools used in data analysis are also described in this chapter. In Chapter 3, we describe the response measurements of *V. alginolyticus* to extended exposure to serine, allowing us to determine how cells adapt to a prolonged signal. In Chapter 4, we present a calculation of the mi-

gration speed of a cell executing the 3-step pattern in a linear chemical gradient. We also calculate the optimal responses in the forward and the backward intervals that maximize the drift velocity in a linear gradient. Here, independent and shared chemosensing are proposed as two distinct scenarios for bacterial chemosensing in *V. alginolyticus*. In Chapter 5, we report our effort to identify the motor rotation state in the optical trap. This allows us to determine bacterial response to an impulsive stimulus conditioned on their motor state. The measurements reveal for the first time that *V. alginolyticus* uses independent chemosensing to regulate the forward and the backward intervals. We also discuss the implications of the observed responses on the search strategy of *V. alginolyticus*. Finally in Chapter 6, we provide an explanation for the asymmetric changes in the cell-body and the flagellar rotation frequencies observed in the optical trap and the erratic movements of stuck cells captured by video imaging. Their possible connection to the kink formation, which leads to a flick at the end of the CW interval, is also discussed.

## 2.0 BACTERIAL CHEMOTAXIS IN AN OPTICAL TRAP

### 2.1 INTRODUCTION

A major difficulty in studying chemotactic behavior of *V. alginolyticus* is that the classical rotation assay [75, 15] that has been used successfully for *E. coli* cannot be reliably applied to this marine bacterium. This perhaps is due to the membrane sheath that covers the flagellum, making it difficult to tether to a substrate [33]. We overcame this difficulty by developing an optical trapping technique to monitor the rotation of the flagellar motor [23]. The optical trap can hold the bacterium in place without restricting its rotational motion. As illustrated in Figures 2.1(A-C), the trapped bacterium can be forced to move in a homogeneous medium (A), towards a chemical source (B), or away from it (C), while the state of motor rotation is monitored continuously at a high rate by a photo-diode. The measurements can achieve a high signal-to-noise ratio owing to the fact that *V. alginolyticus* has a single polar flagellum such that rotation of the cell body reacts instantaneously to the flagellum rotation. By way of introduction, Figures 2.1(D, E) display the response of a bacterium when subjected to the manipulations as described in Figures 2.1(A-C). The chemical source in this case is created by a micropipette filled with 1 mM of serine, which is an attractant to *V. alginolyticus*, and the flagellar angular displacement (or the winding angle)  $\phi = \int^t \omega(t') dt'$  is recorded as a function of time  $t$ , where  $\omega$  is the angular velocity of the flagellum. As shown, when the bacterium is in a homogeneous medium, which can be called a steady state, the winding angle  $\phi$  fluctuates in time, giving rise to a saw-tooth functional form as displayed by the blue curve in (D). When the cell is moved towards the source,  $\phi$  increases steadily, indicating no motor switching as displayed by the green line in (E). In contrast, when the cell is moved away from the source,  $\phi$  fluctuates wildly as illustrated by the red curve in (E). The motor

reversal is almost instantaneous, i.e., within the resolution of our measurement, no obvious delays or pauses can be detected during a reversal. The above measurements can be repeated for a large number of bacteria, which allow the time-dependent switching rate  $S(t)$  to be determined after an ensemble average.

A nice feature of our technique is that it permits experimenters to design paths for a cell so that the chemical signal  $c(t)$  it receives can be predetermined. This potentially enables detailed studies of bacterial chemotactic response to a variety of stimulation patterns that have only been achieved in tethered *E. coli* cells with the help of a programmable mixing apparatus [18]. Our optical trapping technique is general, since it does not rely on cell tethering, and therefore should be applicable to different bacterial species.

Here, we investigated the simplest stimulation, where  $c(t)$  is approximately  $\delta$  in time and its amplitude was varied systematically. We found that the response of the bacterium is biphasic in a manner similar to *E. coli*. However, the excitation time  $\tau_e$  and the adaption time  $\tau_a$  are both very short with  $\tau_e \simeq \tau_a \simeq 0.5$ s. Biologically, these time scales may be associated with the dephosphorylation time  $\tau_z$  of response regulators CheY-P and the methylation time  $\tau_m$  of chemoreceptors (or MCPs), similar to *E. coli*. Thus, an important finding of this experiment is that upon a brief stimulation, the chemotaxis network of *V. alginolyticus* appears to employ only a single time scale for chemosensing.

## 2.2 RESULTS

### 2.2.1 Bacterial motion in the optical trap

Our measurements were carried out in a home-built optical tweezers (see Figure 2.2(A)), which has been described in detail in Ref. [23]. A brief description of the setup is also provided in Appendix A.2. Using radiation pressure from a tightly focused infrared laser, a bacterium can be held in place or be moved about without restricting its rotational degrees of freedom. The cylindrical shape of the bacterium ensures that once trapped, its cell body is aligned with the optical axis of the trap as illustrated in Figures 2.2(C-F). Waves due to

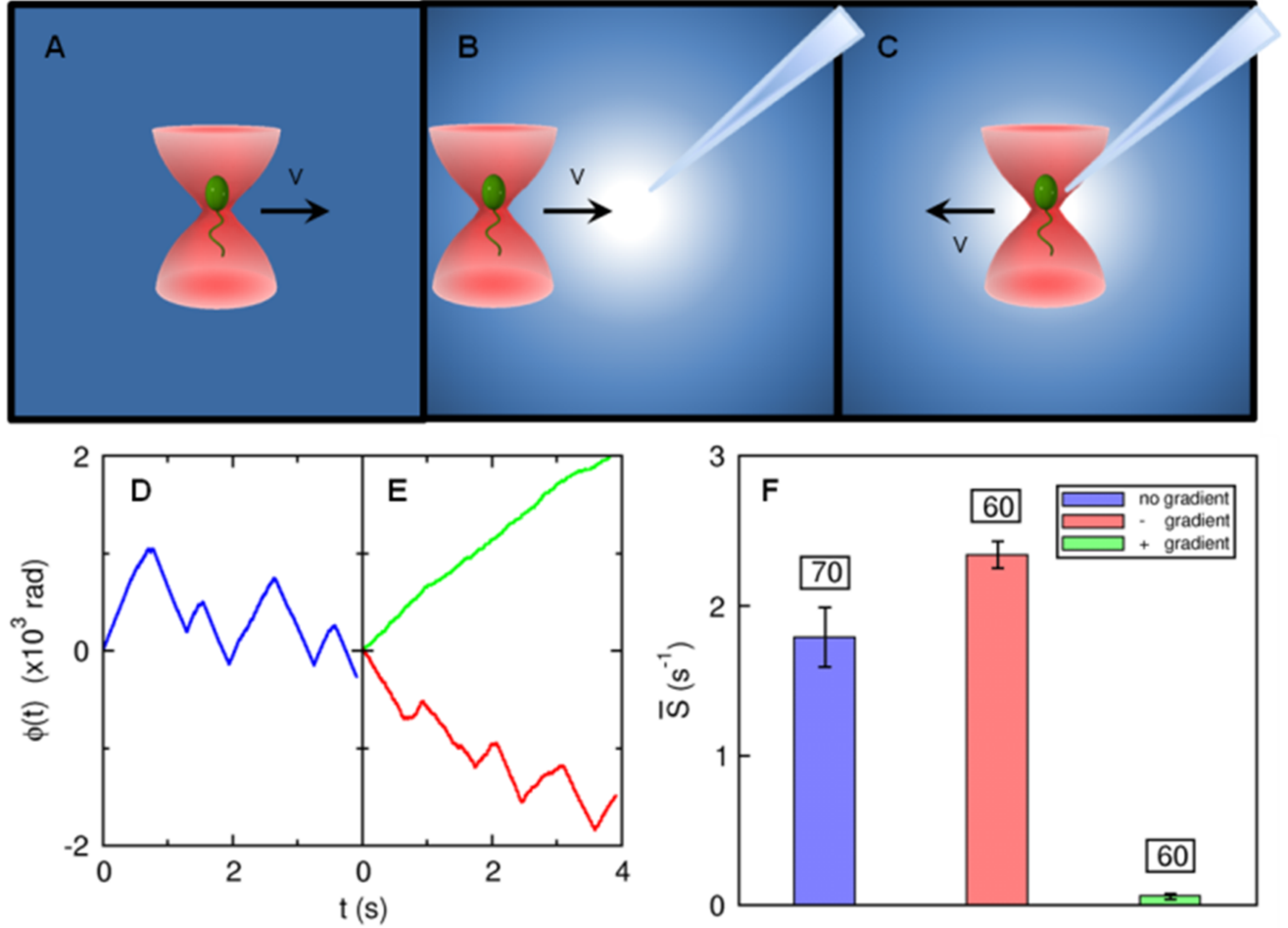


Figure 2.1: Probing bacterial chemotactic response with an optical tweezers. To investigate cell's response to a chemoattractant gradient, a micropipette filled with 1 mM of serine was used. The concentration profile is determined by molecular diffusion [34]. (A) is a control experiment in which a *V. alginolyticus* cell was dragged at a speed  $v = 30 \mu\text{m/s}$  in a uniform TMN buffer to obtain its steady-state switching rate. In (B), the cell was trapped  $\sim 120 \mu\text{m}$  away from the tip and then dragged towards it for 4 s at the same speed. In (C), a cell was initially trapped at a distance  $5 \mu\text{m}$  from the tip and was then dragged away from it for 4 s at the same speed. In (D), the flagellar motor rotation angle (or the winding angle) as a function of time  $\phi(t)$  is measured in the optical trap when the trapped cell was moved in the motility buffer without chemoattractant. In (E), the bacterium was moved towards (green) and away from (red curve) the source of attractant. In the homogeneous medium (D), the motor reverses its direction roughly once every 0.5 s. However, when the cell is moving up the gradient (green in (E)) the motor reversal is completely suppressed. When the same cell was moved down the gradient, frequent motor reversals from  $\text{CW} \Leftrightarrow \text{CCW}$  were again observed. In (F), the average switching rates  $\bar{S}$  for the three different stimuli are displayed. The blue bar is for the steady-state case, while the green and the red bars are for cells moving up and down the gradient, respectively. We noticed that there was only a small difference when the cell was forced to move away from the source compared to the steady-state case. The error bars are standard errors of the mean calculated based on the cell numbers indicated above the bars.

flagellar rotation propagate along the cell body, causing its center of mass position  $(x(t), y(t))$  to fluctuate, which can be interrogated using a two-dimensional position sensitive detector (PSD). Figure 2.3(A) displays a typical time trace  $(x(t), y(t))$  for a trapped bacterium. The bacterial trajectory in the optical trap is concentrated in two lobes, which correspond to the rotational states of the motor (see more discussions below). A short segment in one of the lobes is plotted against time as displayed in (B) for  $x(t)$  and  $y(t)$ , corresponding to the black and red curves, respectively. The power spectra  $E_x(f)$  and  $E_y(f)$ , corresponding to fluctuations in  $x(t)$  and  $y(t)$ , are given in (C). Here, one observes two sharp peaks located at  $f_L \simeq 80$  Hz and  $f_H \simeq 520$  Hz. These frequencies are due to the rotation of the cell body  $\Omega = 2\pi f_L$  and the flagellum  $\omega = 2\pi f_H$ , respectively. One can apply band-pass filters (see dotted green curves) to extract the slow and the fast rotations of the cell body as depicted in Figure 2.3(C). We applied Gaussian filters that are centered at the peaks and with a width of 15% of the peak frequency. One observes in Figure 2.3(D) that after filtering the slow cell-body rotation and the fast flagellum rotation are rather regular. Moreover, there is a phase difference between  $x(t)$  and  $y(t)$  traces, and this phase difference is opposite for the fast and slow rotations, indicating that the cell body and the flagellum rotate in the opposite directions. The filtered data for the  $x(t)$  and  $y(t)$  displacements can be recombined to produce Lissajous figures, which are displayed in Figure 2.4. Here, the left column (A and D) is for the high-frequency (flagellum) rotation, the middle column (B and E) is for the low-frequency (cell body) rotation, and the right column (C and F) is for the linearly superimposed rotations of both fast and slow components. The time is color coded with red being the beginning and blue the end of the trajectory. A convenient way to characterize the state of the flagellar motor is to use the winding angle  $\phi(t)$ , which as delineated in Figure 2.1 allows the motor reversals to be characterized.

It must be pointed out that while the  $\phi(t)$  measurement is straightforward, it works best for cells that display wobbly swimming patterns, i.e., the cell body spirals about the swimming direction. For cells that are not wobbly, such as those with high axial symmetry, the signal in the PSD is small and it sometimes becomes difficult to determine a motor reversal unambiguously. A simple solution to this problem is to tilt the laser trap slightly so that the  $z$  movement is coupled to the  $x$  movement, which can be detected by the PSD.

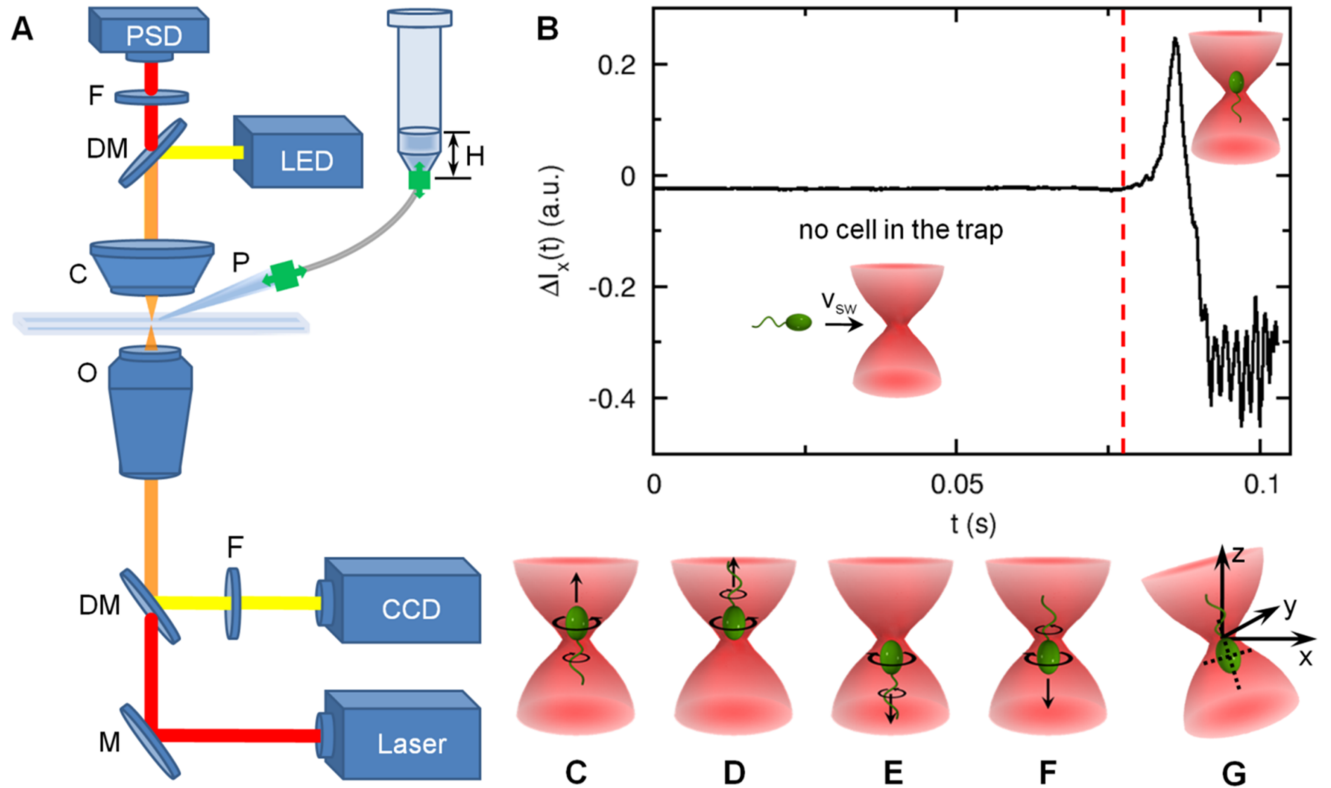


Figure 2.2: Experimental setup. (A) The trapping beam (red) from an IR laser was focused into the sample chamber by a high N.A. objective (O). The scattered light was refocused onto a position-sensitive detector (PSD) using a high N.A. condenser (C). An infrared filter (F) was placed before the PSD to cut off ambient light. The focal plane was illuminated by a LED and imaged by a CCD camera via dichroic mirrors (DMs). To eliminate the laser light, a visible band-pass filter (F) was used in front of the CCD. To stimulate a trapped cell, a micropipette (P) was mounted onto the stage that held the sample chamber. The x-y stage movements were controlled by DC actuators whereas the z movement was controlled by a piezo-actuator. A small hydrostatic pressure was applied to the micropipette via a plastic tubing by a water column of height  $H$ , where the plastic tubing was filled with air. (B) When the bacterium was outside the optical trap, the optical signal  $\Delta I_x(t)$  was quiescent. However, when the bacterium swims into the optical trap, it first produces a large spike in  $\Delta I_x(t)$  and then the signal fluctuates with a large amplitude. The red line in the figure indicates the moment just before the bacterium falls into the optical trap. We used the change in the rms value of  $\Delta I_x(t)$  to trigger the movement of the x-y stage, causing a relative motion between the trapped cell and the micropipette tip. A trapped bacterium can assume one of the four configurations (C to F) and its swimming direction cannot be resolved. (G) In a slightly tilted optical trap, the  $z$  position is coupled to the  $x$  position and thus the CCW and CW rotation of the motor can be readily measured by the PSD. As discussed in Appendix A.2, this tilted optical trap significantly improves the detection of a motor reversal, but it still does not resolve degeneracies in the cell orientation as displayed in (C to F).

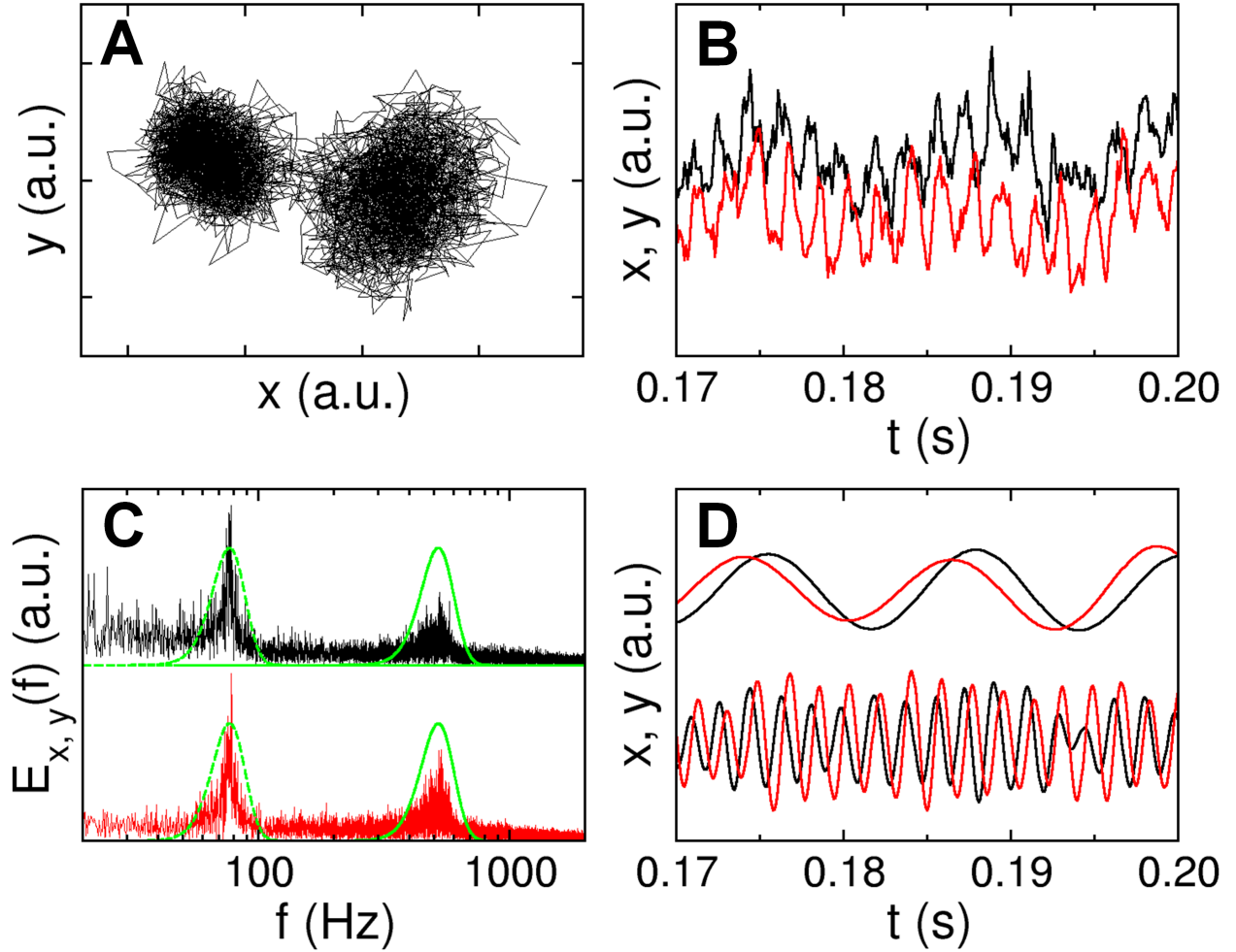


Figure 2.3: Bacterial positions in the optical trap. The bacterial position  $(x(t), y(t))$  in the optical trap is recorded by the PSD, and a trace of 2 s is given in (A). A stretch of the data for the x- (black) and y-channel (red) is given in (B), and the corresponding power spectra are presented in (C). The peaks in the power spectra are due to cell-body and flagellar rotations. We applied Gaussian band-pass filters (green lines) to  $E_x(f)$  and  $E_y(f)$  to separate rotational motions of the cell body and the flagellum. The filtered data can be used to perform an inverse Fourier transformation, yielding the results for the cell-body (top) and the flagellum rotations (bottom) in (D). Note that after band-pass filtering the phase differences between red and black curves for the cell body (top) and the flagellum (bottom) are opposite to each other, indicating that the cell body and the flagellum are rotating in opposite directions. When a polar angle is used, the angular displacements (or the winding angle)  $\phi_L(t)$  of the cell body and the flagellum  $\phi_H(t)$  can be calculated. In this thesis, we exclusively use  $\phi(t) = \phi_H(t)$ .

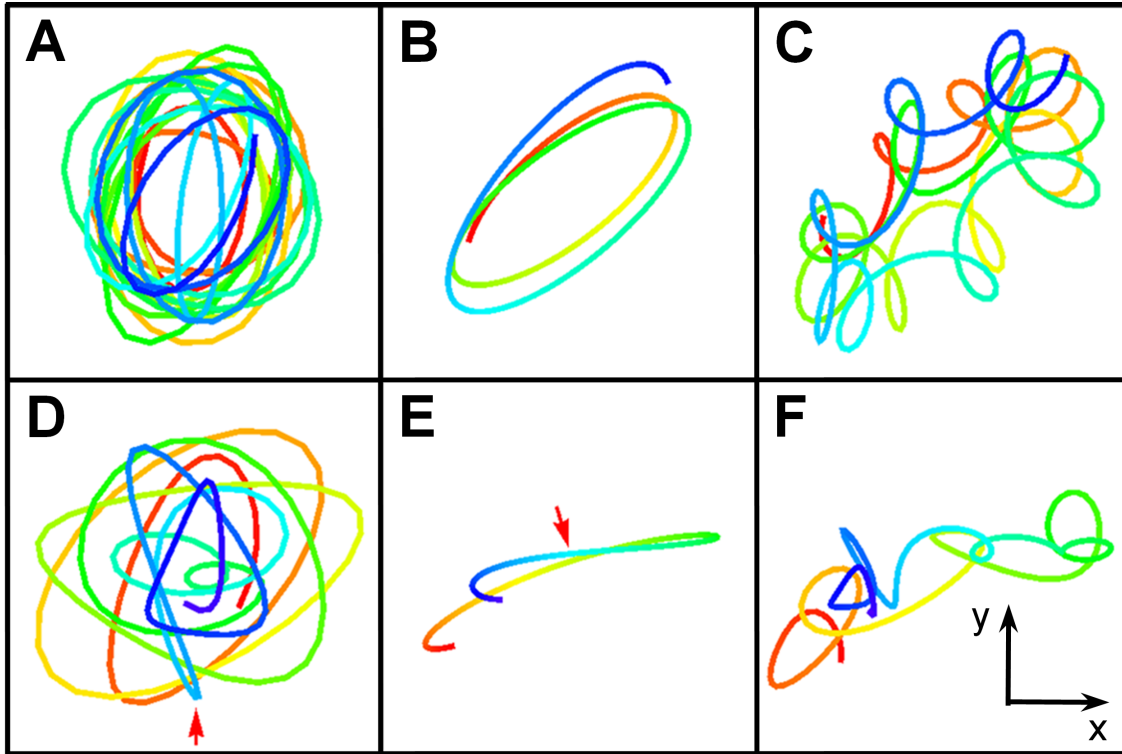


Figure 2.4: Lissajous figures of bacterial trajectories in the optical trap. For illustration purpose, the top and bottom rows depict two bacterial trajectories  $(x(t), y(t))$  in the optical trap, lasting for 300 ms and 180 ms each. Here, (A) and (D) correspond to the high frequency  $f_H$  components of rotation; (B) and (E) correspond to the low frequency  $f_L$  components of rotation; and (C) and (F) are the linear superposition of (A) and (B), and (D) and (E), respectively. In all of these figures, the flow of time is designated by colors, starting with red and ending with blue. We note that the sense of rotation is opposite for the high and the low frequency components, which is expected for the torque balance between the bacterial cell body and flagellum. For the Lissajous figures in the lower row, a switching event occurs at the location (see arrows) where the color turns from green to blue.

Figure 2.2(G) depicts the optical tweezers setup where a bacterium is assumed to be trapped in the tail-up position. The CCW (CW) rotation of the flagellum will push (pull) the cell body so that it gives a small displacement in the positive (negative)  $x$  direction (see more details in Appendix A.2). Figure 2.5(A) displays the switching events using this technique. As can be seen, the correlation between the  $\phi(t)$  and the  $x(t)$  measurements is nearly perfect. Our current experimental setup would not allow us to distinguish the rotation directions of a flagellar motor (see more discussions in Appendix A.2); therefore, only measurements concerning the motor switching rate  $S(t)$  will be reported. For a bacterium performing 3-step motility pattern with the mean forward and backward swimming times being about the same [92],  $S(t)$  is a relevant quantity for characterizing its chemotactic behavior.

### 2.2.2 Characterization of the chemoattractant concentration profile

A stable serine concentration gradient was established following the procedure described in Appendix A.3. Figure 2.6(A) displays a background corrected fluorescence intensity profile of fluorescein, which mimics serine. We can model the concentration profile  $c(\vec{r}, t)$  using the diffusion equation,

$$\frac{\partial}{\partial t}c(\vec{r}, t) + \vec{\nabla} \cdot \vec{J}(\vec{r}, t) = 0, \quad (2.1)$$

where  $\vec{J}(\vec{r}, t)$  is the flux. Phenomenologically, we write the flux as  $\vec{J} = \vec{J}_0\delta(\vec{r}) - D\vec{\nabla}c$ , which consists of a deterministic injection term and a term due to thermal diffusion. For simplicity of calculation, the injection term is approximated by a  $\delta$  function because the mouth of the capillary is very small. In the above,  $D (= 6 \times 10^{-6} \text{ cm}^2/\text{s})$  is the diffusion constant of the dye (or  $D = 9 \times 10^{-6} \text{ cm}^2/\text{s}$  for serine) and  $\vec{J}_0 \propto c_0\vec{v}_0$  with  $\vec{v}_0$  being the injection velocity. The proportionality constant between  $\vec{J}_0$  and  $c_0\vec{v}_0$  has a dimension of length to the cubic power. We seek the steady-state solution, which is given by

$$\vec{\nabla}^2c = \vec{\nabla} \cdot \left( \frac{\vec{J}_0}{D}\delta(\vec{r}) \right). \quad (2.2)$$

Using the mathematical identity  $\delta(\vec{r}) = -\nabla^2(4\pi r)^{-1}$ , Eq. 2.2 can be solved with the result,

$$c(\vec{r}) = \frac{\vec{J}_0 \cdot \hat{r}}{4\pi D r^2} = \frac{J_0 \cos \theta}{4\pi D r^2}. \quad (2.3)$$

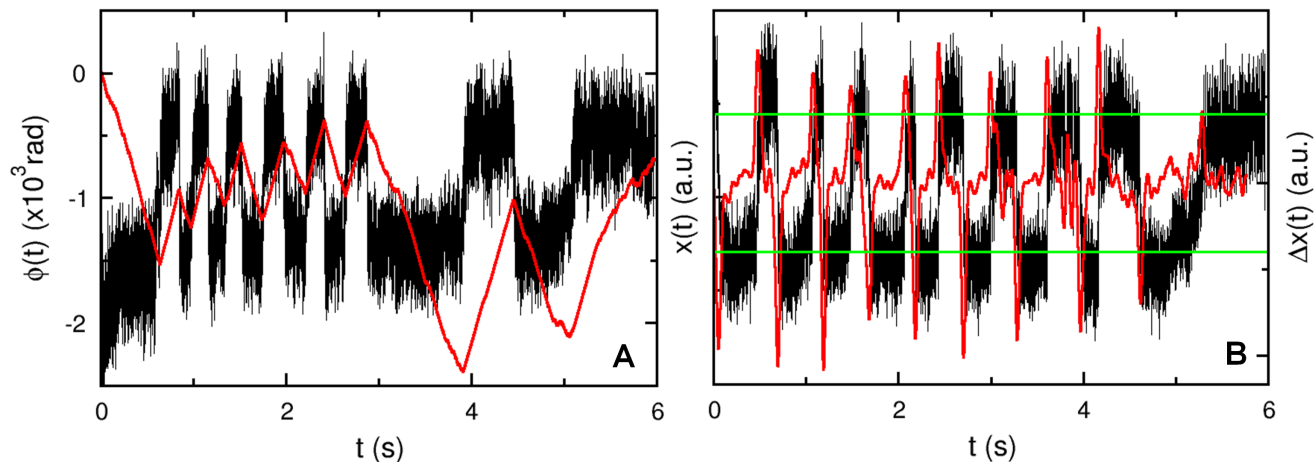


Figure 2.5: Two rotation states of bacterial flagellar motor in the optical trap. In (A), the correlation between  $\phi(t)$  and  $x(t)$  is demonstrated. The x-channel,  $x(t)$ , from the PSD exhibits a two-state behavior as displayed by the black curve. For a given state, the thick dark band corresponds to rapid oscillations due to cell-body and flagellum rotations as delineated in Figure 2.3. The transition from one state to the other is due to motor reversals. These transitions are strongly correlated with the turning points in the angular displacement  $\phi(t)$  depicted by the red curve. In (B), the switching events occurring at different times are identified in a typical run. The smoothed time derivative  $\Delta x(t)$  (red) is obtained by convolving  $x(t)$  (black) with the derivative of a Gaussian function. The width of the Gaussian is adjusted such that it captures the changes occurring over times greater than 50 *ms*. Only those events for which the derivative exceeds the threshold (green lines) are registered as switching events. The threshold is determined individually for each cell.

We note that this concentration profile is different from when  $J_0 = 0$ . In that case, the quasi-steady-state profile is determined by thermal diffusion alone, and the profile at large distances decays as  $r^{-1}$  [11]. A computer generated dye distribution according to Eq. 2.3 is given as an inset in Figure 2.6(B). The video images acquired using the CCD camera are two dimensional, and thus the above calculated three-dimensional concentration profile needs to be integrated over the depth of the visual field in order to compare with the measurement. For simplicity, we assumed that  $c(\vec{r})$  is viewed along the  $z$ -axis (see Figure 2.6(B)), and our measured intensity profile  $I(\rho)$  with  $\rho = \sqrt{x^2 + y^2}$  is proportional to the two-dimensional projection of  $c(\vec{r})$  onto the  $x - y$  plane according to,

$$I(\rho) \propto \int_0^{\infty} \frac{J_0}{4\pi D} \frac{z}{(\rho^2 + z^2)^{3/2}} dz, \quad (2.4)$$

where  $r^2 = \rho^2 + z^2$  and  $\cos \theta = z/r$  defined in the inset of Figure 2.6(B). The above integration yields,

$$I(\rho) = c' \frac{J_0}{4\pi D \rho}, \quad (2.5)$$

where  $c'$  is a constant that can be determined by calibration. However, in this work this is not important since we are only interested in the width of the concentration profile. As depicted in Figure 2.6(B), where  $I(\rho)$  vs.  $\rho^{-1}$  is plotted, our theoretical result (dashed line) agrees well with the measurement (solid circles) over a broad range of  $\rho$ ; the graph displays a quasi linear region for small  $\rho^{-1}$  that is expected from Eq. 2.5. The strong deviation from the linear behavior occurs when  $\rho^{-1} > 0.2 \mu\text{m}^{-1}$ , which is also expected because near the mouth of the micropipette the flux  $J_0$  cannot be simply described by the  $\delta$  function. To remove the singularity at  $r = 0$  in Eq. 2.3, one can replace  $r$  by  $(r^2 + \rho_0^2)^{1/2}$ , which leads to

$$I(\rho) = c' \frac{J_0}{4\pi D (\rho^2 + \rho_0^2)^{1/2}}, \quad (2.6)$$

after the  $z$  integration. This equation is used to fit the measured intensity profile in Figure 2.6(B) as displayed by the solid red line. The fitting procedure yields  $\rho_0 \approx 5.6 \mu\text{m}$ , which can be considered as the width of the concentration profile in our experiment. Measurements using different hydrostatic pressures  $\Delta P$  show that the intensity maximum  $I_{max}$  at the center

of the concentration profile is a linear function of  $\Delta P$ , which is displayed in Figure 2.6(C) along with the fitting line. This linear dependence is expected from Eq. 2.5 since the injection velocity  $v_0$  or the rate  $J_0$  is proportional to  $\Delta P$  according to the Stokes law [50]. In the experiment,  $\Delta P$  is controlled by a water column of height  $H$ , as delineated in Figure 2.2. In Figure 2.6(D), we also plotted the half-width  $\rho_{1/2} (\equiv \sqrt{3}\rho_0)$  at half-height  $I_{max}/2$  as a function of  $H$ . Here again  $\rho_{1/2}$  is approximately linear in  $H$ . For the measurement presented below we set the water column height at  $H \sim 22$  mm, which yields  $\rho_{1/2} \approx 9.7 \mu\text{m}$  (or  $\rho_0 \simeq 5.6 \mu\text{m}$ ).

Although the concentration profile  $c(r)$  is established by injection, the attractant flux is so small that the background serine concentration increases negligibly during the measurement, which lasts less than an hour. A control experiment was conducted in the same sample chamber with 0.3 ml of TMN motility buffer (see Appendix A.1), and the micropipette was filled with  $c_0 = 100$  mM of fluorescein. A small volume of fluid inside the chamber was sampled periodically after thorough mixing, and its fluorescence intensity was determined by a fluorescent spectrometer (Perkin Elmer, LS-3B). This measurement, which is presented in Figure 2.6(E), yields  $\frac{1}{c_0} \frac{\Delta c_\infty}{\Delta t} = 1.5 \times 10^{-8} \text{ s}^{-1}$ , where  $c_\infty$  is the background fluorescein concentration in the chamber after mixing. In our stimulation experiment, the highest serine concentration used was  $c_0 = 10 \mu\text{M}$ , which corresponds to a total flux of  $\frac{\Delta c_\infty}{\Delta t} \simeq 0.15 \text{ pM/s}$ . For  $\Delta t \simeq 3 \times 10^3 \text{ s}$ ,  $\Delta c_\infty \simeq 0.45 \text{ nM}$ . This change is significantly less than the stimulation level  $c_0$ , or the sensitivity of *V. alginolyticus* to serine, which we show below to be  $\sim 0.2 \mu\text{M}$ .

### 2.2.3 The average switching rate

As a demonstration of our technique, Figure 2.1(B) displays a simple measurement where individual bacteria were trapped at a distance  $\sim 120 \mu\text{m}$  from the tip of the capillary filled with 1 mM of serine. The cells were then moved towards the tip or up the gradient direction ( $+\vec{\nabla}c$ ) at a speed of  $v = 30 \mu\text{m/s}$ . The average switching rate among 60 cells were determined. Likewise, a similar number of bacteria were also trapped at  $5 \mu\text{m}$  from the capillary tip (see Figure 2.1(C)) and moved away from the tip ( $-\vec{\nabla}c$ ) at the same speed. These two sets of measurements were presented in Figure 2.1(F) by the green and the red bars, respec-

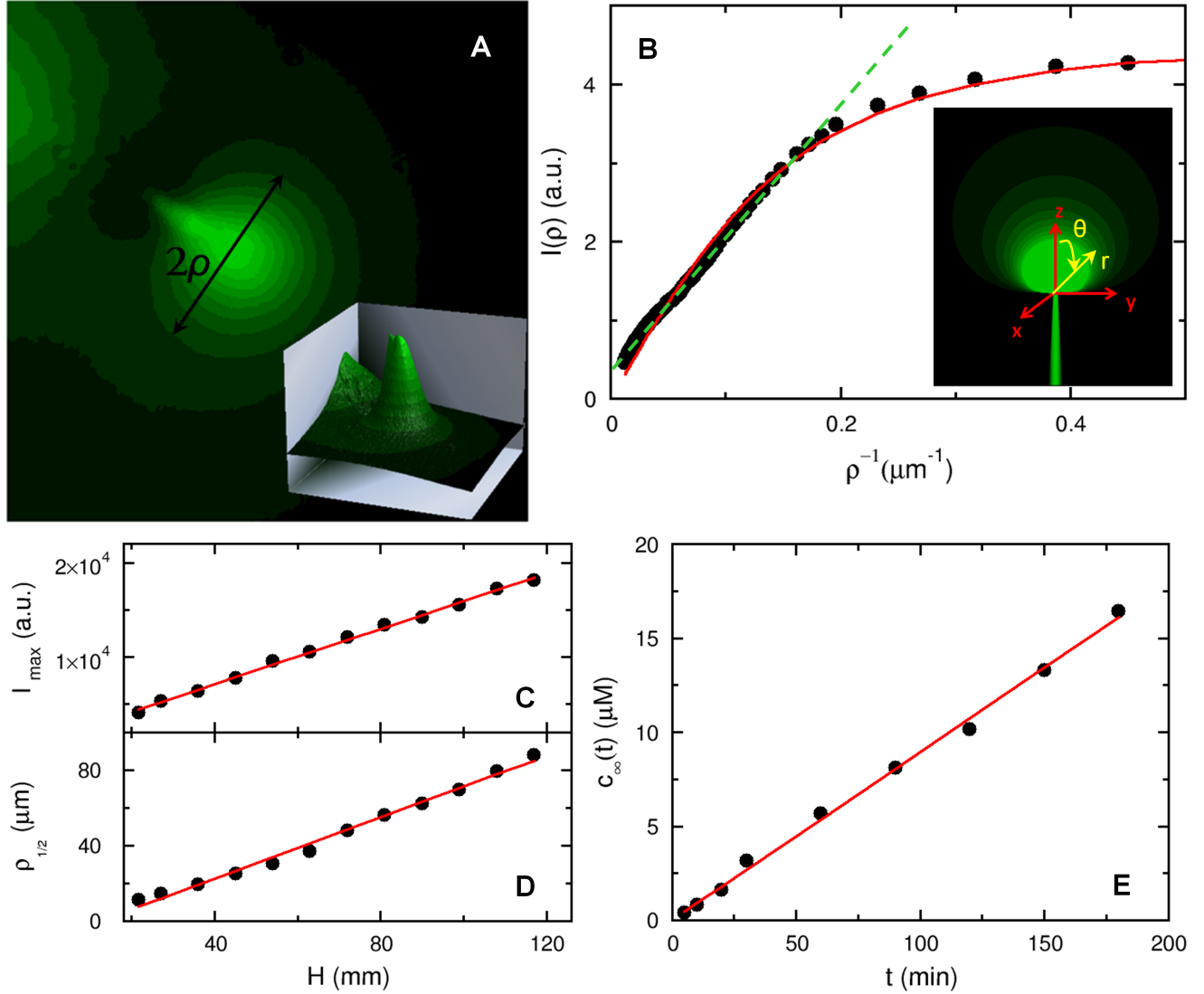


Figure 2.6: The chemoattractant concentration profile. (A) To visualize the concentration profile of serine, a micropipette was filled with 10 mM fluorescein and a small hydrostatic pressure was applied by a water column to maintain a continuous flow of dye into the sample chamber. The height of the water column was set to  $H = 22$  mm and kept fixed in all measurements. The fluorescence intensity distribution after the background subtraction is displayed in (A) and in the inset. In (B), the measured intensity  $I(\rho)$  is plotted against  $1/\rho$ , where  $\rho$  is along the radial direction as delineated in (A). In the far field,  $I(\rho)$  is proportional to  $1/\rho$  as displayed by the dashed green line, which is expected from the calculation. The solid line is the fit to Eq. 2.6, which captures both the near- and far-field behaviors. The inset is a computer generated plot of the dye distribution according to Eq. 2.3, where  $J_0/4\pi D = 1$  and the same coordinate system is used as in the calculation. In (C and D), the fluorescence peak intensity ( $I_{\max}$ ) and the half-width at half-height ( $\rho_{1/2}$ ) were measured as a function of the water column height  $H$ . In (E), the micropipette was filled with 100 mM of fluorescein, and the mean fluorescein concentration in the sample chamber (with a total volume of 0.3 ml) was measured as a function of time  $t$ .

tively. As a comparison, we also trapped a group of 70 bacteria individually and moved them in a homogeneous TMN background (see Figure 2.1(A)). This measurement is displayed by the blue bar in the same figure. The data showed that upon moving away from the source of attractant, the average switching rate  $\bar{S}$  increases compared to that in the homogeneous TMN. A striking feature of Figure 2.1(F) is that when the cells were moved towards the source of attractant,  $\bar{S}$  is suppressed to such an extent that it is barely measurable. For instance, among the 60 cells tested, only 5 showed a motor reversal when moved up the gradient. These results are consistent with that displayed in Figure 2.1(E) (see the green line). Our measurements indicate that (i) the response of *V. alginolyticus* to a deteriorated and an improved environment is not symmetrical; it appears that cells can more readily suppress the motor switching rate than enhance it. (ii) Since the cell orientation in the optical trap is random when the motion of the trap is initiated, it can be concluded that this suppression must take place in either cell orientation. Hence, the cells of *V. alginolyticus* must perform chemical sensing all the time with a 100% duty cycle. It also implies that the switching logic of *V. alginolyticus* is different from *E. coli* in that the former lengthens both of its CCW and CW intervals but the latter only lengthens its CCW interval when stimulated by an attractant.

## 2.2.4 The time-dependent switching rate

### 2.2.4.1 Chemotactic response measurements

A more revealing quantity to measure is the time dependent switching rate  $S(t)$  when the cells are exposed to a short pulse of stimulus at  $t = 0$ . In order to measure this quantity reliably, it is crucial to have precise timing. As discussed in Appendix A.2, there is a considerable change in the optical signal when a bacterium becomes trapped. This signal provides a convenient means for us to define  $t = 0$  and to synchronize all the subsequent steps, which include the movement of an x-y stage, monitoring the position of the cell in the optical trap using PSD, and termination of the run. Specifically, once a bacterium falls into the optical trap that is located  $3\ \mu\text{m}$  from a serine-filled micropipette tip, it is forced to move away from the tip with a speed  $v = 30\ \mu\text{m/s}$  that is comparable to the swimming speed  $v_{sw}$  of the bacterium. Since the

width of the serine profile is  $2\rho_0$ , the characteristic time of a cell's exposure to the chemical is  $\tau_0 = 2\rho_0/v \simeq 0.4$  s. To obtain  $S(t)$ , we first identified, for each bacterium trapped, the times when individual switches took place. This was accomplished by accentuating the switching events using a smoothed time derivative of  $x(t)$  and a threshold was then applied as shown in Figure 2.5(B). The smoothed time derivative was performed by convolving  $x(t)$  with the derivative of a Gaussian function,

$$\Delta x(t) = \int_{-\infty}^{\infty} D(t-t')x(t')dt', \quad (2.7)$$

where  $D(x) = \frac{d}{dx} \left[ \frac{1}{\sqrt{2\pi}\sigma} \exp\left(-\frac{x^2}{2\sigma^2}\right) \right]$ . The distance between the positive and negative peaks of the kernel was set to  $2\sigma \sim 50$  ms so that the convolution is equivalent to a finite-time difference ( $\Delta t \sim 50$  ms) with low-pass filtering to get rid of high frequency oscillations of the cell body. Figure 2.5(B) displays the original time series  $x(t)$  (black) of a typical cell along with its smoothed time derivative  $\Delta x(t)$  (red). We chose a threshold manually for each cell so that all the major abrupt changes in the derivative were accounted for. This is illustrated by the two green lines in the figure.

As a control, we filled the micropipette with the motility buffer (TMN) without serine. The total number of bacteria in this data set was 254, resulting in 3404 switching events. These events were used to construct the cumulative distribution function, which after normalizing by the cell number is designated as  $\Psi(t)$ . As shown in the inset of Figure 2.7, for a short time  $t \leq t_0 \simeq 2$  s,  $\Psi(t)$  increases linearly with time  $t$ , but for  $t > t_0$ ,  $\Psi(t)$  starts to level off in long times. The slope of the initial increase yields the steady-state switching rate  $S_0 = d\Psi/dt = 3.13$  s<sup>-1</sup>, which is consistent with the observation of the free-swimming bacteria ( $3.25 \pm 0.03$  s<sup>-1</sup>) in the steady state (see Appendix A.4). The leveling off of  $\Psi(t)$  indicates that the bacteria switch less frequently in long times. This is likely due to photodamage, even though most of the cells released after the measurement did not lose their ability to swim. Taking into account this effect, we found that  $\Psi(t)$  can be adequately described by the following functional form,

$$\Psi(t) = \begin{cases} S_0 t & 0 \leq t < t_0 \\ S_0 t_0 + S_0 \tau_p \left[ 1 - \exp\left(-\frac{t-t_0}{\tau_p}\right) \right] & t_0 \leq t < \infty \end{cases}, \quad (2.8)$$

where the characteristic decay time  $\tau_p \simeq 5.2$  s. In the inset of Figure 2.7, the measured  $\Psi(t)$  (black curve) is plotted alongside with Eq. 2.8 (red curve). In the same inset, we also plotted the ideal case (green line), when the bacterial switching rate remains constant at all times. This demands a correction (blue curve) of the form,

$$\delta\Psi(t) = \begin{cases} 0 & 0 \leq t < t_0 \\ S_0(t - t_0) - S_0\tau_p \left[ 1 - \exp\left(-\frac{t-t_0}{\tau_p}\right) \right] & t_0 \leq t < \infty \end{cases} \quad (2.9)$$

This correction factor  $\delta\Psi$  is applied to all of our subsequent measurements with different serine concentrations. An example with  $c_0 = 10 \mu\text{M}$  of serine is displayed in Figure 2.7, where the measured (black curve) and the corrected  $\Psi(t)$  (green curve) are displayed. By definition, the time-dependent switching rate is given by  $S(t) = \frac{d}{dt}\Psi(t)$ . To reduce noises, the data was first binned over the time interval of 50 ms and then a finite difference  $S(t) = \Delta\Psi/\Delta t$  was taken.

The time-dependent responses to different levels of chemical stimulations are displayed in Figures 2.8(A-C), where the micropipette was filled with  $c_0 = 1, 5, \text{ and } 10 \mu\text{M}$  of serine. The number of bacteria in each set was 314, 384, and 513 with the corresponding number of switching events being 4329, 5507, and 5849, respectively. We noticed that as  $c_0$  increases, the initial switching rate can be significantly reduced, and in the case of  $c_0 = 10 \mu\text{M}$ ,  $S(t)$  is only  $\sim 0.3 \text{ s}^{-1}$  in short times or about a factor of ten less than the steady-state value  $S_0$ . We also noticed that  $S(t)$  recovers rapidly over time, and the process is biphasic, i.e.,  $S(t)$  overshoots beyond  $S_0$  and then relaxes towards  $S_0$  over a long time. Qualitatively, therefore, *V. alginolyticus*' chemotactic response is surprisingly similar to *E. coli*, consisting of a short initial excitation followed by a long adaptive process.

**2.2.4.2 Theoretical modeling** The biphasic response was first discovered in *E. coli* [74], and we are surprised to see that *V. alginolyticus* has a similar response. Considerable progress has been made over the past several years in terms of a quantitative understanding of this fascinating behavior in *E. coli* [9, 20, 77, 78, 63, 43, 86]. The progress was made because of extensive knowledge of biochemistry of several *che* gene products and their interactions with chemoreceptors and the motor complex. Although much less is known about

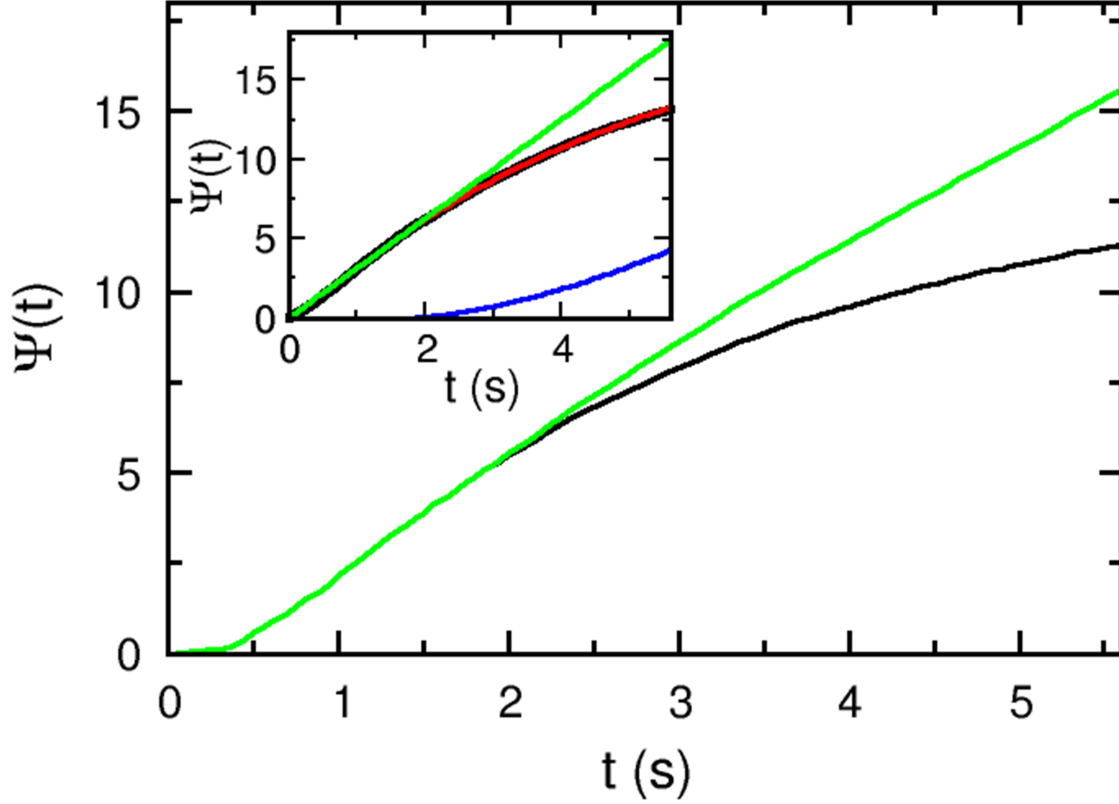


Figure 2.7: Normalized cumulative distribution functions (CDFs). The measured CDF (black) can be mimicked by the function  $\Psi(t)$  (red), which is given in short times ( $t < t_0 = 2$  s) by  $S_0 t$  and in long times ( $t > 2$  s) by  $S_0 \left[ t_0 + \tau_p \left( 1 - \exp\left(-\frac{t-t_0}{\tau_p}\right) \right) \right]$ , where  $S_0 = 3.13 \text{ s}^{-1}$  is the initial switching rate, and  $\tau_p = 5.2$  s. The experimental data after the photodamage correction  $\delta\Psi(t)$ , which is represented by the blue line, yields the green line. In the main figure, the same correction function  $\delta\Psi(t)$  is applied to the measurement (black) when  $10 \mu\text{M}$  of serine is present. The resulting curve is presented in green.

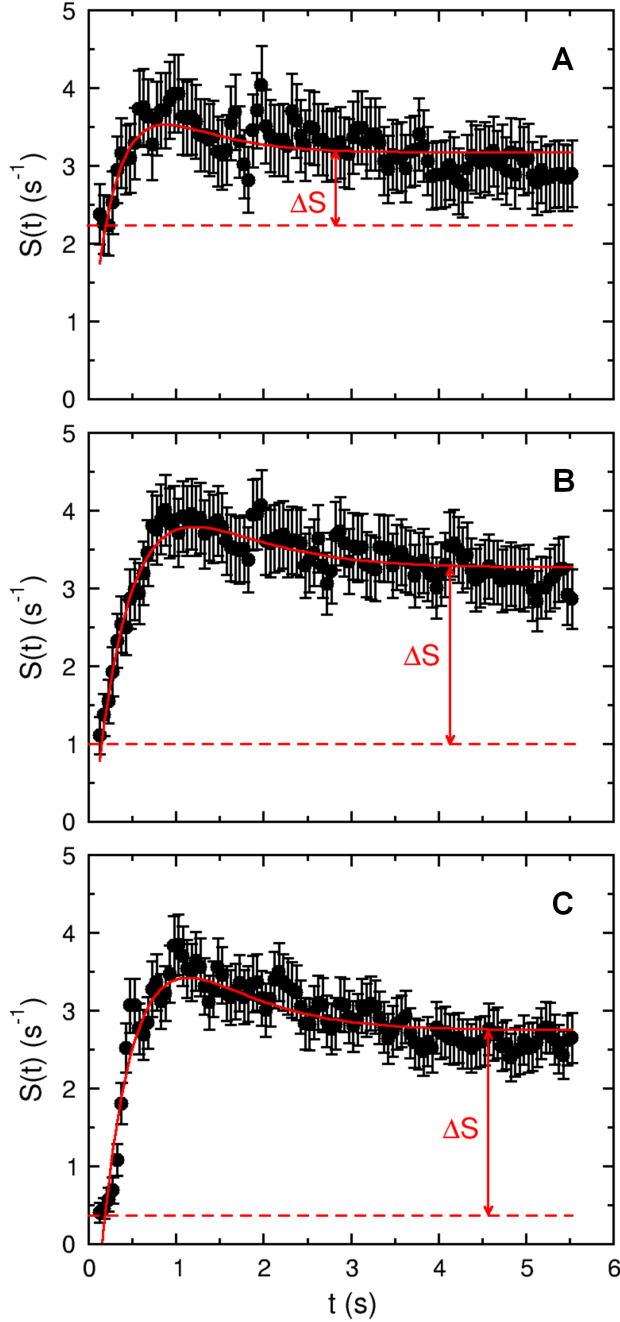


Figure 2.8: The time-dependent switching rate of *V. alginolyticus*. The measured switching rates for  $c_0 = 1, 5$  and  $10 \mu\text{M}$  of serine are plotted as dots in (A to C), respectively. The stimulation occurs at  $t = 0$ . In all the cases, an initial suppression in  $S(t)$  was followed by an overshoot beyond the steady-state switching rate  $S_0$ . It is only in long times that  $S_0$  is recovered. The red curves in each plot are the fits using Eq. 2.15. The fitting procedure yields the following parameters:  $S_0 = 3.17 \text{ s}$ ,  $R'_0 = 0.83$ , and  $\tau = 0.44 \text{ s}$  for (A);  $S_0 = 3.27 \text{ s}$ ,  $R'_0 = 1.19$ , and  $\tau = 0.60 \text{ s}$  for (B); and  $S_0 = 2.75 \text{ s}$ ,  $R'_0 = 1.85$ , and  $\tau = 0.56 \text{ s}$  for (C). Here, we treated  $S_0$  as an adjustable parameter; as can be seen, its value does not change much from run to run.

*V. alginolyticus*' chemotaxis regulation [47, 61], the similarity in the response seen in our experiment suggests that the regulation mechanism in *V. alginolyticus* may be similar. One of the successful models in explaining the biphasic response is the Monod-Wyman-Changeux (MWC) model proposed by Tu et al. [86]. This mean-field model integrates out fast kinetics of binding and unbinding of chemoeffectors to receptors, and leaves comparatively slow processes of dephosphorylation and methylation as independent variables. The model has been successfully applied to explain the response data acquired in *E. coli* using a variety of stimulation protocols [18, 74]. In the following we will focus on the impulse stimulation when the serine concentration is low so that the bacterial response may be considered linear.

We assume that the switching rate is determined by the phosphorylated form of response regulator CheY-P whose concentration  $[Y]$  varies with time  $t$  according to,

$$\Delta[Y](t)/[Y](0) \equiv [Y](t)/[Y](0) - 1 = \int_0^t R(t-t') \Delta f_L(t') dt', \quad (2.10)$$

where  $[Y](0)$  is the CheY-P concentration at the steady state,  $\Delta f_L(t)$  is the change in the free energy (in terms of thermal energy  $k_B T$ ) when the ligand concentration varies from its pre-stimulation level  $[L](0)$  to  $[L](t)$ , and  $R(t)$  is the linear response (or Green's) function. This assumption is consistent with Kojima et al.'s observation that phosphorylation of CheY is necessary for motor reversals similar to *E. coli* cells [47]. For convenience, we will use *E. coli*'s response function to mimic that of *V. alginolyticus* [86],

$$R(t > 0) = R_0 [\tau_z \exp(-\frac{t}{\tau_m}) - \tau_m \exp(-\frac{t}{\tau_z})] / (\tau_m - \tau_z), \quad (2.11)$$

where  $\tau_z$  and  $\tau_m$  are respectively the dephosphorylation and methylation times, and  $R_0$  is the amplitude of the response.  $R_0$  is a measure of the sensitivity of the chemotactic network and is given by  $R_0 = N a_0 (1 - a_0) k_a / [Y](0)$ , where  $N$  is the number of ligand-binding subunits in the MWC clusters,  $0 \leq a_0 \leq 1$  is the average steady-state kinase activity, and  $k_a$  is the phospho-transfer rate, which depends on the total number of MWC complexes in a cell.

The above model enables one to establish the connection between the microscopic chemical-reaction (ligand-receptor binding) kinetics and macroscopic bacterial response. Specifically, we are interested in the switching rate  $S(t)$  after a brief stimulation by serine. For a weak

stimulation, it is reasonable to assume that  $S(t)$  depends linearly on CheY-P concentration such that

$$S(t) = S_0(1 + g\Delta[Y](t)/[Y](0)), \quad (2.12)$$

i.e., an increase in CheY-P will increase the switching rate beyond the steady-state value  $S_0$ . In the above,  $g$  is the gain factor of the motor complex, which is related to the Hill coefficient  $H$  by  $g = H/4$ . In *E. coli* for instance,  $H$  varies from 3 to 10 depending on whether the measurements were carried out in an ensemble or in single cells [72, 28]. However, since nothing is known about how the motor complex responds to a change in CheY-P in *V. alginolyticus*, we will set  $g = 1$ . We note that  $g$  only affects the amplitude of the response function but not its overall functional form. The effect of  $g \neq 1$  can be readily taken into account once its value becomes available. Substituting  $\Delta[Y]/[Y](0)$  from Eq. 2.10, we find

$$S(t) = S_0 \left[ 1 + \int_0^t R(t-t') \Delta f_L(t') dt' \right]. \quad (2.13)$$

This mathematical result will be compared to our measurements. We noticed that within the linear-response approximation, Eq. 2.11 implies the adaption is precise, i.e. for a step stimulation  $\int_0^\infty R(t) dt = 0$ , and for a sufficiently long waiting time,  $S(t) \rightarrow S_0$ . This behavior appears to be consistent with our observations in Figure 2.8. As the stimulation in our experiment is brief with an exposure time  $\sim 2\rho_0/v \sim 0.4$  s,  $\Delta f_L(t)$  will be approximated by a  $\delta$  function:  $(2\rho_0/v) \ln(1 + [L]/K_I) \delta(t)$ . This leads to,

$$S(t) = S_0 \left\{ 1 + R'_0 \left[ \tau_z \exp\left(-\frac{t}{\tau_m}\right) - \tau_m \exp\left(-\frac{t}{\tau_z}\right) \right] / (\tau_m - \tau_z) \right\}, \quad (2.14)$$

where  $R'_0 = (2\rho_0/v) \ln(1 + [L]/K_I) R_0$ . This equation contains three adjustable parameters,  $R'_0$ ,  $\tau_z$ , and  $\tau_m$ , if  $S_0$  is assumed to be known. While analyzing the data, we found that the best result could be attained when  $\tau_z$  and  $\tau_m$  were very close for all of our measurements. In the limit  $\tau_m \rightarrow \tau_z = \tau$ , the above equation can be cast in the form,

$$S(t) = S_0 \left\{ 1 - R'_0 \left( 1 - \frac{t}{\tau} \right) \exp\left(-\frac{t}{\tau}\right) \right\}, \quad (2.15)$$

and effectively only two parameters,  $R'_0$  and  $\tau$ , are necessary. As shown in Figures 2.8(A-C), all of our data can be fit reasonably well by the above equation, which is indicated by the red lines in the figure. For  $c_0 = 1, 5,$  and  $10 \mu\text{M}$ , the following results are obtained:  $R'_0 = 0.83, 1.19,$  and  $1.85,$  and  $\tau = 0.44, 0.60,$  and  $0.56 \text{ s}$ . However, considering the large noise in the data, these fittings are not perfect particularly in long times.

The biphasic response is a hallmark of an adaptive behavior. What is unusual in our finding is that the adaptation time is so short that it is indistinguishable from the excitation time. Several lines of evidence showed that *V. alginolyticus* can adapt to serine after a step change  $\Delta c$  in the serine concentration [37]. The adaptation time becomes longer as  $\Delta c$  increases. Although a more detailed and quantitative study is needed, this adaptive behavior appears to be similar to *E. coli*. Thus, the short adaptation time seen in our experiment may correspond to either  $c_0$  is low or the stimulation is short. In any event, it suggests that *V. alginolyticus* are able to adapt to a wide range of chemical stimulations, which may be significant for bacteria to thrive in the presence of ephemeral micro-scale nutrient sources.

### 2.2.5 Sensitivity of *V. alginolyticus* to serine

A quantity of significance to bacterial chemotaxis is the dissociation constant  $K_I$ . For *E. coli* cells, previous measurements showed  $K_I$  for serine is  $\sim 14 \mu\text{M}$  [51]. Our experiments also allow us to estimate  $K_I$  for *V. alginolyticus*. Using the definition  $R'_0 (\equiv (2\rho_0/v)Na_0(1 - a_0)k_a \ln(1 + c_0/K_I))/[Y](0) = A \ln(1 + c_0/K_I)$ , we plotted  $R'_0$  vs.  $c_0$  in the inset of Figure 2.9, where  $R'_0$  was obtained from the curve-fitting procedure (see Figure 2.8). The error bars were calculated based on uncertainties in the measured switching rate  $S(t)$ . The solid line in the inset of Figure 2.9 is the theoretical prediction, where  $A = 0.46$  and  $K_I = 0.25 \mu\text{M}$  were used. Alternatively one can find  $K_I$  via the relation  $R'_0 = \Delta S/S_0$  derivable from Eq. 2.15, where  $\Delta S = S_0 - S(0)$  can be easily found for each  $c_0$  by visual inspection without the fitting procedure.  $R'_0$  determined in this manner (see Figure 2.8) is plotted in Figure 2.9, yielding  $A = 0.14$  and  $K_I = 0.11 \mu\text{M}$ . As can be seen, there is a considerable uncertainty in the determination of  $K_I$  due to the noise in  $R'_0$ . However, it is evident that  $K_I$  in *V. alginolyticus* is considerably smaller than *E. coli*. Since at  $c_0 \simeq K_I$  there is only  $\sim 10^2$

serine molecules in a cell volume and the integration time  $\tau \simeq 0.5$  s is rather short, it raises the interesting possibility that the threshold of chemosensing in this marine strain may be limited by thermal fluctuations [14, 16, 31].

Finally, using the average value of  $A$ ,  $\bar{A} \simeq 0.3$ , we can estimate the amplitude of the response function  $R_0[\equiv Na_0(1 - a_0)k_a/[Y](0)] = \bar{A}/(2\rho_0/v)$ , which turns out to be  $R_0 = 0.8 \pm 0.4 \text{ s}^{-1}$ . If the gain factor  $g$  is considered in Eq. 2.12,  $R_0$  will be reduced by the same factor.

## 2.3 DISCUSSION

In summary, studies of bacterial chemotaxis have significantly advanced our understanding of how a microorganism interacts with its environment and have general implications for higher level animals that use more sophisticated sensing apparatus [64, 49]. Over the last 40 years, methods have been developed to quantitatively investigate this fascinating phenomenon in a variety of bacteria, including *E. coli*, *Bacillus subtilis*, and *Rhodobacter sphaeroides* [76, 35, 67]. The most notable is Adler’s modern implementation of the capillary assay that allowed scientists to establish for the first time the existence of specific receptors on bacterial surfaces that play an important role in modulating cell’s motility [1]. Berg invented an impressive tracking microscope, which elucidated how *E. coli* cells perform chemotaxis [10]. Silverman et al. developed the rotation assay by tethering a flagellum on a coverslip and observing the rotation of the cell body [75]. This seemingly simple experiment, aside from demonstrating that the flagellum is powered by a rotary motor at its base [75, 12], paved the way for more advanced implementation by conjugating a small bead to the flagellum using antibodies. The rotation assay allowed scientists to study a variety of problems ranging from a torque-speed relation [25], noises in flagellar motor [71], chemotactic responses [18, 74], and molecular interactions between the chemotactic regulatory protein and the motor complex [72, 40]. Herein we added to this impressive arsenal a new approach that allows the cell to be localized while its flagellum and cell-body rotations can be monitored. Similar to the rotation assay, our method is single-cell based and permits the study of behaviors of individual cells as well

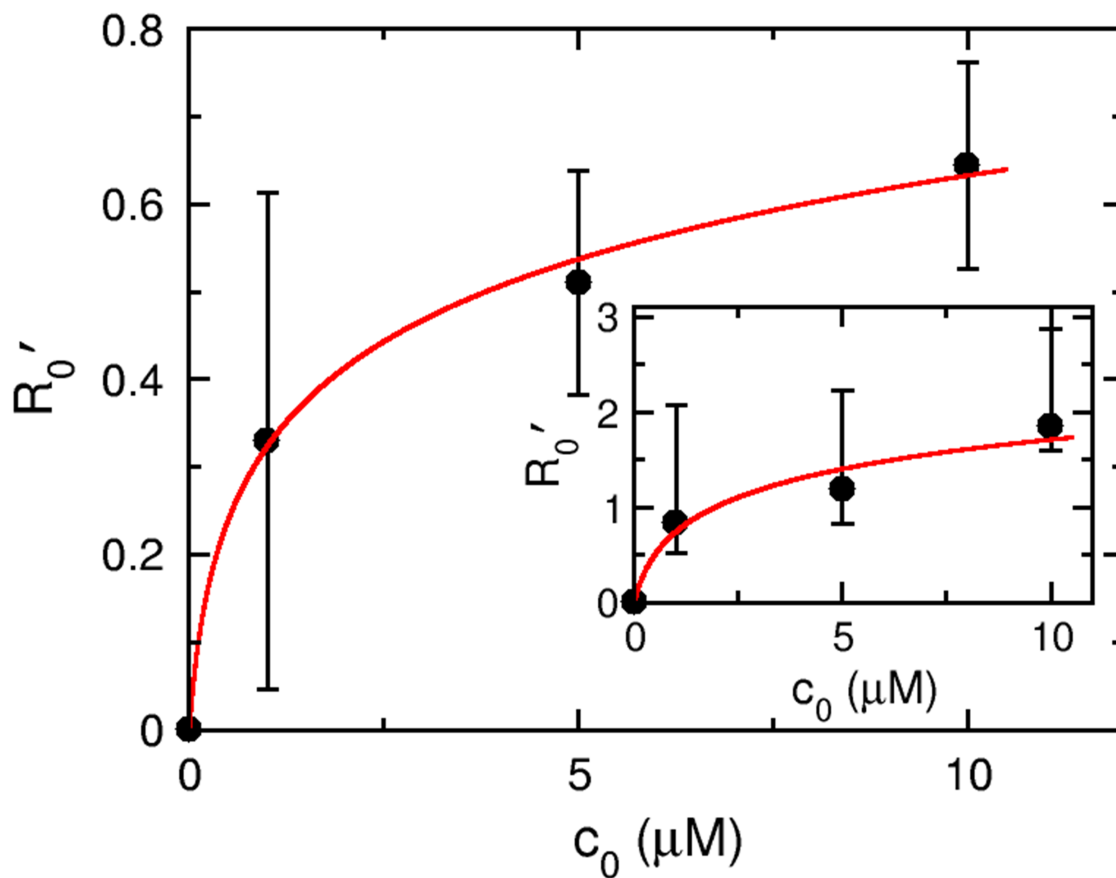


Figure 2.9: The response amplitude  $R'_0$  vs. serine concentration  $c_0$ . The solid circles are experimental data and the line is the theoretical expression  $R'_0 = A \ln(1 + c_0/K_I)$ , where  $R'_0$  are extracted from Figures 2.8(A-C). The fitting procedure yields  $K_I = 0.11 \mu\text{M}$  and  $A = 0.14$ . The curve in the inset is generated from the best fit values  $R'_0$  in Figure 2.8, and the data can be explained by  $K_I = 0.25 \mu\text{M}$  and  $A = 0.46$ , which is plotted as a solid line.

as the average behavior in a population. A distinctive advantage of our technique is that it does not rely on cell tethering and thus generally applicable to different bacteria. The ease by which the bacterium can be moved by the optical trap also allows one to design “swimming” paths so that complicated memory effects may be studied. The technique when combined with a microfluidic device would allow investigators a great deal of freedom to explore different types of chemical stimulations [60, 41].

Using the optical trapping technique we have investigated *V. alginolyticus*’ response to a short pulse of serine. If the regulatory network is linear, the measured response function can be used to interpret bacterial chemotactic behaviors in complicated chemical environments. However, the extent of this linear regime has yet to be established in future experiments. We found that the response function of *V. alginolyticus* is biphasic similar to *E. coli*, suggesting that such a behavior may be evolutionarily conserved. Unlike *E. coli*, however, the putative methylation time  $\tau_m$  turns out to be so short that it nearly matches the dephosphorylation time,  $\tau_z \simeq \tau_m \simeq 0.5$  s. Thus, the chemotactic response of *V. alginolyticus* to a short pulse of attractant essentially consists of only a single time scale. The fast adaptation seen in *V. alginolyticus* is likely due to their habitat where nutrients are short-lived so that unless the microorganisms can recover from the initial excitation quickly, the signal would be lost.

## 3.0 ADAPTATION IN *V. ALGINOLYTICUS*

### 3.0.1 Response of *V. alginolyticus* to extended exposure to serine

Unlike the impulsive stimulation experiments described in Chapter 2, in this set of experiments, the dragging was not initiated upon detection of a bacterium in the optical trap. After the bacterium was trapped at  $\sim 3 \mu\text{m}$  from a serine-filled micropipette tip, it was forced to stay there for varying amounts of time before being dragged away. The micropipettes used in these experiments were filled with  $c_0 = 5 \mu\text{M}$  of serine, which is the highest serine concentration at which no saturation effects had been observed in our preliminary experiments. The exposure time of bacteria to serine, or the waiting time  $t_w$ , ranged from 0 to 3.1 s. The cells were dragged away from the stimulation point at the same speed  $v = 30 \mu\text{m/s}$  as in the impulsive stimulation experiments. In Figure 3.1, the concentration profile sensed by the bacterium is illustrated with all the relevant experimental timescales. Here, the cell experiences a positive stimulation at  $t = 0$  and a negative stimulation at  $t = t_w$ . The optical trap data were analyzed following the procedure described in Section 2.2.4.1 and the switching rate  $S(t)$  was calculated for each  $t_w$ . The results are displayed in Figure 3.2(A-F). In these figures, the origin of the time axis corresponds to  $t = 0$  in Figure 3.1.

We found that the extended exposure to serine has multiple effects on the switching rate of *V. alginolyticus*. When  $t_w$  increases, the switching rate  $S(t)$  remains depressed if  $t_w$  is not very long as in (C-E). However, for long exposure times, such as in (F), the recovery of  $S(t)$  becomes noticeable. For the longest waiting time  $t_w = 3.1$  s, the switching rate curve in the  $[0, 3.1 \text{ s}]$  interval can be extrapolated to the steady-state switching rate  $S_0$  seen in late times and the switching rate reaches  $\sim 85\%$  of the steady-state value  $S_0$  at the end of this interval. This observation suggests that under our experimental conditions, *V. alginolyticus*

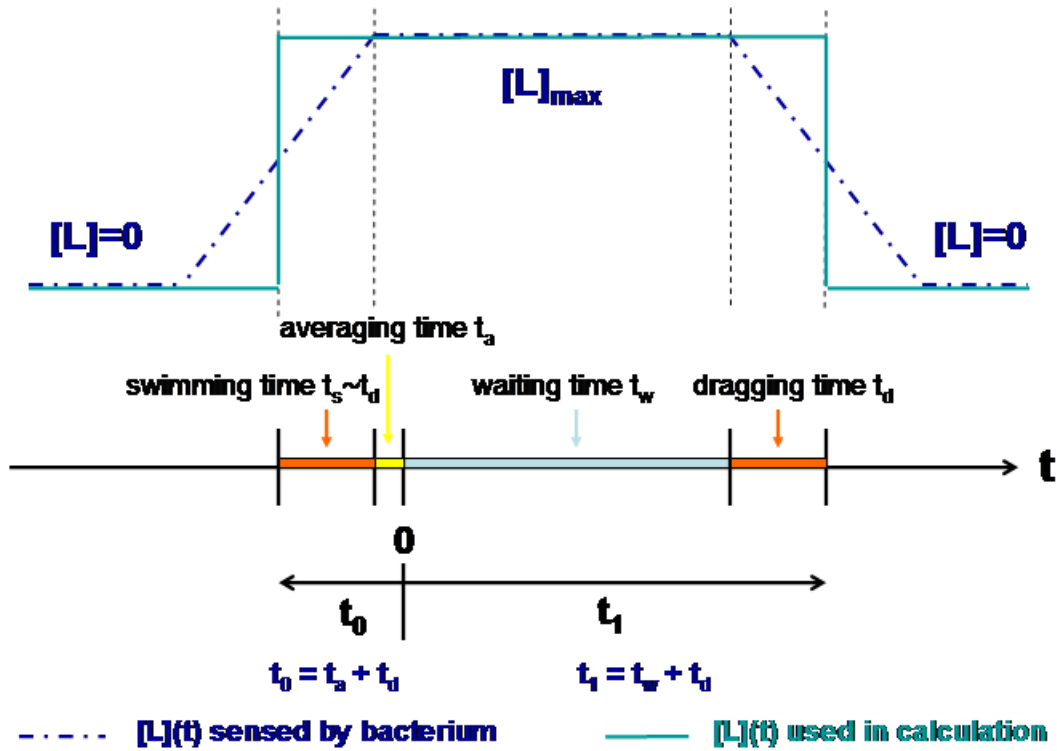


Figure 3.1: Experimental timescales. The swimming time  $t_s$  is the time it takes for a bacterium to swim from the HWHH of the concentration profile to the the peak of the profile where the optical trap is initially located. The computer calculates the rms value of  $\Delta I_x(t)$  at intervals of  $t_a = 100$  ms. An abrupt increase in the rms value indicates that a bacterium is trapped and defines the origin of the time axis, i.e.,  $t = 0$ . During the waiting (exposure) time  $t_w$  the optical trap does not move and exposes the trapped bacterium to the peak chemoattract concentration  $[L]_{max}(= c_0)$ . Subsequently, the trapped bacterium is dragged away from the micropipette tip with the aid of the optical tweezers. The dragging time  $t_d$  is defined as  $\rho_{1/2}/v$ , where  $\rho_{1/2}$  is the HWHH of the concentration profile and  $v$  is the speed at which the optical trap is moved.

can adapt to a stimulus precisely.

We noticed that as  $t_w$  increases, the bacteria respond to the negative stimulation sooner, which is indicated by the reduction in the time difference between the sharp rise of the switching rate curve  $S(t)$  and the beginning of the drag ( $t = t_w$ ), which is marked by the vertical lines in Figure 3.2. This effect may be explained by the fact that when the cells are better adapted to a given ligand concentration, they become more sensitive to changes in  $[L]$  and are able to respond faster.

Finally, we also noticed that the maximum switching rate  $S_{max}$  elicited by dragging the bacteria away from the point source is not constant but increases slightly with  $t_w$  as seen in Figure 3.2. Here, as  $t_w$  increases from 0.1 s to 1.5 s,  $S_{max}$  increases from  $\sim 3.3 \text{ s}^{-1}$  to  $\sim 4.2 \text{ s}^{-1}$ , and then decreases to  $S_{max} \simeq 3.5 \text{ s}^{-1}$  for the longest waiting time  $t_w = 3.1 \text{ s}$ . The increased switching rate indicates that chemotactic response is history dependent and for certain ligand exposure times, it can elicit a larger response than other time scales.

Another point that attracts our attention is the fine structures (see the red arrows in Figure 3.2) which become more prominent as  $t_w$  increases from 0.3 s to 1.5 s and weakens when  $t_w = 3.1 \text{ s}$ . When the cells are given sufficient time,  $\sim 0.3 \text{ s}$  for  $c_0 = 5 \mu\text{M}$  serine stimulation, they produce a more coherent response represented by a very sharp increase in the switching rate. This burst of switching events usually followed by a relatively silent period which lasts  $\sim 0.4 \text{ s}$ .

### 3.0.2 Analysis

Assuming  $K_A \gg [L] \gtrsim K_I$  in these experiments, we approximate the ligand-dependent free energy change as a square pulse,  $\Delta f_L(t) [\equiv f_L([L](t)) - f_L([L]_0)] \simeq \ln(1 + [L]_{max}/K_I)\Theta(t - t_0)\Theta(t_1 - t)$ , where the background ligand concentration  $[L]_0$  is assumed to be zero in our square-pulse stimulation experiments. This approximation is illustrated in Figure 3.1 where  $t_0$  and  $t_1$  are clearly identified. To fit our data, we substitute the linear response function given in Eq. 2.11 and the square-pulse  $\Delta f_L(t)$  in Eq. 2.13. This leads to

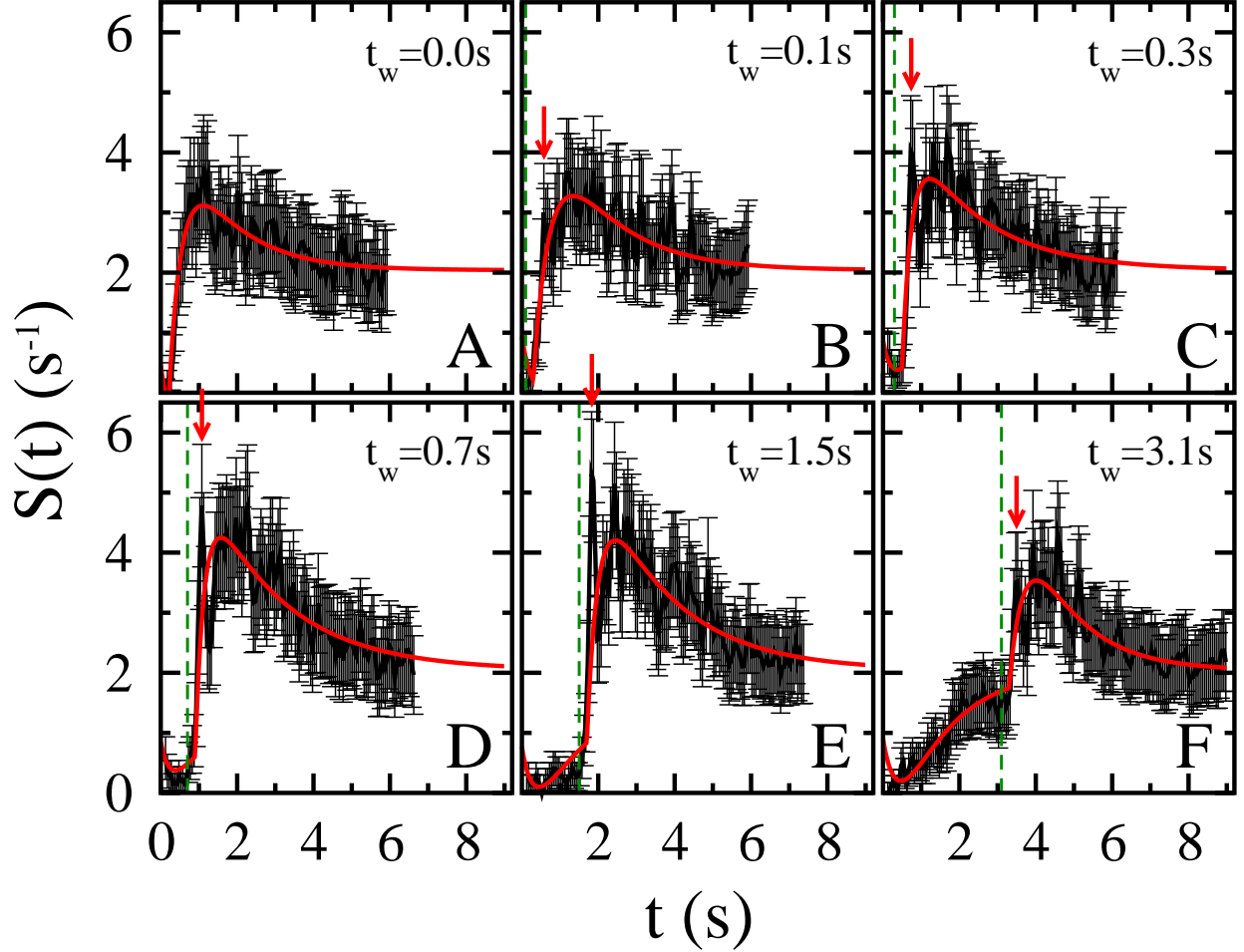


Figure 3.2: Response of *V. alginolyticus* to the extended exposure to serine. The measured switching rates for  $t_w = 0, 0.1, 0.3, 0.7, 1.5$  and  $3.1$  s are plotted in (A-F), respectively.  $c_0 = 10 \mu\text{M}$  in (A) and  $5 \mu\text{M}$  in all the others (B-F). The dashed lines indicate the end of the waiting period. The red curves are the fits using Eq. 3.3. The fitting parameters are tabulated in Table 3.1 inside the paranthesis. We noticed that  $S(t)$  displays fine structures soon after the bacteria are dragged out of the high serine concentration region. For convenience, these structures are marked by red arrows.

$$S(t) = S_0 \left\{ 1 + \frac{A_0}{(\tau_m - \tau_z)} \int_{-\infty}^t \left[ \tau_z \exp\left(-\frac{(t-t')}{\tau_m}\right) - \tau_m \exp\left(-\frac{(t-t')}{\tau_z}\right) \right] \Theta(t' - t_0) \Theta(t_1 - t') dt' \right\}, \quad (3.1)$$

where  $A_0 \equiv R_0 \ln\left(1 + \frac{[L]_{max}}{K_I}\right)$ .

When the convolution integrals are evaluated using the experimentally determined values of  $S_0 = 2.24$  s,  $\tau_z = 0.3$  s,  $\tau_m = 1.5$  s,  $t_0 = -0.2$  s and  $t_1 = t_w + 0.2$  s where  $t_w \in \{0, 0.1, 0.3, 0.7, 1.5, 3.1\}$  s and a single response amplitude  $A_0$ , the resultant response curves are seen not to belong to the same family of curves. On the other hand, the experimental response curves look very similar. This means a single  $A_0$  cannot fit both the positive and the negative stimulation parts of the response  $S(t)$ . If it fits the positive stimulation part well, it falls short to account for the strong response to the negative stimulation. We believe that the methylation process during the waiting time pushes the cells to a new activity level, which in turn determines the response strength to the subsequent stimulus. To probe how the response strength changes with increasing waiting time we assumed that the system had two different response strength parameters, namely  $A_0$  and  $A_0(1 - \alpha)$  that are effective during the positive and the negative stimulation, respectively. Based on this assumption, Eq. 3.1 can be rewritten as

$$S(t) = S_0 \left\{ 1 + \frac{A_0}{(\tau_m - \tau_z)} \int_{-\infty}^t \left[ \tau_z \exp\left(-\frac{(t-t')}{\tau_m}\right) - \tau_m \exp\left(-\frac{(t-t')}{\tau_z}\right) \right] \times [\Theta(t' - t_0) \Theta(t_1 - t') + \alpha \Theta(t' - t_1)] dt' \right\}. \quad (3.2)$$

A straight forward integration yields

$$S(t) = S_0 \left\{ 1 + A_0 \frac{\tau_m \tau_z}{(\tau_m - \tau_z)} \left[ -\exp\left(-\frac{(t-t_0)}{\tau_m}\right) + \exp\left(-\frac{(t-t_0)}{\tau_z}\right) + (1 - \alpha) \left( \exp\left(-\frac{(t-t_1)}{\tau_m}\right) - \exp\left(-\frac{(t-t_1)}{\tau_z}\right) \right) \Theta(t - t_1) \right] \right\}. \quad (3.3)$$

This function was used to fit our data. It has two adjustable parameters,  $A_0$  and  $\alpha$ , if  $S_0$ ,  $\tau_z$ ,  $\tau_m$ ,  $t_0$  and  $t_1$  are assumed to be known. Table 3.1 displays the values of the fitting parameters of this model for each  $t_w$ .

Table 3.1: Response amplitudes

$[L]_{max}$ ( $\mu\text{M}$ )	$t_w$ (s)	No. of cells	No. of reversals	$A_0$	$\alpha$
0	-	72	599	-	-
10	0.0	80	705	2.33	-0.20
5	0.1	91	870	1.96	-0.32
	0.3	96	962	1.58	-0.56
	0.7	92	1073	1.59	-0.84
	1.5	99	1041	1.78	-0.45
	3.1	103	799	1.66	0.11

## 4.0 IMPLICATIONS OF RUN-REVERSE-FLICK CYCLE IN BACTERIAL CHEMOTAXIS

### 4.1 INTRODUCTION

Existing observations made in *E. coli* have shown that sensing and motility impose different requirements on bacterial chemotactic response [27, 22]. The debate on this interesting issue was initiated by the observation of Block, Segall, and Berg [18] who discovered that the experimentally measured chemotactic response function  $R(t)$  integrated over time  $t$  is zero. In physical terms  $R(t)$  can be thought as the Green's function of the chemotactic network when subjected to an impulsive or a  $\delta$ -in-time perturbation. The importance of this null integrated effect goes without saying, and was immediately recognized by the investigators as the bacterium's means of sensing. In their words [18], "the bacterium compares the information received in the past one second to that received over the previous three seconds." In effect, the double-lobe response function, which is displayed in Figure 4.1(C), allows the bacterium to react to fast temporal variations of a chemical signal  $c(t)$  but not to its dc component, enabling the cell to adapt to a wide range of chemical concentrations. Using a macroscopic diffusion argument, it was suggested by Schnitzer et al. [73] that a finite memory time is required for a bacterium to migrate in a linear chemical gradient; without the memory effect (or  $R(t) \simeq \delta(t)$ ), it was concluded that the chemotactic coefficient  $\kappa = V/\nabla c$  or the drift velocity  $V$  would be zero, where  $V$  is in the direction of the chemical gradient  $\nabla c$ . However, de Gennes pointed out that the macroscopic diffusion approach ignored important correlations between bacterial swimming and the underlying chemical gradient [29]. By taking into account such correlations, de Gennes showed that the optimal (or a fast) response for migration in a linear gradient is an exponential function with a decay rate determined

by the cell’s memory time  $\tau$ . He further pointed out that the double-lobe response function observed in *E. coli* could only reduce the migration speed in the gradient.

Contributing to this stimulating debate is the finding of Clark and Grant [27], who argued that while a cell needs a fast drift speed in a concentration gradient, it is equally important for the cell to localize once the top of the gradient is reached. They showed that the single-lobe function proposed by de Gennes is inadequate for cell localization. By imposing the co-requirements of being able to localize as well as to migrate, they demonstrated that the optimal response function is biphasic, which is in remarkably good agreement with the one measured in the experiment [18]. This observation led Clark and Grant to conclude that the biphasic response in *E. coli* perhaps reflects a compromised need of the cells in different environments. A recent study also suggested that the laboratory observed bacterial response corresponds to the maximin strategy that ensures the highest minimum uptake of nutrient for any profile of concentration [22].

As described in Section 1.1, the swimming pattern of the marine bacterium *V. alginolyticus* is a *cyclic 3-step* process [92], where a cell swims forward for a time interval  $\Delta_f$  and it then backtracks by reversing the motor direction for a time  $\Delta_b$ . Upon resuming forward swimming, the bacterial flagellum flicks causing the cell body to veer in a new direction. This type of motility pattern is very different from that of *E. coli*, which exhibit a run-tumble pattern. By way of introduction a typical trajectory of *V. alginolyticus* and that of *E. coli* are presented respectively in Figure 4.1(A) and (B). For the *V. alginolyticus*’ trajectory, Figure 4.1(A), the forward and the backward segments are designated by circles and squares, respectively. The last (flicking) step is functionally equivalent to a tumble in *E. coli*, allowing the bacterium to randomly select a direction, and a new cycle ensues. Despite the fact that run and reverse intervals,  $\Delta_f$  and  $\Delta_b$ , as well as the flicking angle  $\Delta\theta$  are stochastic, the 3-step cycle is deterministic and has been observed in different *V. alginolyticus* strains and in a swimming buffer with and without a chemical gradient [92]. In a steady state without a chemical gradient, we found that the probability density functions  $P(\Delta_b)$  and  $P(\Delta_f)$  are statistically independent and have long exponential tails (or a Poissonian-like behavior) with the mean intervals  $\tau_b \simeq \tau_f \simeq 0.3 s$ . However, when a point source of chemoattractant is present, the cells can quickly migrate along the gradient and form a tight pack around the

source.

The biochemical network that regulates the activity of *E. coli*'s motor is reasonably well understood [80]. While this is not the case for *V. alginolyticus*, it cannot deter our progress because we know that even for very diverse microorganisms, such as *E. coli* and *Bacillus subtilis* that are roughly one billion years apart according to a recently constructed phylogenetic tree [26], the fundamental mechanism of regulation is still similar, i.e. a ligand binding to a receptor triggers a cascade of chemical reactions. The end product of the reaction is a chemically modified protein, called the response regulator (CheY-P), that binds to the motor, causing it either to rotate CCW (*B. subtilis*) or CW (*E. coli*). The basic aim of different microorganisms is also the same, namely guided by chemical signals, the cell is directed towards the source of chemoattractant and away from chemorepellent. According to the phylogenetic tree [26], *V. alginolyticus* appears to be much closer to *E. coli* than *B. subtilis*, suggesting that there is much in common between these two bacterial species. Indeed in *V. alginolyticus*, one can identify chemotaxis genes that are largely homologous to *E. coli* with the exception of *cheV* that is absent in *E. coli* but is present in *B. subtilis*. A recent study moreover showed that the phosphorylated CheY in *V. alginolyticus* causes the polar flagellar motor to reverse direction from CCW to CW, similar to *E. coli* [47].

It is clear that the 3-step swimming pattern is significantly different from the well-studied 2-step swimming pattern of run and tumble, and it has strong implications for bacterial chemotaxis, which can be characterized by an effective diffusion coefficient  $D$  and a drift velocity  $V$  in the presence or absence of a chemical gradient. The calculation below illustrates that cells executing the 3-step swimming pattern can exhibit rich chemotactic behaviors, and the variations can be acted on by natural selection so that a particular response emerges. Below we will illustrate these new aspects of bacterial chemotaxis based on our findings of the 3-step process.

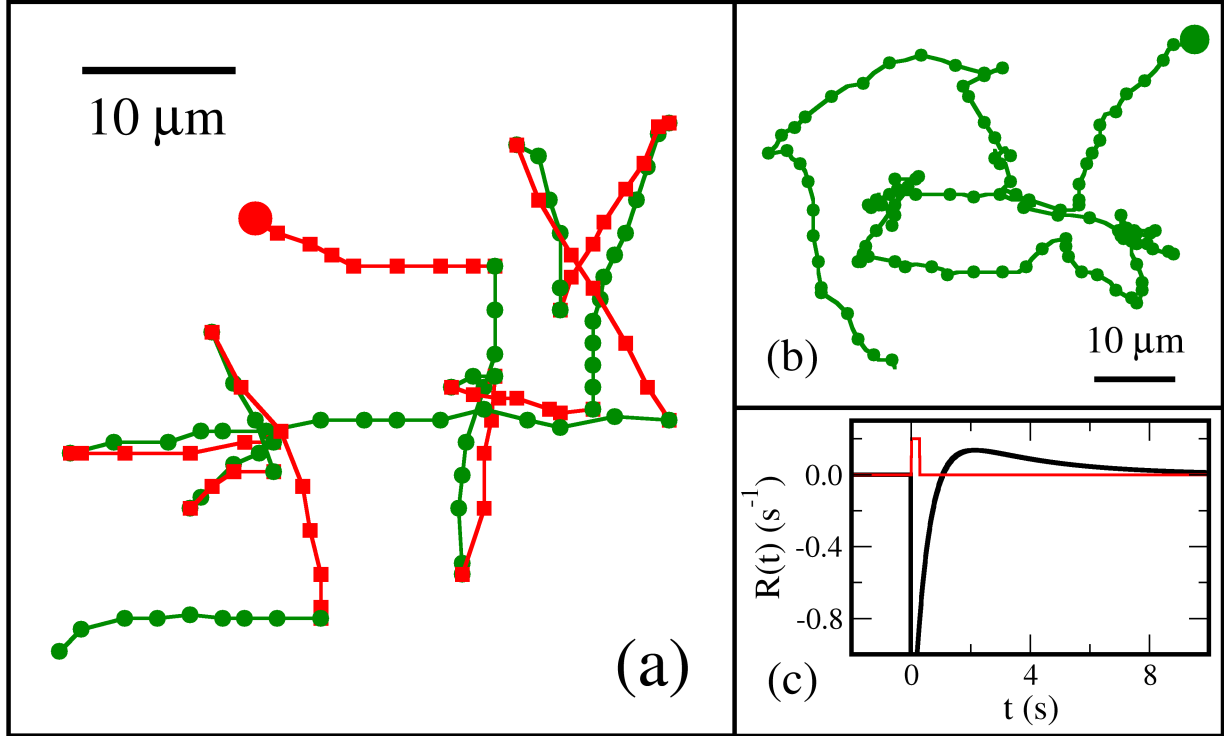


Figure 4.1: Bacterial swimming trajectories. Bacterial swimming trajectories of *V. alginolyticus* (A) and *E. coli* (B). The cells have been selected amongst many because they are more or less swimming in the focal plane, 50-100  $\mu\text{m}$  above the glass coverslip. The starting points for both trajectories are indicated by the two large solid dots. The time lapse between adjacent squares or circles are 0.067 s and 0.13 s for (A) and (B). The segments labeled by squares and circles in (A) designate the backward and forward swimming intervals, and transitions from backward to forward cause flicking, randomizing the swimming direction. Unlike a transition from forward to backward, which has a directional change  $\Delta\theta \simeq \pi$  (or backtracking), a backward to forward transition is random with  $\Delta\theta$  uniformly distributed between 0 and  $180^\circ$ . (C) A hypothetical response function  $R(t)$  of *E. coli* due to an impulse stimulation (the thin line) is plotted as the thick curve, where  $R(t) = R_0 \left[ \frac{1}{\tau_m} \exp\left(-\frac{t}{\tau_m}\right) - \frac{1}{\tau_z} \exp\left(-\frac{t}{\tau_z}\right) \right]$ . Here we set  $R_0 = 1$  and used the typical *E. coli* methylation time ( $\tau_m = 3$  s) and phosphorylation time ( $\tau_z = 0.5$  s) [86, 74].

## 4.2 RESULTS

Similar to cells of *E. coli*, the flagellar motor of *V. alginolyticus* has two lifetimes for the state of rotations: one ( $\tau_f$ ) for the CCW interval and one ( $\tau_b$ ) for the CW interval, where the subscripts  $f$  and  $b$  stand for forward and backward swimming, respectively. To modulate their chemotactic behaviors, these lifetimes are affected by the local concentration of chemoeffectors and cells' adaptation mechanism. Unlike *E. coli*, however, CW rotation in *V. alginolyticus* causes the cell to backtrack. Both swimming intervals are expected to depend on the ligand concentration  $c(t)$ , which we assume to be chemoattractant. For small  $c(t)$ , we assume that a linear response is applicable and hence,

$$\frac{1}{\tau_f(t)} = \frac{1}{\tau_f} \left[ 1 - \int_{-\infty}^t dt' R_f(t-t')c(t') \right], \quad (4.1)$$

$$\frac{1}{\tau_b(t)} = \frac{1}{\tau_b} \left[ 1 - \int_{-\infty}^t dt' R_b(t-t')c(t') \right], \quad (4.2)$$

where  $\tau_f$  and  $\tau_b$  are the steady-state values, and  $R_f(t)$  and  $R_b(t)$  are the memory (or the response) functions, which are not necessarily the same for the two swimming intervals. In the above, an exposure to the ligand causes the forward lifetime to increase, and is consistent with our observations in *V. alginolyticus* [92]. Linearity of Eqs. 4.1 and 4.2 suggests that it is possible to examine one delay time  $\theta$  at a time and sum up all possible delays at the end. Following de Gennes, we write  $R_s(t) = \alpha_s \delta(t - \theta)$ , where the strength of the response  $\alpha_s$  ( $s = f, b$ ) has the dimension of volume. Next, we consider a cell moving in a chemical gradient as depicted in Figure 4.2. Our aim is to calculate the displacement  $x_i$  along the gradient in one cycle,  $\Delta_f + \Delta_b$ , which leads to a mean drift velocity  $V = \bar{x}_i/(\tau_f + \tau_b)$  after averaging over  $\Delta_f$  and  $\Delta_b$ . Because a cell randomizes its swimming direction at the end of the backward interval by a flick, the motions in two consecutive cycles are uncorrelated. This allows us to place the origin of time ( $t = 0$ ) at the beginning of the forward run. Assuming that the forward run time is Poisson distributed, the surviving probability of a cell swimming

forward up to  $\Delta_f$  is given by,

$$P_f(\Delta_f) = \exp \left[ - \int_0^{\Delta_f} dt' \frac{1}{\tau_f(t')} \right] \simeq \exp \left( - \frac{\Delta_f}{\tau_f} \right) \left[ 1 + \frac{\alpha_f}{\tau_f} \int_{-\theta}^{\Delta_f - \theta} dt' c(t') \right], \quad (4.3)$$

and the probability that it stops immediately after  $\Delta_f$  is  $-\partial P_f(\Delta_f)/\partial \Delta_f$ . Likewise, the surviving probability of a cell swimming backwards from  $\Delta_f$  to  $\Delta_f + \Delta_b$  is given by,

$$P_b(\Delta_b, \Delta_f) = \exp \left[ - \int_{\Delta_f}^{\Delta_f + \Delta_b} dt' \frac{1}{\tau_b(t')} \right] \simeq \exp \left( - \frac{\Delta_b}{\tau_b} \right) \left[ 1 + \frac{\alpha_b}{\tau_b} \int_{\Delta_f - \theta}^{\Delta_f + \Delta_b - \theta} dt' c(t') \right], \quad (4.4)$$

and the stopping probability at the end of the backward run is  $-\partial P_b(\Delta_b, \Delta_f)/\partial \Delta_b$ . It follows that the net mean displacement in one cycle is given by,

$$\begin{aligned} \bar{x}_i \equiv \bar{x}_{fi} + \bar{x}_{bi} &= \left\langle \int_0^{\infty} d\Delta_f \left( - \frac{\partial P_f(\Delta_f)}{\partial \Delta_f} \right) v_{fi} \Delta_f \right\rangle \\ &+ \left\langle \int_0^{\infty} d\Delta_f \left( - \frac{\partial P_f(\Delta_f)}{\partial \Delta_f} \right) \int_0^{\infty} d\Delta_b \left( - \frac{\partial P_b(\Delta_b, \Delta_f)}{\partial \Delta_b} \right) v_{bi} \Delta_b \right\rangle, \end{aligned} \quad (4.5)$$

where  $\bar{x}_{fi}$  and  $\bar{x}_{bi}$  represent respectively the mean displacement during the forward ( $\Delta_f$ ) and the backward ( $\Delta_b$ ) swimming interval, and  $\langle \dots \rangle$  designates the angular average for  $v_{fi}$  and  $v_{bi}$ . For the linear gradient depicted in Figure 4.2, the concentration experienced by the cell can be represented as  $c(t) = c_0 + \nabla c \cdot v_{fi} \cdot t$  for  $0 \leq t < \Delta_f$  and  $c(t) = c_0 + \nabla c \cdot v_{fi} \cdot \Delta_f + \nabla c \cdot v_{bi} \cdot (t - \Delta_f)$  for  $\Delta_f \leq t < \Delta_f + \Delta_b$ . Since  $c_0$  is determined by the velocity in the previous cycle, it does not contribute to the above integrations after angular averaging. Although the calculation of Eq. 4.5 is tedious, and is given in Appendix B, the final result is straightforward:

$$\begin{aligned} \bar{x}_i &= \left\{ \alpha_f \tau_f^2 \langle v_{fi}^2 \rangle \exp \left( - \frac{\theta}{\tau_f} \right) \right. \\ &\left. + \alpha_b \left[ \frac{\tau_f^2 \tau_b^2}{\tau_f - \tau_b} \langle v_{fi} v_{bi} \rangle \left( \frac{1}{\tau_b} \exp \left( - \frac{\theta}{\tau_f} \right) - \frac{1}{\tau_f} \exp \left( - \frac{\theta}{\tau_b} \right) \right) + \tau_b^2 \langle v_{bi}^2 \rangle \exp \left( - \frac{\theta}{\tau_b} \right) \right] \right\} \nabla c. \end{aligned} \quad (4.6)$$

The first term in the curly brackets of Eq. 4.6 is the displacement during the forward interval, and the second term is the displacement during the backward interval. It is noteworthy that during the second interval, there is a cross term proportional to  $\frac{\tau_f^2 \tau_b^2}{\tau_f - \tau_b} \langle v_{fi} v_{bi} \rangle (\dots)$ , which results from the delay, i.e., even though the cell is moving backwards, in the early episode of

that interval, the cell still remembers the concentration sensed during the previous forward swimming. This gives rise to anti-correlation, since  $\langle v_{fi}v_{bi} \rangle < 0$ , that contributes to a negative displacement. This important correlated motion adds richness to bacterial chemotaxis and is what makes *V. alginolyticus* behave differently from *E. coli*.

We noted that in the limit of no memory,  $\theta \rightarrow 0$ , Eq. 4.6 yields the result  $\bar{x}_i = [\alpha_f \tau_f^2 \langle v_{fi}^2 \rangle + \alpha_b \tau_b (\tau_b \langle v_{bi}^2 \rangle + \tau_f \langle v_{fi}v_{bi} \rangle)] \nabla c$ . It is interesting that even when there is no memory, the cross term survives because there is no direction randomization after a forward run. Moreover, the displacement during the backward interval, can contribute positively or negatively to the net mean displacement, depending on the response  $\alpha_b$ , the mean lifetimes  $\tau_f$  and  $\tau_b$ , and the swimming velocities  $\vec{v}_f$  and  $\vec{v}_b$ . In particular, if the regulation in the backward interval is independent of the regulation in the forward interval, a case that will be further discussed below, the displacement in both swimming intervals can be positive. In comparison, for *E. coli*  $\bar{x}_i = \alpha_f \tau_f^2 \langle v_{fi}^2 \rangle \nabla c$  when  $\theta \rightarrow 0$ , where the subscript  $f$  stands for the forward run (or CCW rotation). Because no motility is produced during the CW interval, which takes up 20 – 50% of the swimming cycle [48, 18], one expects that *E. coli* will migrate slower than *V. alginolyticus* in a linear gradient if everything else is equal. Using  $v_{fi} = -v_{bi} = v_i$  and summing up all possible delays in Eq. 4.6, we found that the mean displacement is given by,

$$\begin{aligned} \bar{x}_i = & \left\{ \tau_f^2 \int_0^\infty d\theta R_f(\theta) \exp\left(-\frac{\theta}{\tau_f}\right) + \tau_b^2 \int_0^\infty d\theta R_b(\theta) \right. \\ & \left. \times \left[ \exp\left(-\frac{\theta}{\tau_b}\right) - \frac{\tau_f^2}{\tau_f - \tau_b} \left( \frac{1}{\tau_b} \exp\left(-\frac{\theta}{\tau_f}\right) - \frac{1}{\tau_f} \exp\left(-\frac{\theta}{\tau_b}\right) \right) \right] \right\} \langle v_i^2 \rangle \nabla c. \end{aligned} \quad (4.7)$$

The average drift speed in the gradient is  $V(\equiv \kappa \nabla c) = \bar{x}_i / (\tau_f + \tau_b)$ , which allows the chemotactic coefficient  $\kappa$  to be calculated. In *E. coli*,  $\kappa$  is proportional to the diffusion coefficient  $D \simeq \frac{1}{3} \phi_0 \langle v^2 \rangle \tau_f$  and one finds  $\kappa = D \int_0^\infty R_f(\theta) \exp\left(-\frac{\theta}{\tau_f}\right) d\theta$ . Based on a dimensional argument, the “diffusivity” of the 3-step swimmer is given by:

$$D = \langle v_i^2 \rangle \frac{(\tau_f - \tau_b)^2}{\tau_f + \tau_b} = \frac{1}{3} \langle v^2 \rangle \frac{(\tau_f - \tau_b)^2}{\tau_f + \tau_b}, \quad (4.8)$$

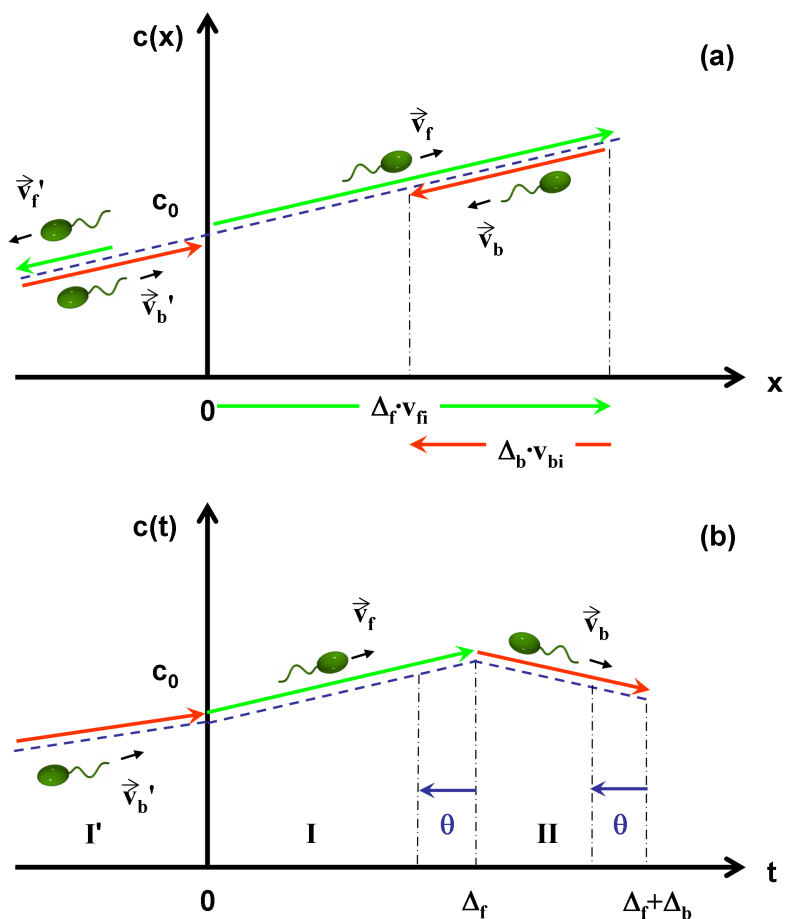


Figure 4.2: Migration of *V. alginolyticus* in a linear chemical gradient. (A) In the spatial domain, the chemical gradient is specified by the dashed line. The arrows indicate the forward and the backward swimming segments along the gradient.  $\Delta_f$  and  $\Delta_b$  are respectively the forward and backward swimming time intervals, and  $v_{fi}$  and  $v_{bi}$  are respectively the forward and backward velocity components along the chemical gradient. Note that backtracking means  $\vec{v}_b = -\vec{v}_f$ . (B) The bacterial chemotactic network processes the chemical information in the temporal domain, and the concentration detected by the cell is depicted in (B), where  $\theta$  is the memory time of the bacterium. I and II are chemosensing in the current cycle, and I' is due to the previous cycle.

and the chemotaxis coefficient can be written as

$$\kappa = \frac{D}{(\tau_f - \tau_b)^2} \left\{ \tau_f^2 \int_0^\infty d\theta R_f(\theta) \exp\left(-\frac{\theta}{\tau_f}\right) + \tau_b^2 \int_0^\infty d\theta R_b(\theta) \left[ \exp\left(-\frac{\theta}{\tau_b}\right) - \frac{\tau_f^2}{\tau_f - \tau_b} \left( \frac{1}{\tau_b} \exp\left(-\frac{\theta}{\tau_f}\right) - \frac{1}{\tau_f} \exp\left(-\frac{\theta}{\tau_b}\right) \right) \right] \right\}. \quad (4.9)$$

This calculation leads to two possible scenarios (or fundamental hypotheses) for bacterial chemotaxis: (i) independent and (ii) shared chemosensing.

### 4.2.1 Independent Chemosensing

In the first case, the response functions in the forward and backward intervals are independent, i.e.,  $R_f(\theta)$  and  $R_b(\theta)$  have different functional forms, so that the sensing system breaks the time reversal symmetry. In order to achieve such a control, the flagellar motor cannot only passively receive signals from the chemotaxis network but instead the status of the motor must be made known to the chemotaxis regulatory network. This may be attained either by the flagellar motor being a part of the regulatory network or by a feedback signal via a protein that can reset the chemotactic response. In short, there will be a back flow of information from the motor to the chemotaxis network in addition to the normal chemotaxis regulation. To optimize the drifting velocity, we applied a variational principle to Eq. 4.9, which is delineated in Appendix C. We used the constraints that  $R_f(\theta)$  and  $R_b(\theta)$  have constant variances  $\sigma_s^2/\tau_s$  ( $s = f, b$ ) [27], yielding

$$R_f(\theta) \propto \frac{\sigma_f}{\tau_f} \exp\left(-\frac{\theta}{\tau_f}\right), \quad (4.10)$$

$$R_b(\theta) \propto \frac{\sigma_b}{\tau_b} \left[ \exp\left(-\frac{\theta}{\tau_b}\right) - \frac{\tau_f^2}{\tau_f - \tau_b} \left( \frac{1}{\tau_b} \exp\left(-\frac{\theta}{\tau_f}\right) - \frac{1}{\tau_f} \exp\left(-\frac{\theta}{\tau_b}\right) \right) \right]. \quad (4.11)$$

It is evident from the optimization procedure that in order to attain the maximum possible drifting speed, the forward response function  $R_f(\theta)$  should be monophasic but the backward response function  $R_b(\theta)$  can be either monophasic or biphasic, depending on the ratio of the two lifetimes,  $\beta \equiv \tau_b/\tau_f$ . Figure 4.3 displays  $(\tau_f/\sigma_f)R_f(\theta)$  and  $(\tau_b/\sigma_b)R_b(\theta)$

for different values of  $\beta = 0.8, 1.2, 1.5, 1.8,$  and  $2.4$ . The figure shows that the biphasic response becomes more biased towards the negative lobe as  $\beta$  decreases towards unity, and it disappears altogether for  $\beta < 1$ , where the response is negative for all  $\theta$ . An analysis shows that the biphasic response occurs in a narrow range of  $\beta$  ( $1 \leq \beta \leq 2$ ), and outside this range the response is always monophasic. This behavior is understandable since when  $\tau_b$  is shorter than  $\tau_f$ , the backward interval is strongly influenced by the signal sensed in the previous forward interval due to the memory effect. To deal with this inconsistency between sensing and motility, the optimal strategy is a negative monophasic response as depicted by the lowest curve ( $\beta = 0.8$ ) in Figure 4.3. On the other hand, when  $\tau_b$  is longer than  $\tau_f$ , the cell would have consistent sensing and motility so that a monophasic positive response is more favorable, which is shown by the top solid curve ( $\beta = 2.4$ ) in Figure 4.3. In the limiting case  $\tau_b \gg \tau_f$  or  $\tau_b \ll \tau_f$ , Eqs. 4.9, 4.10, and 4.11 make it clear that the chemotactic coefficient  $\kappa$  is dominated respectively by the backward or the forward swimming interval. The situation is formally equivalent to *E. coli* chemotaxis, where the monophasic response is optimal for fast migration in a linear chemical gradient as was concluded by de Gennes [29].

#### 4.2.2 Shared Chemosensing

In the case of shared chemosensing, the bacterium uses a single response function  $R(\theta)$ , albeit the amplitudes of the responses may be different in the two directions,  $R_f(\theta) = R_b(\theta)/\gamma = R(\theta)$ . A simple reason for  $\gamma \neq 1$  could be due to different swimming speeds  $v_f$  and  $v_b$ , but other possibilities may also exist. For this type of sensing, there is no breaking of time reversal symmetry since the chemotaxis network processes the received information during the forward and the backward interval equally, and there is no need for a back flow of information. Using Eq. 4.9, we found:

$$\begin{aligned} \kappa = & \frac{D}{(\tau_f - \tau_b)^2} \int_0^\infty d\theta R(\theta) \left\{ \tau_f^2 \exp\left(-\frac{\theta}{\tau_f}\right) \right. \\ & \left. + \gamma \tau_b^2 \left[ \exp\left(-\frac{\theta}{\tau_b}\right) - \frac{\tau_f^2}{\tau_f - \tau_b} \left( \frac{1}{\tau_b} \exp\left(-\frac{\theta}{\tau_f}\right) - \frac{1}{\tau_f} \exp\left(-\frac{\theta}{\tau_b}\right) \right) \right] \right\}. \end{aligned} \quad (4.12)$$

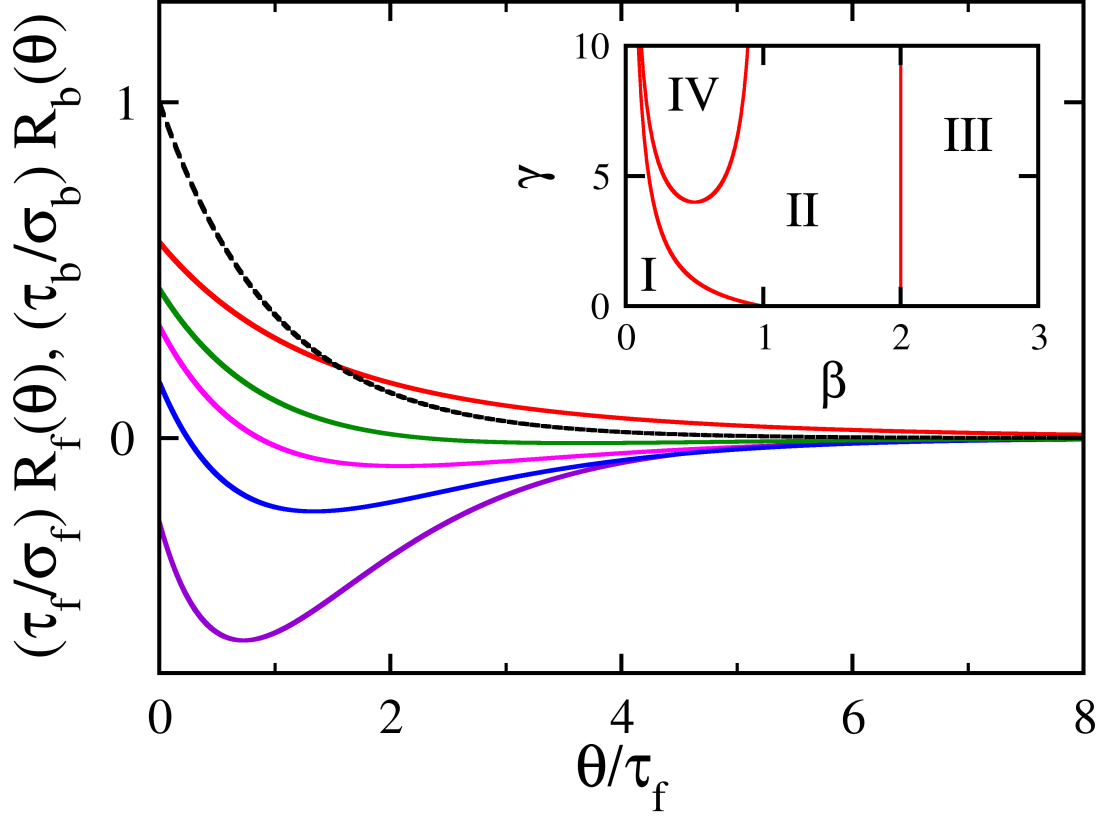


Figure 4.3: Chemotactic strategy I. The bacterium uses separate response functions,  $R_f(\theta)$  and  $R_b(\theta)$ , for chemosensing. The figure shows the dimensionless forms of the response functions. Here the dashed curve is for  $R_f(\theta)$ , and the solid curves, from bottom to top, are for  $R_b(\theta)$  with  $\beta(\equiv \tau_b/\tau_f) = 0.8, 1.2, 1.5, 1.8,$  and  $2.4$ , respectively. The inset is the phase diagram for chemotactic strategy II. It displays the phase boundaries between monophasic (I, III, IV) and biphasic (II) response regimes when the chemotaxis response obeys the relation  $R(\theta) = R_f(\theta) = R_b(\theta)/\gamma$ .

Applying the variational principle again (see Appendix C), we found that the drift velocity is optimized by the following response function

$$R(\theta) \propto \frac{\sigma}{\tau_f + \tau_b} \left\{ \exp\left(-\frac{\theta}{\tau_f}\right) + \gamma \left(\frac{\tau_b}{\tau_f}\right)^2 \left[ \exp\left(-\frac{\theta}{\tau_b}\right) - \frac{\tau_f^2}{\tau_f - \tau_b} \left( \frac{1}{\tau_b} \exp\left(-\frac{\theta}{\tau_f}\right) - \frac{1}{\tau_f} \exp\left(-\frac{\theta}{\tau_b}\right) \right) \right] \right\}. \quad (4.13)$$

As displayed in Figure 4.4,  $R(\theta)$  can be monophasic or biphasic depending on  $\gamma$  as well as the time ratio  $\beta \equiv \tau_b/\tau_f$ . The biphasic regime is bounded by  $\frac{1-\beta}{\beta} \leq \gamma < \frac{1}{\beta(1-\beta)}$  for  $0 \leq \beta < 1$  and  $\gamma \geq 0$  for  $1 < \beta \leq 2$ , which is displayed in the inset of Figure 4.3. The inset shows that the parameter space  $(\gamma, \beta)$  consists of four different regimes with I, III, and IV being monophasic and II biphasic. Our theory hence predicts that if a bacterium uses a single response function, for very short ( $\beta \ll 1$ ) or very long ( $\beta \gg 1$ ) backward swimming intervals, the biphasic response is not a good chemotactic strategy for migration in a linear chemical gradient. The biphasic response emerges only when  $\tau_f$  and  $\tau_b$  being close (or  $\beta \simeq 1$ ), which is the case in *V. alginolyticus* [92]. It is conspicuous that in the limits  $\beta \rightarrow 1$  and  $\gamma \rightarrow 1$ ,  $R(\theta)$  calculated using Eq. 4.13 is identical to the solution of a critically damped harmonic oscillator, which has the interesting property of  $\int_0^\infty (1 - \theta/\tau) \exp(-\theta/\tau) d\theta = 0$ , i.e., the response is “precisely” adaptive.

### 4.3 DISCUSSION

The above two hypotheses are testable by laboratory experiments where the bacteria are subject to a defined chemical stimulation, and one measures the switching rate  $S(t) = 2/(\tau_f(t) + \tau_b(t))$  and the forward swimming bias  $\Phi(t) = \tau_f(t)/(\tau_f(t) + \tau_b(t))$  as a function of time. For a weak stimulation, the above calculation allows us to find,

$$S(t) = S_0 \left[ 1 - \Phi_0 \int_{-\infty}^t R_f(t-t')c(t')dt' - (1 - \Phi_0) \int_{-\infty}^t R_b(t-t')c(t')dt' \right], \quad (4.14)$$

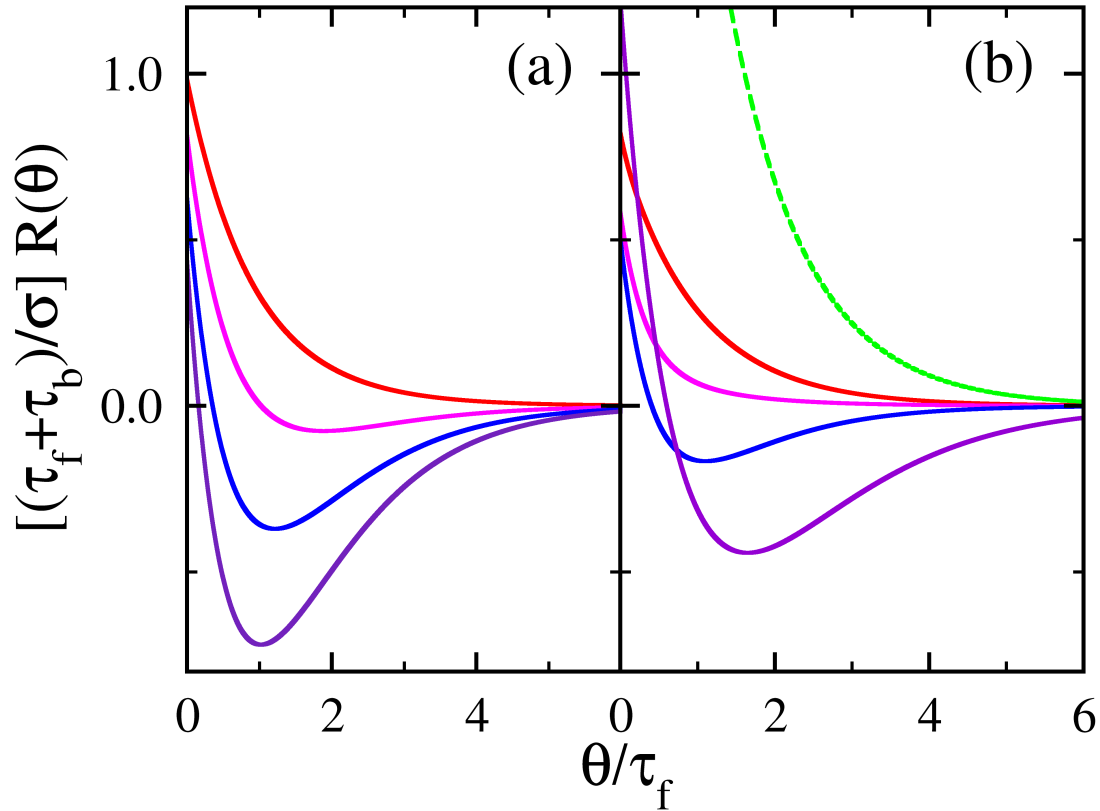


Figure 4.4: Chemotactic strategy II. The bacterium shares the same response function  $R(\theta) = R_f(\theta) = R_b(\theta)/\gamma$  for the forward and backward swimming intervals. In (A),  $\beta = 0.75$  and from top to bottom  $\gamma = 0.1, 1.0, 2.0,$  and  $3.0$ . In (B), the dashed line is for  $\gamma = 2$  and  $\beta = 2.0$ . The solid curves are for  $\gamma = 2$  and from top to bottom  $\beta = 0.1, 0.3, 0.5,$  and  $1.0$ . As can be seen, for fixed  $\beta \simeq 0.75$ , the response becomes strongly biphasic as  $\gamma$  increases. On the other hand, for fixed  $\gamma = 2$ , the response is monophasic for small  $\beta$ , and becomes biphasic for intermediate values of  $\beta$ , and returns to monophasic for  $\beta \geq 2$ .

$$\Phi(t) = \Phi_0 \left[ 1 + (1 - \Phi_0) \int_{-\infty}^t (R_f(t - t') - R_b(t - t')) c(t') dt' \right], \quad (4.15)$$

where  $S_0 \equiv 2/(\tau_f + \tau_b)$  and  $\Phi_0 \equiv \tau_f/(\tau_f + \tau_b)$  are the steady-state switching rate and the forward bias, respectively. The expressions are significantly simplified if the perturbation is  $\delta$ -in-time,  $c(t) = c'\delta(t)$ , and they are given by,

$$S(t) = S_0 [1 - c' (\Phi_0 R_f(t) + (1 - \Phi_0) R_b(t))], \quad (4.16)$$

$$\Phi(t) = \Phi_0 [1 + c'(1 - \Phi_0) (R_f(t) - R_b(t))]. \quad (4.17)$$

The calculation shows that if the second scenario is true and  $R_f(t) \simeq R_b(t)$ , the forward bias will be weakly dependent on time  $t$ , and the switching rate is simply given by  $S(t) \simeq S_0[1 - c'R_f(t)]$ . However, if the first scenario is true, the measured  $S(t)$  and  $\Phi(t)$  can be used to find the response function  $R_f(t)$  and  $R_b(t)$  using Eqs. 4.16 and 4.17. In this case, the following simple relations result,

$$R_f(t) = \frac{1}{c'} \left[ \frac{\Phi(t)}{\Phi_0} - \frac{S(t)}{S_0} \right], \quad (4.18)$$

$$R_b(t) = \frac{1}{c'} \left[ \frac{1 - \Phi(t)}{1 - \Phi_0} - \frac{S(t)}{S_0} \right]. \quad (4.19)$$

An alternative and perhaps more direct way to find  $R_f(t)$  and  $R_b(t)$  is to perform a conditional stimulation on individual cells. The bacterium can be either tethered to a surface, such as in Block et al.'s experiment [18], or freely swimming, as in Khan et al.'s experiment [44]. For tethered cells, one can apply a pulse of chemoattractant at the moment the motor switches from CW (CCW) to CCW (CW), and record the subsequent swimming interval  $\Delta_{1f}$  ( $\Delta_{1b}$ ), where the subscript 1 emphasizes the interval before the first switch. By counting the switching events up to time  $t$ , one can construct a cumulative PDF (normalized by the total number of cells)  $\Psi_s(t)$ , and the time-dependent switching rate can be obtained according to  $\tau_s^{-1}(t) = -\frac{d}{dt} \ln(1 - \Psi_s(t))$ , where  $s = f$  or  $b$ . For freely swimming cells, one can use photo-active serine, which is an attractant to *V. alginolyticus*, to stimulate cells. If the first

scenario is true, one should find that  $\tau_f^{-1}(t)$  and  $\tau_b^{-1}(t)$  have different time dependence or equivalently  $R_f(t)$  and  $R_b(t)$  have different functional forms. However, if the second scenario is true, there should be not much difference between  $\tau_f^{-1}(t)$  and  $\tau_b^{-1}(t)$  or  $R_f(t) \propto R_b(t)$ .

To conclude, the 3-step motility pattern of *V. alginolyticus* allows significant variations in bacterial chemotactic behaviors. These variations can be acted on by natural selection and give rise to distinct phenotypes observed in the wild. Compared to the 2-step swimming pattern of *E. coli*, *V. alginolyticus* can engage in chemosensing and migration in both the forward and the backward swimming intervals, and hence their “duty cycle” is  $\sim 100\%$  as compared to  $\sim 50 - 80\%$  in *E. coli* [18, 48]. Thus, given a proper regulation in the backward swimming interval, *V. alginolyticus* can migrate in a chemical gradient more efficiently than their *E. coli* counterparts. An important aspect in 3-step chemotaxis is backtracking that gives those bacteria heading down a gradient an opportunity to re-exploit what they find a moment earlier. In our opinion, the full duty cycle, backtracking, and flicking are defining characteristics of *V. alginolyticus*. These significant niches are likely selected for by the ocean environment where a quick response to transitory signals is important. We showed that for a swimmer executing the cyclic 3-step motility pattern, a biphasic response arises naturally without the need to invoke cell localization as suggested for *E. coli* [27]. Moreover, we showed that the biphasic response is most effective when the forward  $\tau_f$  and the backward  $\tau_b$  swimming intervals are comparable. This makes biological sense since a brief forward or a brief backward interval contributes little to motility, and consequently a monophasic response is sufficient for migration. This also raises the interesting question why the non-motile CW interval in *E. coli* is so long, taking up at least 20% of the duty cycle. If tumbling is just to change the direction, would not it be better if CW interval is shorter? An interesting possibility is that the ancestral cell that gave “birth” to *E. coli* and *V. alginolyticus* was a 3-step swimmer. However, when *E. coli* became specilized in a different environment, which favored multiple flagella for motility, they gave up backtracking and flicking, resulting in a tumbly movement. In this view, then, it is not surprising that *E. coli*’s tumbling interval is long and its chemotactic response is biphasic.

Based on motility alone, we propose two different mechanisms, independent and shared chemosensing, by which cells of *V. alginolyticus* can optimize their migration speed in a

linear gradient. Interestingly, the biphasic response appears in both types of chemotactic strategies. The experiment that will be discussed in the next chapter illuminates how the two motor states are regulated after a stimulation.

## 5.0 ASYMMETRIC RESPONSES OF FORWARD AND BACKWARD SWIMMERS

### 5.1 INTRODUCTION

When an *E. coli* cell is given a pulse of chemoattractant, its CCW bias  $\Phi(t)$  increases initially, it then decreases below its steady-state level  $\Phi_0$  in  $\sim 1$  s, before relaxing towards  $\Phi_0$  in 3–4 s (see the inset of Figure 5.1(A)). This finding, discovered nearly 30 years ago by Berg and coworkers [18, 74], is fundamental to bacterial chemotaxis and has been successfully explained by models that take into account cooperativity of chemoreceptors [78, 30, 86] and robust adaption in the regulatory network of *E. coli* [3]. However, how general this behavior is among different bacteria is not known, and has invited much speculations about its biological origin and usefulness in chemotaxis. Pierre-Gilles de Gennes showed that if the main goal of the bacterium is to reach the chemical source as rapidly as possible, a monophasic response will do better than the experimentally observed biphasic response [29]. However, it was subsequently shown by Clark and Grant [27] that the monophasic response would not allow the cell to localize if needed. Paradoxically, it was shown by these investigators that the monophasic response will cause the bacteria to accumulate in the low chemoattractant region in long times. Clark and Grant recognized that cell localization is just as important as directed motility and proposed that the biphasic response seen in *E. coli* might reflect such dual requirements. Indeed, their theoretical analysis lends strong support to their hypothesis and the calculated response function was in good agreement with the measured one (see the solid line in the inset of Figure 5.1(A)).

*V. alginolyticus*' ability to backtrack significantly enhances its ability to localize near a point source as demonstrated in our recent experiment [92]. It was shown that *V. alginolyti-*

*cus* could not only rapidly form a compact cluster near a point source of chemoattractant but also had the cluster size five times smaller than that of *E. coli* despite their high swimming speed. Heuristically, this can be explained by means of bacterial “diffusivity”  $D$ , which can be calculated based on the observed 3-step motility pattern:  $D = v_{sw}^2 \langle (\Delta_f - \Delta_b)^2 \rangle / 6 \langle (\Delta_f + \Delta_b) \rangle$ , where  $v_{sw} \approx 50 \mu\text{m/s}$  is the cell’s swimming speed, and  $\Delta_f$  and  $\Delta_b$  are the forward and the backward intervals in a given swimming cycle [91]. For a bacterium to localize i.e.  $D \approx 0$ , it only requires that  $\Delta_f$  and  $\Delta_b$  are kept approximately the same near the source, which was indeed observed in *V. alginolyticus* [92]. Hence, it is not clear whether the biphasic response is necessary or even helpful for *V. alginolyticus*’ localization near a source of attractant.

While de Gennes’ approach (delineated in Chapter 4) is appealing, its utility to 3-step swimmers is questionable. In Chapter 4, we hypothesized that because of the reverse step, *V. alginolyticus* can readily localize and thus the primary aim of the chemotaxis response for this microorganism is to migrate as rapidly as possible in a chemical gradient. We derived the response function(s) for a 3-step swimmer who senses the environment continuously using a single response function or two separate response functions for the forward and backward intervals, respectively (see Section 5.2). In the former case, the regulatory network does not differentiate the swimming direction, which may be called shared sensing, and in the latter case, the network regulates the two intervals autonomously, which may be called independent sensing. We were surprised to find that over a broad range of parameters, such as the forward  $\tau_f (\equiv \langle \Delta_f \rangle)$  and the backward  $\tau_b (\equiv \langle \Delta_b \rangle)$  swimming intervals, a biphasic response with a positive and a negative lobe arises naturally for the 3-step swimmer [6].

The aim of this work is to check which of the above two hypotheses, shared vs. independent sensing, is adopted by the marine bacterium. We conducted our measurement using an optical trapping technique that allows us to determine both the switching rate  $S(t)$  and the rotational bias  $\Phi(t)$  in individual cells. Using conditional stimulations, we found that *V. alginolyticus* perform chemotaxis using two separate response functions. We also found that while the forward response is biphasic with a positive lobe followed by a negative lobe, the backward response is monophasic. These findings have strong implications for molecular events in the chemotaxis network and for the chemotaxis behaviors of the cells in a marine environment.

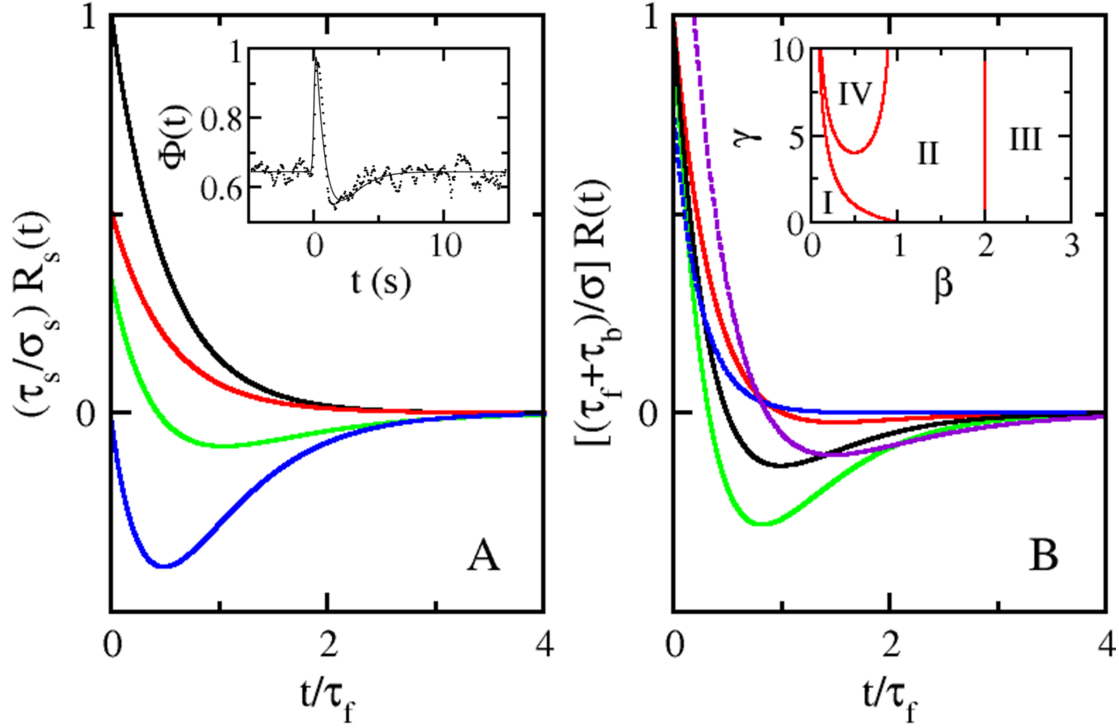


Figure 5.1: Response functions for independent and shared chemosensing revisited. Response functions for independent (A) and shared (B) chemosensing. In both (A) and (B), we assume  $\tau_f = 0.5$  s to be fixed. For independent sensing (A), the forward response  $R_f(t)$  (black curve) is monophasic with a single time constant  $\tau_f$ . The backward response  $R_b(t)$  on the other hand is biphasic characterized by two time constants  $\tau_f$  and  $\tau_b$ . Depending on  $\beta \equiv \tau_b/\tau_f$ ,  $R_b(t)$  could have either a single negative lobe (blue curve with  $\beta \lesssim 1$ ), a single positive lobe (red curve with  $\beta \gtrsim 2$ ), or an initial positive lobe preceding a negative lobe (green curve with  $\beta = 1.5$ ). In the inset, the solid dots represent the CCW bias measured by Block et al. [18] for the *E. coli* stimulated impulsively at  $t = 0$ . The solid line is the fit using Clark and Grant's theory [27]. For shared sensing (B), there is only one response function  $R(t)$  that is characterized by two time constants,  $\tau_f$  and  $\tau_b$ . Some representative response curves are plotted using different colored lines. For  $\beta \lesssim 1$ , with increasing  $\gamma (\equiv R_b(t)/R_f(t))$ , the negative lobe becomes more prominent as shown by the red, black, and green curves corresponding to  $\gamma = 0.5, 1.0$ , and  $1.5$ , respectively. For  $\gamma = 1$ , while the black ( $\beta \lesssim 1$ ) and the purple ( $\beta = 1.5$ ) curves have two lobes, the blue ( $\beta = 0.5$ ) curve has only a single positive lobe. The inset summarizes different responses for a range of parameters  $\beta$  and  $\gamma$ . Here, in regions I and III,  $R(t)$  has a single positive lobe; in IV, it has a single negative lobe; and in II, it has an initial positive and a long-time negative lobe. Note that the biphasic regime (II) is broad and the 3-step swimmer *V. alginolyticus* is operating in this range as indicated by the black cross.

## 5.2 THEORY

The quantity we seek to determine is the bacterial chemotaxis response function  $R(t)$  to a *brief* and *weak* stimulation. This function is biologically important because it can reveal on the one hand the inner working of chemotaxis regulatory network, and on the other hand how this function is shaped by environmental and evolutionary forces. Moreover, if the regulatory system is linear,  $R(t)$  can also be used to predict bacterial behaviors in a complex environment.

It is evident that de Gennes' conclusion that a biphasic response is not advantageous for the migration speed in a linear chemical gradient is valid for a microorganism executing the run-tumble motility pattern. The same conclusion cannot be drawn for *V. alginolyticus* because of its very different motility pattern. This makes one to wonder what would be the optimal response for the cell to perform chemotaxis efficiently. To find out we generalized de Gennes' calculation to the case of 3-step swimmers, which is described in details in Chapter 4. Below, the key steps and the central results will be restated.

Since *V. alginolyticus* produce motility in both forward and backward swimming intervals, it can admit two different response functions, one for the forward  $R_f(t)$  and one for the backward  $R_b(t)$ . This allows us to postulate two fundamental hypotheses for bacterial chemotaxis for the 3-step swimmers: (i) independent chemosensing and (ii) shared chemosensing. In the first scenario, the bacterium uses different response functions,  $R_f(t)$  and  $R_b(t)$ , for migration in a chemical gradient. In the second scenario,  $R_f(t)$  and  $R_b(t)$  can differ only in the amplitude,  $R(t) (\equiv R_f(t) = R_b(t)/\gamma)$ , where  $\gamma$  is constant. It is evident that (ii) is more restrictive than (i) and thus given everything being equal, the independent sensing should produce a higher drift velocity in a linear gradient. However, independent sensing is more costly to the bacterium because for this scheme to be effective, there must be an information back-flow from the motor to the regulatory network to inform its current status. This would require additional chemical steps and possibly new proteins in the regulatory network.

Our calculation is based on the Poisson surviving probability defined as [29],

$$P_s(\Delta_s) = \exp \left[ - \int_0^{\Delta_s} dt' k_s(t') \right], \quad (5.1)$$

where  $\Delta_s$  is the persistence time while swimming forward ( $s = f$ ) or backward ( $s = b$ ), and the switching rate  $k_s(t)$  is a function of the chemoeffector concentration  $c(t)$ . For a weak signal, we can assume a linear response so that,

$$k_s(t) = k_s \left[ 1 - \int_{-\infty}^t dt' R_s(t-t') c(t') \right], \quad (5.2)$$

where  $k_s = \tau_s^{-1}$  is the steady-state value and  $c(t)$  may be considered as a linear approximation of the ligand binding free-energy  $f_c(t) = \ln \left( \frac{1+c(t)/K_I}{1+c(t)/K_A} \right)$  recently proposed by Tu et al. [86]. Here,  $K_I$  and  $K_A$  are respectively the dissociation constants of the inactive and active forms of the chemoreceptors.  $K_A$  is usually several orders of magnitude greater than  $K_I$  and therefore can be neglected for a weak stimulus, which is the case in the present experiment. Using the above definition, a straightforward but tedious calculation yields the mean displacement  $\bar{x}_i$  during one swimming cycle ( $\tau_f + \tau_b$ ),

$$\bar{x}_i = \left\{ \tau_f^2 \int_0^\infty dt R_f(t) \exp\left(-\frac{t}{\tau_f}\right) + \tau_b^2 \int_0^\infty dt R_b(t) \left[ \exp\left(-\frac{t}{\tau_b}\right) - f(t) \right] \right\} \langle v_i^2 \rangle \nabla c \quad (5.3)$$

where the subscript  $i$  stands for the vector component along the chemical gradient direction, the brackets  $\langle \dots \rangle$  represent the angular average for the swimming  $\vec{v}$  velocity, and

$$f(t) = \frac{\tau_f^2}{\tau_f - \tau_b} \left( \frac{1}{\tau_b} \exp\left(-\frac{t}{\tau_b}\right) - \frac{1}{\tau_f} \exp\left(-\frac{t}{\tau_f}\right) \right). \quad (5.4)$$

By requiring that the response functions  $R_s(t)$  are well behaved in long times, which can be implemented by demanding the integral of  $R_s^2(t)$  to have a finite variance given by  $\sigma_s^2 = \tau_s \int_0^\infty R_s(t)^2 dt$  [27], we show that for scenario (i), the optimal drift velocity  $V$  ( $\equiv \bar{x}_i / (\tau_f + \tau_b)$ ) is obtained if  $R_f(t)$  is monophasic and  $R_b(t)$  is biphasic with the result [6],

$$R_f(t) \propto \frac{\sigma_f}{\tau_f} \exp\left(-\frac{t}{\tau_f}\right), \quad (5.5)$$

$$R_b(t) \propto \frac{\sigma_b}{\tau_b} \left[ \exp\left(-\frac{t}{\tau_b}\right) - \frac{\tau_f^2}{\tau_f - \tau_b} \left( \frac{1}{\tau_b} \exp\left(-\frac{t}{\tau_b}\right) - \frac{1}{\tau_f} \exp\left(-\frac{t}{\tau_f}\right) \right) \right]. \quad (5.6)$$

We note that depending on the ratio of the two swimming intervals  $\beta (= \tau_b/\tau_f)$ ,  $R_b(t)$  exhibits two different behaviors. For  $1 \leq \beta < 2$ ,  $R_b(t)$  consists of a positive lobe in short times and a negative lobe in long times, which is a characteristic of chemotaxis response with a negative feedback. Outside the above specified  $\beta$  range,  $R_b(t)$  is always negative for  $\beta < 1$  and positive for  $\beta \geq 2$  [6]. Some representative response functions are plotted in Figure 5.1(A).

For scenario (ii), the response function  $R(t)$  is given by,

$$R(t) = \frac{\sigma_b}{\tau_f + \tau_b} \left\{ \exp\left(-\frac{t}{\tau_f}\right) + \gamma \frac{\tau_b^2}{\tau_f^2} \left[ \exp\left(-\frac{t}{\tau_b}\right) - \frac{\tau_f^2}{\tau_f - \tau_b} \left( \frac{1}{\tau_b} \exp\left(-\frac{t}{\tau_f}\right) - \frac{1}{\tau_f} \exp\left(-\frac{t}{\tau_b}\right) \right) \right] \right\}. \quad (5.7)$$

This function is biphasic for all values of  $\beta$  and  $\gamma$ . However, depending on their values,  $R(t)$  can be positive ( $R(t) > 0$ ), negative ( $R(t) < 0$ ), or exhibit a double-lobe (positive in short times and negative in long times) feature. The latter is characteristic of chemotaxis enabled by adaptation. Typical response functions in different parameter regimes are displayed in Figure 5.1(B), and the diverse behaviors of  $R(t)$  are summarized by the phase plot in the inset of Figure 5.1(B). We noticed that for *V. alginolyticus* the steady-state response with  $\beta \approx 1$  falls inside regime II, which has the double-lobe feature.

Using the optimized response functions, the drift velocities are calculated  $V = \bar{x}_i/(\tau_f + \tau_b)$ . For independent sensing, we find

$$V_i = \frac{\langle v_i^2 \rangle \nabla c}{\tau_f + \tau_b} \left\{ \tau_f^2 \int_0^\infty dt R_f(t) \exp\left(-\frac{t}{\tau_f}\right) + \tau_b^2 \int_0^\infty dt R_b(t) \left[ \exp\left(-\frac{t}{\tau_b}\right) - f(t) \right] \right\}, \quad (5.8)$$

where  $R_f(t)$ ,  $R_b(t)$ , and  $f(t)$  are given by Eqs. 5.4-5.6. For shared sensing, we find

$$V_s = \frac{\langle v_i^2 \rangle \nabla c}{\tau_f + \tau_b} \left\{ \int_0^\infty dt R(t) \left[ \tau_f^2 \exp\left(-\frac{t}{\tau_f}\right) + \gamma \tau_b^2 \left( \exp\left(-\frac{t}{\tau_b}\right) - f(t) \right) \right] \right\}, \quad (5.9)$$

where  $R(t)$  is given by Eq. 5.7. Figure 5.2 displays the ratio of the drift velocities  $V_i/V_s$  as a function of the time ratio  $\beta = \tau_f/\tau_b$  and the amplitude ratio  $\gamma$ , i.e.,  $\gamma \equiv R_b(t)/R_f(t)$  for shared and  $\gamma \equiv \sigma_b/\sigma_f$  for independent sensing. It is evident from this graph that the

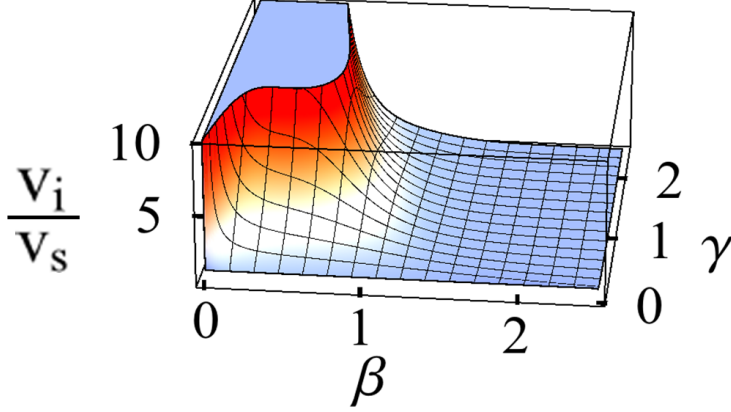


Figure 5.2: Drift velocity ratio for independent and shared chemosensing. The drifting velocities,  $V_i$  and  $V_s$ , are calculated using the optimized response functions for independent and shared chemosensing, and their ratio  $V_i/V_s$  is plotted. For both cases we define  $\beta \equiv \tau_b/\tau_f$  and  $\gamma$  to be the amplitude ratio. We noted that for the biologically relevant range,  $\gamma \simeq 1$  and  $\beta \lesssim 1$ ,  $V_i/V_s > 1$ , indicating that independent chemosensing is more efficient for migration in a linear chemical gradient. Note that the base of the white region in the plot corresponds to the plane where  $V_i/V_s = 1$ .

migration speed is higher for independent sensing than for shared sensing for the biologically relevant range of parameters,  $\gamma \simeq 1$  and  $\beta \simeq 1$ .

To determine the response functions experimentally, we measured both the mean switching rate  $S(t)$  and the CCW bias  $\Phi(t)$  after a brief stimulation administered at  $t = 0$  (see Figure 5.5). For a two-state motor,  $S(t)$  and  $\Phi(t)$  uniquely specifies the statistical properties of the motor switch. In particular, when the stimulation is weak, Eq. 5.2 yields

$$S(t) \equiv \frac{2}{\tau_f(t) + \tau_b(t)} \approx S_0 \left[ 1 - \Phi_0 \int_{-\infty}^t R_f(t-t')c(t')dt' - (1 - \Phi_0) \int_{-\infty}^t R_b(t-t')c(t')dt' \right], \quad (5.10)$$

$$\Phi(t) \equiv \frac{\tau_f(t)}{\tau_f(t) + \tau_b(t)} \approx \Phi_0 \left[ 1 + (1 - \Phi_0) \int_{-\infty}^t (R_f(t-t') - R_b(t-t'))c(t')dt' \right], \quad (5.11)$$

where  $S_0 = 2/(\tau_f + \tau_b)$  and  $\Phi_0 = \tau_f/(\tau_f + \tau_b)$  are the steady-state switching rate and the bias. These relationships are informative in that  $\Delta S(t) (\equiv S(t) - S_0)$  is proportional to the  $\Phi_0$ -weighted sum of  $R_f(t)$  and  $R_b(t)$  whereas  $\Delta\Phi(t) (\equiv \Phi(t) - \Phi_0)$  is proportional to their difference. It follows that if chemosensing is shared with  $\gamma \simeq 1$ , the bias  $\Phi(t)$  should be weakly dependent on time and Eq. 5.10 allows the response function  $R(t)$  to be determined. If chemosensing is independent,  $R_f(t)$  and  $R_b(t)$  can be determined by solving Eqs. 5.10 and 5.11. For continuous stimulation  $-\infty < t' < t$ , the convolution integrals  $\tilde{R}_s(t) \equiv \int_{-\infty}^t R_s(t-t')c(t')dt'$ , where  $s = (f, b)$ , are given by,

$$\tilde{R}_f(t) = \frac{\Phi(t) - \Phi_0}{\Phi_0} + \frac{S_0 - S(t)}{S_0}, \quad (5.12)$$

$$\tilde{R}_b(t) = \frac{\Phi_0 - \Phi(t)}{1 - \Phi_0} + \frac{S_0 - S(t)}{S_0}. \quad (5.13)$$

The response functions  $R_f(t)$  and  $R_b(t)$  can be extracted by a Fourier transformation method.

## 5.3 RESULTS

### 5.3.1 Unconditioned switching rate measurements

Although the measured quantity in our experiment (see Chapter 2 and Appendix A.2) is the switching rate  $S(t)$ , its functional form is remarkably similar to the CW bias seen in *E. coli* [18]. In both cases, the responses are biphasic, i.e., as a result of a positive stimulus, *E. coli* suppress their CW bias as the run interval is lengthened but *V. alginolyticus* suppress their switching rate. Once the stimulus is withdrawn, *E. coli* cells increase their CW bias but *V. alginolyticus* increase their switching rate. Biologically these responses make sense for each bacterium and can be interpreted as its attempt to stay closer (for *E. coli*) or return (for *V. alginolyticus*) to a “greener pasture”. However, because of the finite memory time both bacteria eventually restore their steady-state behavior.

Hence, our measured  $S(t)$  in *V. alginolyticus* displays all canonical features of bacterial chemotaxis enabled by adaptation. Since in this experiment the stimulation is random, occurring either during CCW or CW intervals for the bacteria in the population, the switching rate  $S(t)$  is an average of the responses in both swimming intervals. Below, we attempt to analyze the implication of our measured  $S(t)$  on how *V. alginolyticus* regulate their swimming intervals. For instance, can  $S(t)$  say anything about whether the chemosensing/response in *V. alginolyticus* is shared or independent?

If *V. alginolyticus* employ the independent chemosensing scheme, Eq. 5.2 yields the mean switching rate  $S(t)$  given by,

$$S(t) = S_0 \left[ 1 - \int_{-\infty}^t \bar{R}(t-t')c(t')dt' \right], \quad (5.14)$$

where  $\bar{R}_0(t) = \Phi_0 R_f(t) + (1 - \Phi_0) R_b(t)$ . Using the calculated response functions in Eqs. 5.5 and 5.6 and the fact that for *V. alginolyticus*  $\Phi_0 \simeq 0.5$  (see Section 5.3.2), we found  $\bar{R}(t) \simeq (R_f(t) + R_b(t))/2$  or,

$$\bar{R}(t) \propto \frac{\sigma_f}{\tau_f + \tau_b} \left[ \left( 1 - \gamma' \frac{\tau_f^2}{\tau_b(\tau_f - \tau_b)} \right) \exp\left(-\frac{t}{\tau_f}\right) + \gamma' \left( 1 + \frac{\tau_f}{\tau_f - \tau_b} \right) \exp\left(-\frac{t}{\tau_b}\right) \right]. \quad (5.15)$$

This function contains four parameters, the overall amplitude  $R_0 \sim \sigma_f/(\tau_f + \tau_b)$ , the amplitude ratio  $\gamma' \equiv \sigma_b/\sigma_f$ , and the two mean dwell times  $\tau_f$  and  $\tau_b$ . We noticed that in the limits that  $\tau_f \simeq \tau_b$  and  $\gamma' \simeq 1$ , which will be justified below (Section 5.3.3),  $\bar{R}(t)$  attains the following simple form,

$$\bar{R}(t) = R_0 \left[ 1 - \frac{t}{\tau} - \left( 1 + \frac{t}{\tau} \right) \frac{\Delta}{\tau} \right] \exp\left(-\frac{t}{\tau}\right) \quad (5.16)$$

where  $\tau_b = \tau$ ,  $\tau_f = \tau + \Delta$ , and  $\Delta$  is a small parameter.

On the other hand, if *V. alginolyticus* employ the shared chemosensing scheme,  $S(t)$  is given by,

$$S(t) = S_0 \left[ 1 - (\Phi_0 + \gamma(1 - \Phi_0)) \int_{-\infty}^t R(t-t')c(t')dt' \right], \quad (5.17)$$

where  $R(t)$  is given by Eq. 5.7. Again, if we take the limit  $\gamma \rightarrow 1$  and assume  $\tau_f - \tau_b = \Delta$  is small, we found  $S(t) = S_0 \left[ 1 - \int_{-\infty}^t R(t-t')c(t')dt' \right]$ , which has the same functional form as Eq. 5.14, but the response function is given by,

$$R(t) = R_0 \left[ 1 - \frac{t}{\tau} - \left( \frac{t}{\tau} - 4 \right) \frac{\Delta}{\tau} \right] \exp \left( -\frac{t}{\tau} \right). \quad (5.18)$$

It follows from Eqs. 5.16 and 5.18 that when  $\Delta/\tau \ll 1$ , the average response function  $\bar{R}(t)$  for independent sensing and the response function  $R(t)$  for shared sensing have essentially the same mathematical form,

$$\bar{R}(t) \simeq R(t) \simeq R_0 \left( 1 - \frac{t}{\tau} \right) \exp \left( -\frac{t}{\tau} \right). \quad (5.19)$$

Interestingly, Eq. 5.19 is identical to the solution of the response function of a critically damped harmonic oscillator, which is commonly used in engineering designs that provide fast response, high fidelity, and robust system controls [7].

Assuming a  $\delta$ -in-time stimulation  $c(t) = c'\delta(t)$ , the switching rate for both scenarios (i) and (ii) is simply given by  $S(t) = S_0 [1 - c'\bar{R}(t)]$ , which is identical to Eq. 2.15 used to fit our data in Section 2.2.4.2.

### 5.3.2 Conditional statistics and motor rotational bias

It is evident from the above analyses that our measured  $S(t)$  is not sufficient to answer the question whether *V. alginolyticus* adopt shared or independent chemosensing. It appears that such a question cannot be addressed without a pure ensemble in which cells' rotation states are well defined at the time of stimulation. To conduct such a conditional statistical analysis we look more carefully at the time traces of individual bacteria in the optical trap. Such inspection reveals subtle but discernible differences in the transitions from one rotation state to another as can be seen in Figure 5.3(C). Specifically, we noticed that there is a slight asymmetry in the transition rates between the two states. For the case displayed in Figure 5.3(C), the transition from the lower ( $-x_0$ ) to the upper ( $+x_0$ ) state is faster than the transition from the upper to the lower state (see Appendix A.2 for the definitions of the  $\pm x_0$  states), and they appear to be systematic. We reasoned that since the transition

from backward to forward swimming is intervened by a flick, the slower transition should correspond to the switch to forward swimming. We also noticed that the stability of the two states in the optical trap are not the same. For the example given in Figure 5.3(C), the level of the lower state is more stable than the level of the upper state. The slow decline of the upper states suggests that the cell body is more likely to drift towards the trapping center during these swimming intervals than the lower state. Among a few thousand trapped bacteria, we found that a significant fraction of them behave in this fashion. For almost all of the cells that exhibit such behavior, the slanted state precedes the slower motor reversal event, and according to our reasoning, it is designated as the CW or the backward swimming direction. However, the features described above in the time series are not always apparent; for certain cells the difference between the transition rates or the inclination is too small to be practical for differentiating the two rotational states. Using the above criteria, we were able to assign, with confidence, the directions of motor rotations to approximately 50% of the trapped cells.

Fortuitously we found another interesting feature in the time series that can help us identify the sense of flagellar motor rotations. By power spectrum analysis of individual swimming intervals in the time series (see Figure 5.3(C), and Appendix A.2), we found that there is a consistent pattern in the rotation frequencies of the cell body  $\Omega(t)$  and the flagellum  $\omega(t)$ , which are displayed in Figure 5.3(D). Specifically, it was observed that both  $\omega(t)$  and  $\Omega(t)$  fluctuate in synchrony with the two motor states and  $\omega(t)$  and  $\Omega(t)$  are out of phase with each other; i.e., if one of the states has a higher flagellar frequency  $\omega$ , the corresponding cell-body frequency  $\Omega$  will be lower than the other state. However, upon transition to the next state, the flagellum frequency will decrease but the cell-body frequency will increase. This pattern repeats from one swimming cycle to the next as delineated in Figure 5.3(D). Hence our observation shows that the flagellum and the cell-body rotation frequencies in the two swimming states are anticorrelated. While the physical mechanism for this anticorrelation is unknown, it provides a convenient means to identify the motor rotation directions. Since *V. alginolyticus* swim faster in the backward direction, by  $\sim 15\%$  based on our unpublished result and by as much as  $\sim 50\%$  according to Ref. [85] and since the higher cell-body rotation speed gives a higher torque, we postulate that the state with a higher (lower) cell-

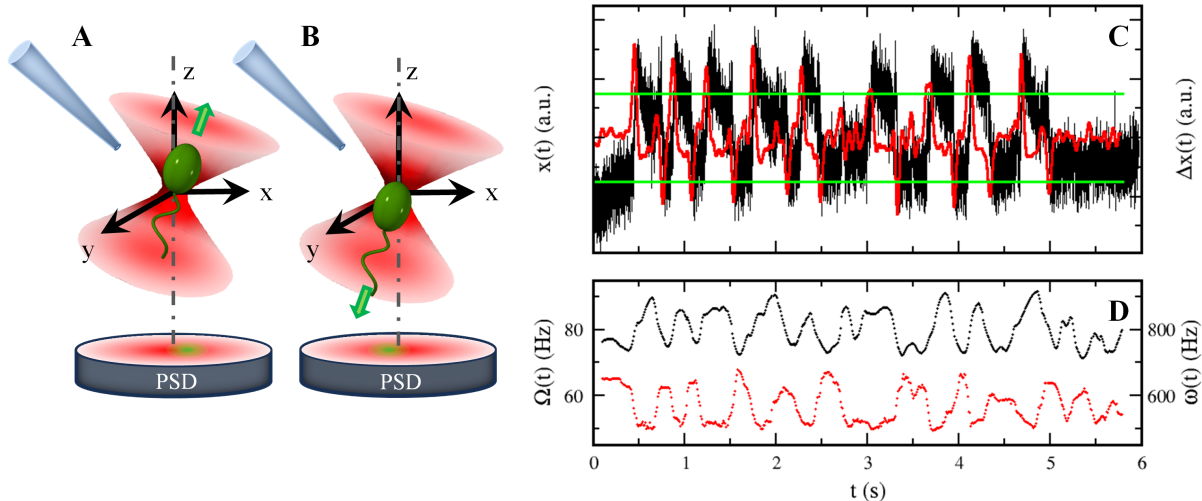


Figure 5.3: Experimental setup and signal processing. The center of the optical trap is initially placed at a distance  $\sim 3 \mu\text{m}$  away from the tip of a serine-filled micropipette. Once a bacterium falls in the trap, the computer initiates the movement of the optical tweezers forcing the bacterium to move out (along  $y$ ) of the high concentration region. A slight tilt ( $\sim 3^\circ$ ) of the optical trap allows the forward (A) and backward (B) swimming intervals to be recorded on the position sensitive detector (PSD). (C) The plot depicts the time trace  $x(t)$  of the bacterial cell-body position (black line) in the optical trap. The red line is a result of the convolution of the data  $x(t)$  with a differentiate filter (the derivative of a Gaussian with a width of 50 ms). The filtering procedure allows the individual motor reversals to be precisely located on the time trace. We observed that there exist two quasi stable states, and the transition from the lower to the upper state is generally faster than the upper to the lower state. Such an asymmetry is due to the flicks that occur only during the backward to forward transition. Thus, in this time trace, we assign the lower state as the CCW (forward) and the upper state the CW (backward) rotation. We also noticed that the stability of the upper and the lower states are not the same. The inclination of the upper state suggests that during this swimming interval the cell body gradually shifts towards the trapping center. Among a few thousands of trapped bacteria, we found that a significant fraction of them behaves this manner. In (D), the anticorrelation between the cell-body rotation frequency  $\Omega(t)$  (black curve) and the flagellum rotation frequency  $\omega(t)$  (red curve) is illustrated for the same time series in (C).

body (flagellum) rotation speed is the CW or backward swimming state. By a blind-fold test, we found that this assignment of the rotation states is in very good agreement with the first method based on the asymmetry in the state-to-state transition rates.

Since the correct assignment of the rotation state is very important in this experiment, we sought other means to justify our method. In our previous experiment, the steady-state dwell time distributions  $P(\Delta_f)$  and  $P(\Delta_b)$  were measured in free-swimming bacteria [92]. These distributions exhibit markedly different behaviors for large and small  $\Delta_s$  that can be used to verify our designation method, where  $s = (f, b)$ . In light of this, the motor rotation directions of  $n = 323$  unstimulated cells were identified using time series similar to Figure 5.3(C). Ignoring the first interval, since it is typically a partial interval, we constructed the dwell time distributions  $P(\Delta_f)$  and  $P(\Delta_b)$  as displayed in Figure 5.4. We found that for the forward intervals  $P(\Delta_f)$  (black circles) is peaked at a shorter time than its backward counterpart  $P(\Delta_b)$  (red circles). Moreover, when plotted in semi-logarithmic scales as the ones delineated in the inset, we found that the forward intervals has a much broader tail than for the backward intervals. These features are in good agreement with our early observations [92]. Quantitatively we found that the peak positions for the forward and the backward intervals are given respectively by  $\Delta_{fmax} \approx 0.15\text{s}$  and  $\Delta_{bmax} \approx 0.2\text{s}$ . The measured distribution functions also allow us to calculate the steady-state mean dwell times  $\tau_f = 0.33 \pm 0.01\text{s}$  and  $\tau_b = 0.31 \pm 0.01\text{s}$ . These results are again consistent with what were observed in free-swimming *V. alginolyticus* [92], and they lead to the steady-state forward bias  $\Phi_0 \simeq 0.52$ .

Combining these methods (asymmetrical transition rates and anticorrelation between  $\omega(t)$  and  $\Omega(t)$ ), we were able to assign the motor rotation states to  $\sim 80\%$  of the cells we trapped. This allows us to separate the bacteria into two groups with the one in which all cells swim forward and in the other all cells swim backward at the time of stimulation ( $t = 0$ ).

The first column in Figure 5.5 depicts the measurements of the conditional switching rates,  $S_F(t)$  and  $S_B(t)$ , for  $c_0 = 1, 5$  and  $10\mu\text{M}$ , corresponding to panels (A,E), (I,M) and (Q,U), respectively. Here the subscripts  $F$  and  $B$  stand for the ensembles in which the bacteria swim exclusively in the forward and the backward direction at  $t = 0$ , respectively.

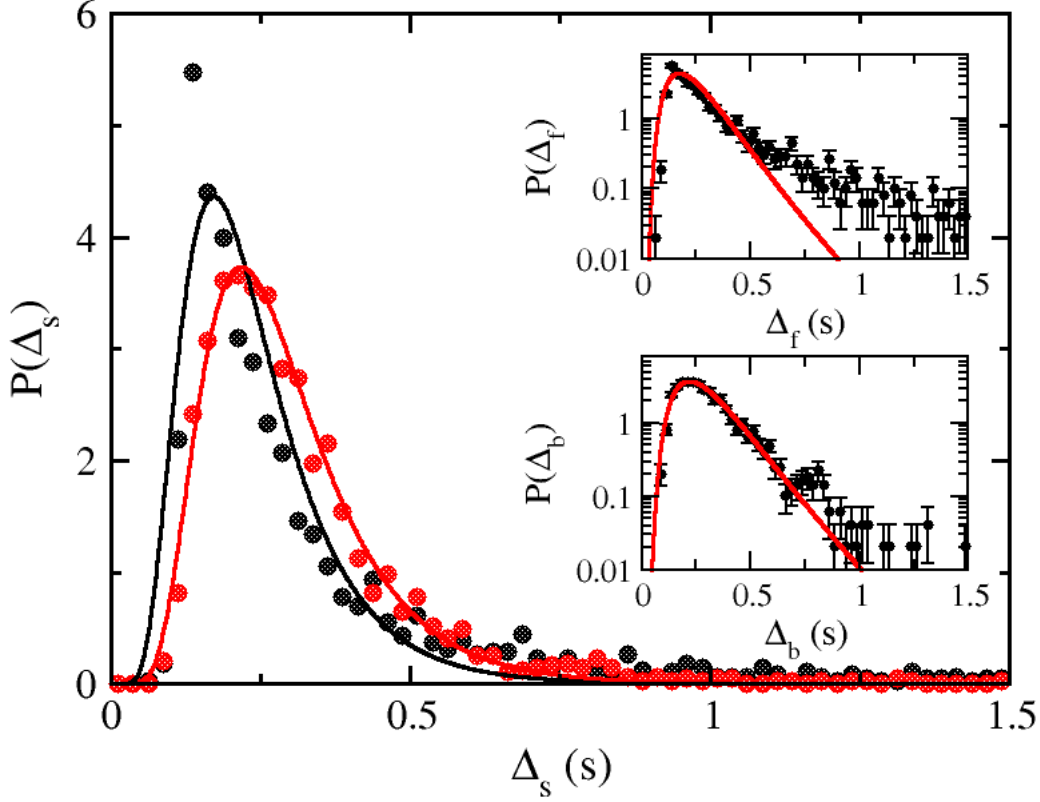


Figure 5.4: Forward and backward dwell time distributions. The main figure depicts the dwell time distributions  $P(\Delta_s)$  for forward  $s = f$  (black circles) and backward  $s = b$  (red circles). The black and red curves are fits to experimental data using the log-normal distribution,  $P(\Delta_s) = \frac{1}{\sqrt{2\pi\Delta_s^2\sigma^2}} \exp\left[-\frac{(\ln\Delta_s-\mu)^2}{2\sigma^2}\right]$ , where  $\mu$  and  $\sigma$  are the fitting parameters. Here,  $\mu \simeq -1.54$  and  $\sigma \simeq 0.48$  for the forward intervals, and  $\mu \simeq -1.33$  and  $\sigma \simeq 0.44$  for the backward intervals. The insets are the semi-log plots of the same distribution functions.

Overall, we found that  $S_F(t)$  and  $S_B(t)$  behave similarly for a given stimulation level  $c_0$ . This similarity explains why the measurement of the average switching rate alone is insufficient to tell whether one or two response functions are used by cells of *V. alginolyticus* for chemotaxis. One also observes in the first column of Figure 5.5 that as  $c_0$  increases, there is a significant change in the initial suppression of the switching rates, which is indicated by  $\Delta S$  in the panels. In particular, for  $c_0 = 10 \mu\text{M}$ , the switching is nearly completely suppressed with  $S = 0$ , indicating the onset of a nonlinear response in the chemotaxis network.

In the second column of Figure 5.5, the conditional CCW bias,  $\Phi_F(t)$  and  $\Phi_B(t)$ , are plotted in panels (B,F),(J,N),(R,V) as a function of time for  $c_0 = 1, 5, \text{ and } 10 \mu\text{M}$ , respectively. One observes that for the lowest concentration ( $c_0 = 1 \mu\text{M}$ ),  $\Phi_F$  and  $\Phi_B$  relax towards the steady-state  $\Phi_0 (\simeq 0.5)$  similarly with a decay time  $\sim 0.2 - 0.3 \text{ s}$  that is close to the steady-state switching rate  $S_0 \simeq 3.3 \pm 0.3 \text{ s}^{-1}$  (see the first column of Figure 5.5). As  $c_0$  increases to  $5 \mu\text{M}$ , while the relaxation time for  $\Phi_B$  remains unchanged, the time for  $\Phi_F$  is nearly doubled to  $\sim 0.58 \text{ s}$ . When the serine concentration is increased further to  $10 \mu\text{M}$ , we found that both  $\Phi_F(t)$  and  $\Phi_B(t)$  persist for a longer time after the stimulation, more so for  $\Phi_F(t)$  than for  $\Phi_B(t)$ . The typical time scales are  $\sim 0.58 \text{ s}$  and  $0.52 \text{ s}$  for the forward and backward swimmers, respectively. As a result, the functional forms of  $\Phi_F(t)$  and  $\Phi_B(t)$  become somewhat similar again as in the case of  $c_0 = 1 \mu\text{M}$ . The above observation shows that the chemical sensitivity to the serine in the forward and the backward direction are quite different. The observation also demonstrates that in *V. alginolyticus* both swimming intervals are extended upon exposure to chemoattractant. This behavior however is at variance with *E. coli* for which only the run interval is extended upon exposure to chemoattractant, leaving the tumbling interval untouched [13] or shortened [18, 28]. A striking feature of both sets of data (5 and 10  $\mu\text{M}$ ) is that while  $\Phi_B(t)$  relaxes toward  $\Phi_0$  monotonically,  $\Phi_F(t)$  dips below  $\Phi_0$  at  $t \simeq 1 \text{ s}$  before leveling off toward  $\Phi_0$  at a longer time. For all the measurements presented, Figures 5.5(B,F),(J,N),(R,V), we found that in general the forward response is stronger than the backward response.

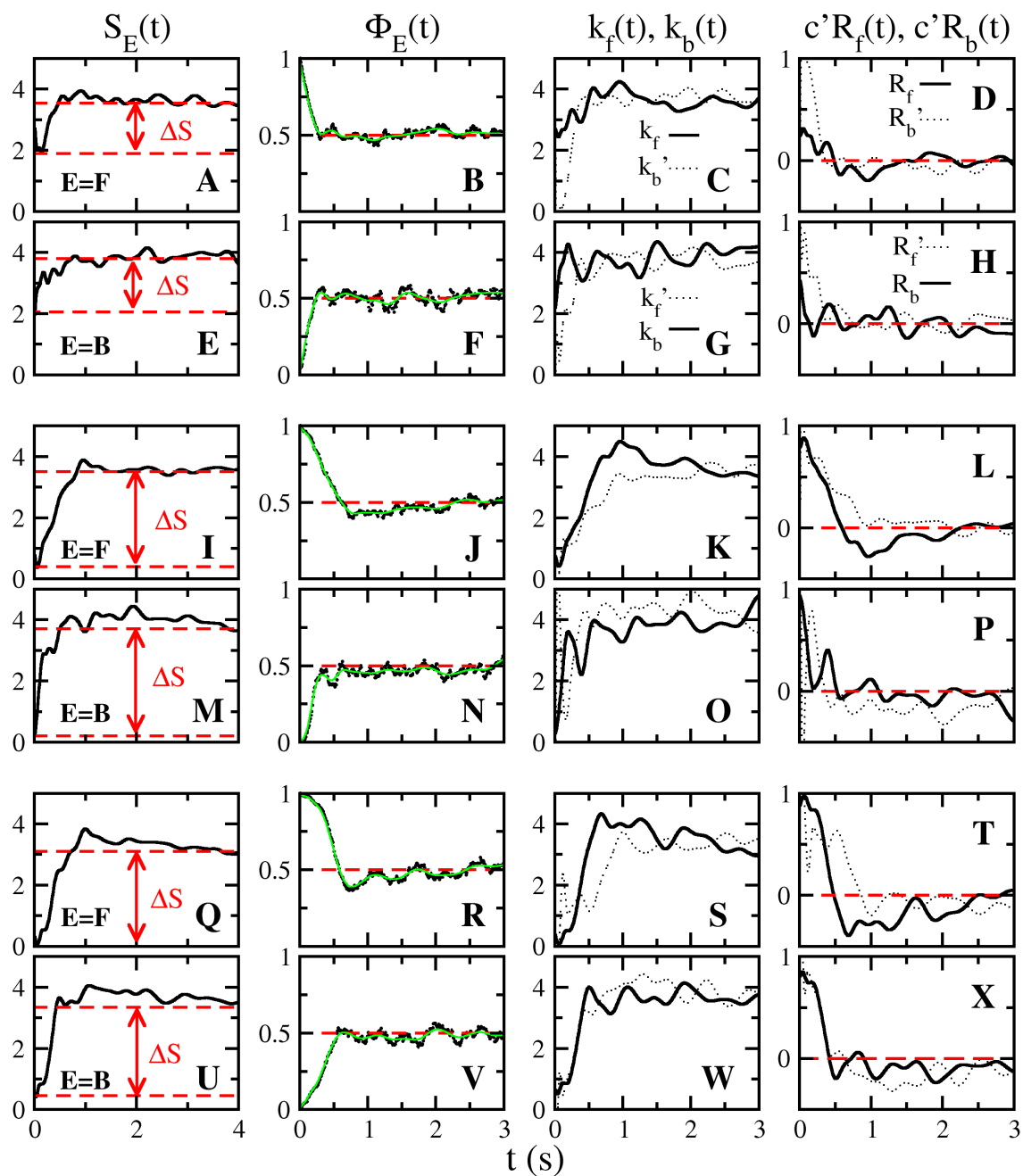


Figure 5.5: Pure ensemble measurements. The top eight panels (A-H), the middle eight panels (I-P), and the bottom eight panels (Q-X) correspond to measurements using serine concentrations  $c_0 = 1, 5,$  and  $10 \mu\text{M}$ , respectively. The first column is for the switching rates  $S_E(t)$ , where the subscript  $E=F$  or  $B$  stands for the pure ensemble when at  $t = 0$  all the cells are swimming forward or backward and is applicable to the corresponding row of panels. (continued on page 74)

(continuation of the caption of Figure 5.5) Here,  $\Delta S$  indicates the initial suppression of the switching rate relative to its steady-state value  $S_0$ . The second column is for the CCW bias  $\Phi_E(t)$  with the same subscript designation as before. Here, the green lines are smoothed data using the Bezier filter. Similar smoothing was also carried out for the switching rates as presented in the first column. The third column is for the switching rates,  $k_f(t)$  and  $k_b(t)$ , where the solid black lines are for the directly and dotted lines are for the indirectly stimulated cells. For example, for the pure CCW (CW) ensemble, E=F (E=B),  $k_f(t)$  ( $k_b(t)$ ) is the switching rate for the directly stimulated cells and  $k'_b(t)$  ( $k'_f(t)$ ) is the switching rate for the indirectly stimulated cells. The last column is for the response functions  $R_f(t)$  and  $R_b(t)$ , where again the solid lines are for the direct response and dotted lines are for the indirect response. The switching rates and the response functions are calculated using  $S_E(t)$  (first column) and  $\Phi_E(t)$  (second column) and Eqs. 4.1 and 4.2. See text for more details. Note that because of the number of switched cells shortly after the serine pulse is small, the indirect switching rates,  $k'_b(t)$  and  $k'_f(t)$ , is not very reliable as can be seen by the large fluctuations in the dotted lines in the third column. The same can also be said about  $R'_f(t)$  and  $R'_b(t)$ , which are presented by the dotted lines in the fourth column.

It is also instructive to evaluate the average bias  $\Phi_M(t)$  without sorting the cells according to their initial (CCW or CW) states. The data for this mixed ensemble is displayed in Figure 5.6 for  $c_0 = 1, 5,$  and  $10 \mu\text{M}$ . For all runs the graphs show that initially  $\Phi_M(t \rightarrow 0)$  stay high ( $\sim 60 - 65\%$ ) and then decay toward the steady-state value  $\Phi_0 \simeq 0.5$  over time. For the two high concentration runs ( $c_0 = 5,$  and  $10 \mu\text{M}$ ), the relaxation towards  $\Phi_0$  is not monotonic but appears to oscillate. Note in particular for small times,  $\Phi_M(t)$  increases momentarily before declining rapidly. This can only happen if the forward swimmers have a longer persistence time than the backward swimmers after the brief stimulation, indicating that these two sub-populations must have different response times. It is also peculiar that for this mixed ensemble, the initial forward bias is not at the steady-state level  $\Phi_0$ . The effect can be understood as a result of bacterial 3-step motility pattern, which is not completely symmetric for the forward and backward swimmers due to the flick. That is one of the reasons that a backward swimmer is captured because it misses the trap during the forward run. In other words, the forward swimming has the tendency to preempt the opportunity for a cell to be captured in the backward direction. This effect is purely geometrical and can be reproduced even when there is no chemoattractant present, namely when the micropipette is filled only with TMN buffer. This also explains why increasing stimulation strength only acts to increase the delay time in  $\Phi_M(t)$  but not the amplitude of the bias as seen in Figures 5.6(B,F,J). This observation is in sharp contrast with the switching rate  $S_M(t)$  displayed in Figures 5.6(A,E,I), where the suppression in the switching rate  $\Delta S$  in early time is a strong function of  $c_0$ . In particular, we found that for a brief exposure of  $c_0 = 10 \mu\text{M}$  serine, the switching rate is nearly completely suppressed  $S(t \rightarrow 0) \approx 0$  in short times. The observation is also at variant with what was found in *E. coli* for which the amplitude of the bias changes rapidly with the chemoattractant concentration [46]. This suggests that the chemotactic regulation mechanisms in *V. alginolyticus* and in *E. coli* are fundamentally different; in the former it is the switching rate but in the latter it is the motor bias that is actively regulated by the cells. The observation also raises interesting questions about why different microorganisms use different regulation mechanisms, and how these different regulations are performed by the networks.

The above observation allows us to make the following general remarks about the response

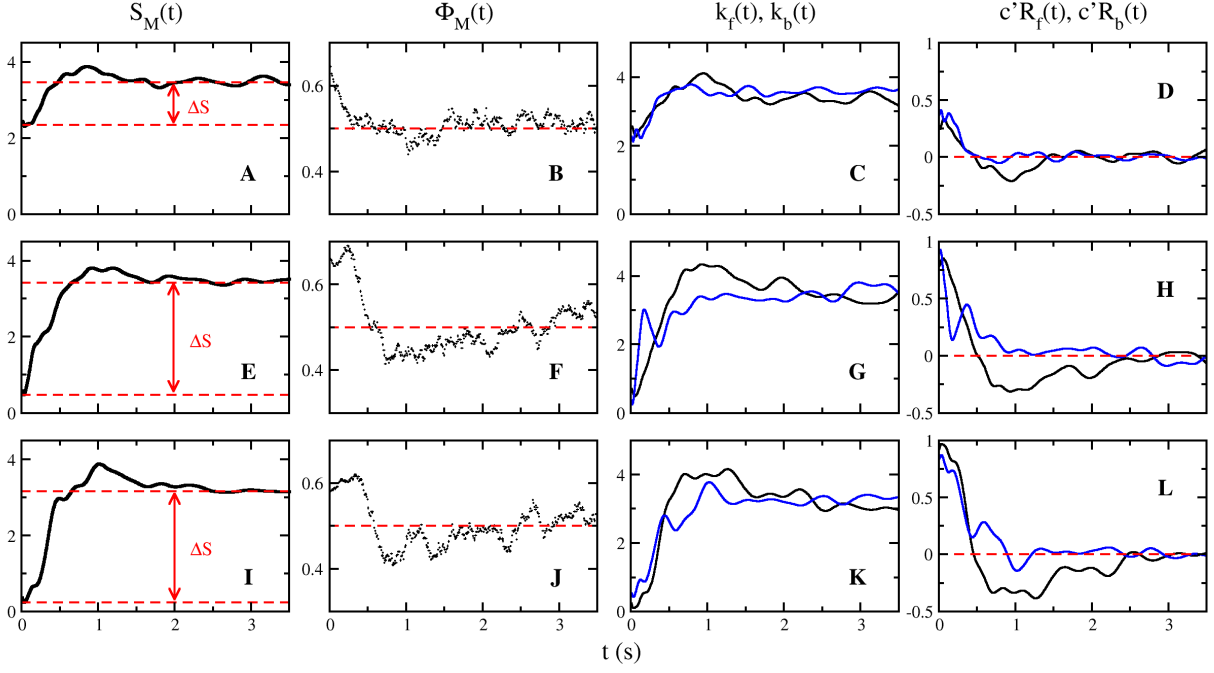


Figure 5.6: Mixed ensemble measurements. The measurements for different stimuli,  $c_0 = 1, 5, \text{ and } 10 \mu\text{M}$ , are presented in the top (A-D), the middle (E-H), and the bottom panels (I-L), respectively. The brief stimulus is administrated at  $t = 0$  for a mixed ensemble of cells. One observes that shortly after the stimulation, the switching rates  $S_M(t)$  of the population decrease markedly as  $c_0$  increases, which are displayed by the figures in the first column. Here  $\Delta S$  indicates the initial suppression of the switching rate relative to its steady-state value  $S_0$ . The second column is for the CCW bias  $\Phi_M$ . It should be noted that at  $t = 0$ , there is an excess of forward swimmers in the mixed population,  $\Phi_M(t \rightarrow 0) > \Phi_0 \simeq 0.5$ , which can be attributed to the trapping bias as discussed in the main text. The third column is for the forward  $k_f(t)$  (black lines) and backward  $k_b(t)$  (blue lines) switching rates calculated based on Eqs. 4.1 and 4.2. The last column is for the forward  $R_f(t)$  (black lines) and the backward  $R_b(t)$  (blue lines) response functions.

functions in *V. alginolyticus*: (i) Since  $\Phi(t)$  increases momentarily shortly after the stimulus, it strongly suggests that chemosensing/control in *V. alginolyticus* is not shared, requiring two response functions to control the two swimming intervals. (ii) Since both forward and backward swimming intervals are extended, the amplitudes of the response functions,  $R_f(t \rightarrow 0^+)$  and  $R_b(t \rightarrow 0^+)$  must be positive. (iii) Since the response in the forward direction is stronger than in the backward direction and because  $\tau_f \simeq \tau_b$  [92], Eq. 5.2 suggests that the positive lobe of  $R_f(t)$  must be greater than that of  $R_b(t)$ . Below, we attempt to use the experimentally obtained conditional statistics on  $S_E(t)$  and  $\Phi_E(t)$  to derive the mathematical forms of  $R_f(t)$  and  $R_b(t)$  so that the above features can be made quantitative.

### 5.3.3 *V. alginolyticus* employ independent chemosensing

Based on their initial state of rotations, we reanalyze the switching rate data. For the initially CCW ensemble, the rate is designated as  $S_F(t)$  and for the initially CW ensemble, the rate is designated as  $S_B(t)$ . The data is shown in the first column of Figure 5.5 for different serine concentrations. One observes that these conditioned switching rates are qualitatively similar to those of the mixed ensembles (see Figure 2.8), both showing a significant suppression of the switching rate in early times and a relaxation to  $S_0$  in long times. Moreover, the suppression of  $S(t)$ , denoted as  $\Delta S$ , is a sensitive function of  $c_0$ .

Eqs. 5.10 and 5.11 allow us to extract  $R_f(t)$  and  $R_b(t)$  from the measured switching rate  $S(t)$  and bias  $\Phi(t)$  for chemical stimulations  $c(t)$  that are continuous in time. However, for a brief stimulation administered at  $t = 0$ ,  $c(t) = c'\delta(t)$ , these equations need to be modified in order to extract the response functions. Imagine that we have a pure ensemble of cells and all of them swim forward (or in the CCW state) at the time of stimulation,  $t = 0$ . If we look at these cells at a later time  $t$ , some will still be in the forward state but the other will switch to the backward state. The cells which remain in the forward state will have a transition rate  $k_f(t)$  that depends on time. However, for those cells who have switched, they will have a different transition rate  $k'_b(t)$ . Here the prime indicates that the transition rate in this backward interval is influenced by the stimulation that occurred in the previous (forward) interval. Hence,  $k'_b(t)$  characterizes what one may call the “indirect” stimulation effect or

the cross-talk between intervals. By the same token, we can also prepare an initially pure ensemble with all cells swimming backward (or in the CW state) at the time of stimulation,  $t = 0$ . In this case the direct transition rate is  $k_b(t)$  and the indirect transition rate is  $k'_f(t)$ . Below, we derive general expressions that allow these transition rates and their corresponding response functions to be extracted.

For a bacterial population that consists of  $n_f(t)$  forward swimming cells and  $n_b(t)$  backward swimming cells, the time evolution equation is given by,

$$\frac{dn_f(t)}{dt} = -k_f(t)n_f(t) + k_b(t)n_b(t), \quad (5.20)$$

$$\frac{dn_b(t)}{dt} = k_f(t)n_f(t) - k_b(t)n_b(t), \quad (5.21)$$

where  $n = n_f(t) + n_b(t)$  is a constant. It follows from the above expressions, the population based switching rate  $S(t)$  and the forward bias  $\Phi(t) \equiv n_f(t)/n$  are defined as,

$$S(t) = k_f(t)\Phi(t) + k_b(t)(1 - \Phi(t)), \quad (5.22)$$

$$\frac{d\Phi(t)}{dt} = -k_f(t)\Phi(t) + k_b(t)(1 - \Phi(t)). \quad (5.23)$$

Since  $S(t)$  and  $\Phi(t)$  are experimentally measured, the above equations allows us to determine the transition rates in both swimming intervals,

$$k_f(t) = \frac{1}{2\Phi(t)} \left( S(t) - \frac{d\Phi(t)}{dt} \right), \quad (5.24)$$

$$k_b(t) = \frac{1}{2(1 - \Phi(t))} \left( S(t) + \frac{d\Phi(t)}{dt} \right). \quad (5.25)$$

Note, the switching rate obtained in this way is model independent. If moreover the system is linear, these transition rates can be expressed in terms of the response functions given by Eq. 5.2.

For the pure CCW ensemble, we have  $\Phi_F(0) = 1$ ,  $S_F(0) = k_f(0)$ , and  $\frac{d\Phi_F(0)}{dt} = -k_f(0)$ . Eqs. 5.2, 5.24, and 5.25 allow the switching rate  $k_f(t)$  and the response function  $R_f(t)$  of the directly stimulated subpopulation, and the switching rate  $k'_b(t)$  and the response function

$R'_b(t)$  of the indirectly stimulated subpopulation to be calculated. Likewise, for the pure CW ensemble, we have  $\Phi_B(0) = 0$ ,  $S_B(0) = k_b(0)$ , and  $\frac{d\Phi_B(0)}{dt} = k_b(0)$ . The same set of equations allow the switching rate  $k_b(t)$  and the response function  $R_b(t)$  of the directly stimulated subpopulation, and the switching rate  $k'_f(t)$  and the response function  $R'_f(t)$  of the indirectly stimulated subpopulation to be calculated. For the pure CCW ensemble,  $k_b(t)$  defined by Eq. 5.25 gives the indirect switching rate  $k'_b(t)$ . On the other hand, for the pure CW ensemble,  $k_f(t)$  defined by Eq. 5.24 gives the indirect switching rate  $k'_f(t)$ . The results of these data analyses are given in the third and fourth columns in Figure 5.5. Here, the solid black lines are for the direct (or unprimed) quantities and the dotted lines are for the indirect (or primed) quantities.

One observes that for the low concentration of serine (see Figures 5.5(C and G)),  $c_0 = 1 \mu\text{M}$ , the group of forward swimmers responds to the serine stimulus weakly, which can be seen by the small depression in  $k_f(t)$  shortly after stimulation ( $t = 0$ ) as displayed by the solid black line in (C). On the other hand, the same stimulus produces a more acute response in the backward swimmers in that it produces a greater depression in the switching rate  $k_b(t)$  initially but,  $k_b(t)$  recovers very rapidly in less than 0.1 s as depicted by the solid black line in (G). As the concentration increases (see Figures 5.5(K and O)),  $c_0 = 5 \mu\text{M}$ , we found that both  $k_f(t)$  and  $k_b(t)$  change significantly as indicated by a large depression in both quantities near  $t = 0$ . Interestingly, however, the manner that  $k_f(t)$  and  $k_b(t)$  approach the steady state is quite different; the former is relatively slow characterized by a broad maximum at  $t \simeq 1 \text{ s}$  whereas the latter is very fast, similar to the weak-stimulation case, and appears to oscillate on its way to recovery. As the serine concentration increases further (see solid black lines Figures 5.5(S and W)),  $c_0 = 10 \mu\text{M}$ , the initial switching rates for both groups of bacteria decrease more. However, most significantly we noticed that the recovery time for the backward swimmers now become long and is almost comparable to their forward counterparts.

Now lets turn our attention to the response functions. For a weak impulsive stimulus  $c(t) = c'\delta(t)$ , Eq. 5.2 yield  $k_f(t) = k_f(1 - c'R_f(t))$  and  $k'_b(t) = k_b(1 - c'R'_b(t))$  for the CCW ensemble and  $k_b(t) = k_b(1 - c'R_f(t))$  and  $k'_f(t) = k_f(1 - c'R'_f(t))$  for the CW ensemble. Given the measured transition rates, the corresponding response functions thus can

be calculated in this limit and the results are presented in the last column of Figure 5.5. Here, we plotted  $c'R_f(t)$ ,  $c'R'_b(t)$ ,  $c'R_b(t)$ , and  $c'R'_f(t)$  as a function of time for  $c_0 = 1 \mu\text{M}$  (D,H),  $5 \mu\text{M}$  (L,P), and  $10 \mu\text{M}$  (T,X). We noticed that while the indirect response functions have an amplitude  $c'R'_s(t \rightarrow 0) \equiv c'R'_{s_0}$  of unity independent of  $c_0$ , which is required for  $k'_s(t \rightarrow 0) \rightarrow 0$ , the corresponding quantity for the direct response functions increases with  $c_0$ . An important feature of the response functions in Figure 5.5 is that the direct response of forward swimmers is biphasic, consisting of a short-time positive lobe and a long-time negative lobe. The direct response for the backward swimmers, on the other hand, appears to be more consistent with a monophasic, positive response in short times, albeit based on our data we cannot rule out the possibility that this backward response function is oscillatory or even biphasic when  $c_0$  becomes large enough. These remarkable features of the response functions also appear in the indirect response functions as delineated by the dotted lines in plots presented in the fourth column, i.e.,  $k'_f(t)$  is biphasic but  $k'_b(t)$  is monophasic. We note that the direct response functions obtained for the pure ensembles are nearly identical to those determined using the mixed ensemble (see Figure 5.6), indicating that our approach is self consistent.

How does the brief stimuli administered at  $t = 0$  affect cells' subsequent switching behaviors, i.e., after they leave the current swimming state? This is characterized by  $k'_b(t)$  for the CCW ensemble and  $k'_f(t)$  for the CW ensemble, which are plotted as the dotted lines in (C, K and S) and (G, O and W), respectively. These indirect effects signify the inheritance of information from one swimming interval to the next and can be important for bacterial chemotaxis. Since transmission of information is via molecules inside the cell, the memory time and fidelity are two important characteristics. We noticed that when the stimulation is weak ( $c_0 = 1 \mu\text{M}$ ), the indirect effect appears to be stronger than the direct effect in the sense that changes in  $k'_f(t)$  and  $k'_b(t)$  are bigger and last longer. However, this seemingly paradoxical effect is actually expected because as delineated earlier, *V. alginolyticus* have a refractory period upon switching to a new state (see Figure 5.4). Hence, shortly after a cell is switched, its switching rate is depressed, which is consistent with the dotted lines in (C) and (G). Interestingly, as  $c_0$  increases we found that inheritance of memory from forward to backward intervals is different from backward to forward intervals. Our data shows that the

backward intervals are more strongly influenced by the stimulation in the forward direction as indicated by a greater change in  $k'_b(t)$  than  $k'_f(t)$  as  $c_0$  increases. Biologically, this seems to make sense because information passed from the backward interval to the forward interval has little or no value to the cell since after the flick, it will swim in a new random direction. However, the situation is considerably different for the information passed from the forward to the backward swimming interval. In this case, since the backward trajectory is strongly correlated with the forward trajectory, the information can be used by the bacterium to perform chemotaxis more efficiently.

Figure 5.7 displays  $c'R_{f0}$  and  $c'R_{b0}$  as a function of  $c_0$ . We found that within the measurement uncertainties,  $R_{f0} \simeq R_{b0}$  for a given  $c_0$ , and hence the condition  $\gamma = R_{b0}/R_{f0} \simeq 1$  used in our calculations in Section 5.2 is reasonable. Figure 5.7 shows that  $c'R_{f0}$  and  $c'R_{b0}$  are strongly nonlinear in  $c_0$  but is consistent with the logarithmic dependence,  $c' = t_0 \ln(1 + c_0/K_{Is})$ , suggested by the Monod-Wyman-Changeux (MWC) model of Tu et al. [86]. We fit the experimental data by adjusting the parameters  $K_{Is}$  and  $R_{s0}t_0$ , where the bacterial exposure time to serine  $t_0 = 0.37$ s may be taken as given [4] and  $s = f, b$ . This fitting procedure yields the following results: In the forward direction,  $K_{If} = 0.71 \pm 0.07 \mu\text{M}$  and  $R_{f0}t_0 = 0.36 \pm 0.06$  and in the backward direction,  $K_{Ib} = 0.17 \pm 0.07 \mu\text{M}$  and  $R_{b0}t_0 = 0.23 \pm 0.06$ . Thus, for *V. alginolyticus* the forward swimming interval is characterized by a somewhat larger response amplitude but a lower serine sensitivity. As can be seen by the red and green lines in Figure 5.7, the quality of the fits is reasonably good. However, because of the limited data and the possibility that at  $c_0 = 10 \mu\text{M}$ , the response might be already nonlinear, the uncertainties in  $K_{If}$  and  $K_{Ib}$  are large. The above fitted values should be viewed as estimates of the dissociation constants of serine binding to receptors of *V. alginolyticus*.

A significant finding of these measurements is that  $R_f(t)$  and  $R_b(t)$  have different functional forms, supporting the notion that *V. alginolyticus* use different responses to explore oceanic environments. Specifically, we found that forward response function  $R_f(t)$  is biphasic consisting of a positive lobe in short times and a negative lobe in long times. The positive lobe is overwhelmingly greater than the negative one, suggesting that during the forward swimming interval, the chemotaxis network is capable of signal comparison and amplification. On the other hand, the backward response function  $R_b(t)$  is monophasic, consisting of

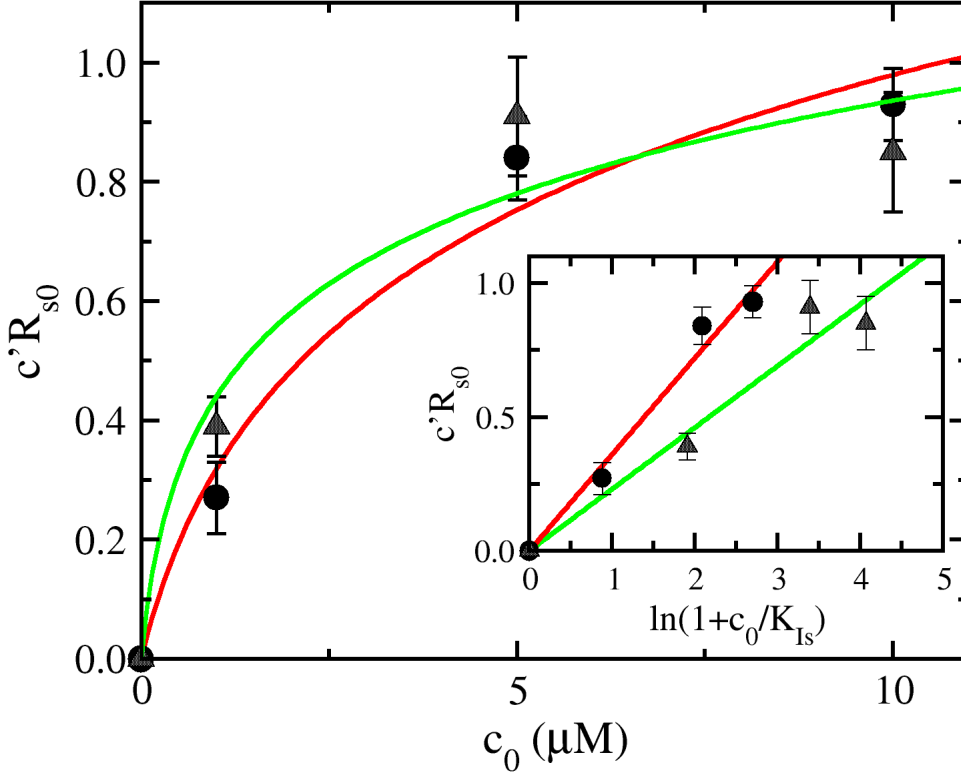


Figure 5.7: Amplitudes of the non-dimensional response functions. The solid circles and shaded triangles are for measured  $c'R_{f0}$  and  $c'R_{b0}$ , respectively. According to the MWC model of Ref. [86],  $c' = t_0 \ln(1 + c_0/K_{Is})$ . The red and green lines are fits using respectively  $(t_0R_{f0}$  and  $K_{If})$  and  $(t_0R_{b0}$  and  $K_{Ib})$  as parameters. The appropriateness of the logarithmic  $c_0$  dependence is further illustrated in the inset. Our fitting procedure yields:  $K_{If} = 0.71 \pm 0.02 \mu\text{M}$  and  $R_{f0}t_0 = 0.36 \pm 0.04$  for the forward (red curves) interval, and  $K_{Ib} = 0.17 \pm 0.02 \mu\text{M}$  and  $R_{b0}t_0 = 0.23 \pm 0.05$  for the backward (green curves) interval.

only a positive lobe in short time. Thus, when the bacterium swims backwards, its chemotaxis network performs only signal amplification but no comparison. Because the short-time lobes are positive in both forward and backward response functions, the bacterium extends both swimming intervals when encountering a chemoattractant. However, because the positive lobe of  $R_f(t)$  integrates to a larger value than  $R_b(t)$ , an identical chemical stimulus will elicit a greater response in the forward direction than in the backward direction, which is consistent with the CCW bias data in Figure 5.5.

Another notable achievement of this experiment is the identification and quantitation of the indirect response functions  $R'_f(t)$  and  $R'_b(t)$ . These functions has a large amplitude so that the nascent state is inhibited from switching in a short time, which gives rise to the non-Poissonian motor switch phenotype. The existence of these indirect responses is a manifestation of the fact that a bacterium possesses a continuous memory and it is transmittable to subsequent swimming intervals.

### 5.3.4 Difference between $k_f(t)$ and $k_b(t)$ persists in the case of longer exposure to serine

In Section 3.0.1, we had mentioned the fine structures observed in the response of *V. alginolyticus* to extended exposure to serine. These structures become more prominent when  $t_w$  increased from 0.3 s to 1.5 s but become weaker for  $t_w \geq 3.1$  s. Our ability to resolve the rotation degeneracy in the optical trap motivated us to reexamine these fine structures in the response functions. The experiment was performed as described in Section 3.0.1 using an ensemble of  $n \sim 800$  cells. In the experiment, the serine concentration in the micropipette was  $c_0 = 10 \mu\text{M}$ , the bacterial exposure time was kept at  $t_w = 1$  s, and each run lasted only 3 s. The data for this mixed ensemble is displayed in Figure 5.8. The switching rates from forward to backward and backward to forward,  $k_f(t)$  and  $k_b(t)$ , respectively, were calculated following the analysis scheme described in the previous section.

As seen in Figure 5.8(E),  $k_f(t)$  goes through a very sharp transition at  $t \simeq 1.5$  s, i.e., while the switching rate of most of the forward-swimming cells is repressed with  $k_f \simeq 0$  for  $t < 1.2$  s,  $k_f$  reaches a maximum rate  $5 \text{ s}^{-1}$  rapidly at  $t = 1.6$  s. In contrast, the backward swimmers

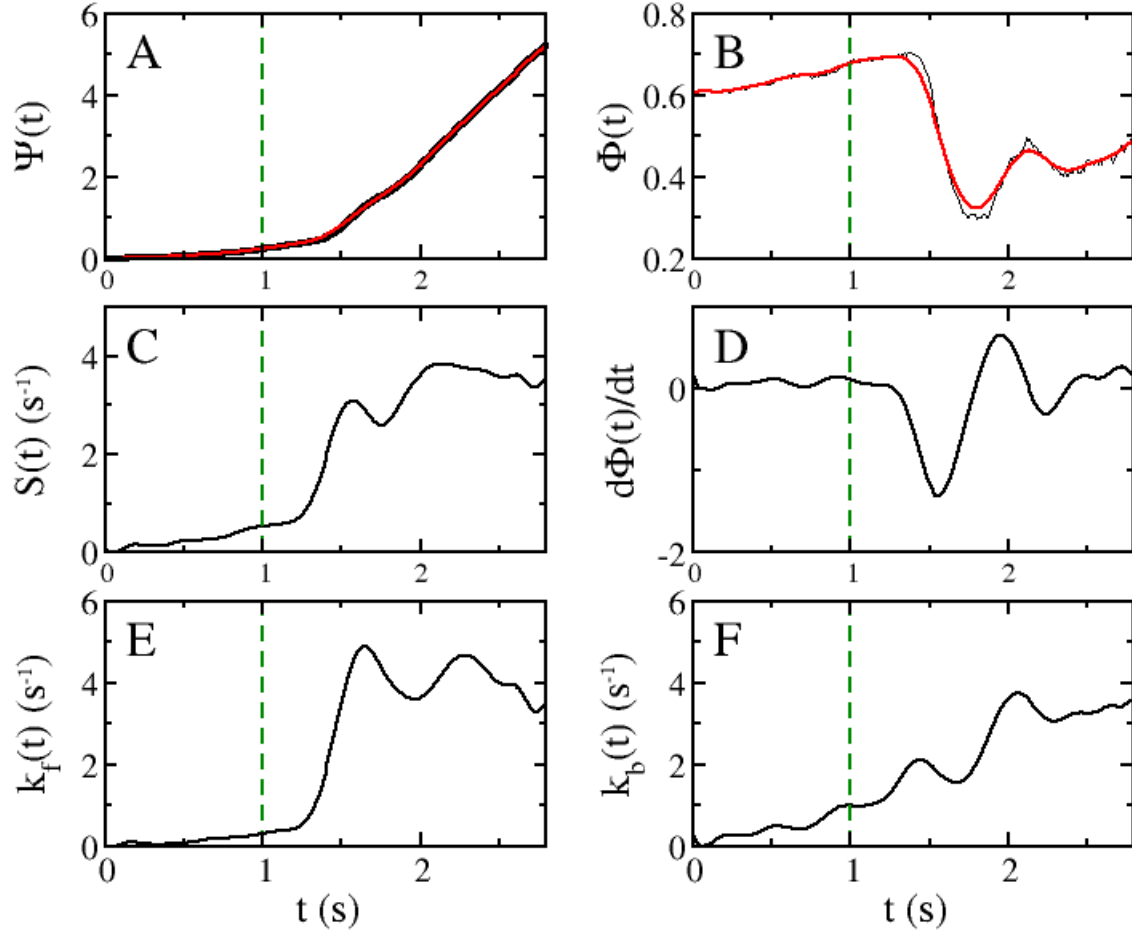


Figure 5.8: Mixed ensemble measurements for prolonged exposure to serine. Plotted in (A) is the cumulative distribution function  $\Psi(t)$  of the switching events for an ensemble of  $n \sim 800$  cells. (C) displays the switching rate  $S(t) = d\Psi/dt$  obtained from (A). In (B) and (D), the CCW bias  $\Phi(t)$  and its derivative  $d\Phi/dt$  are plotted, respectively, as a function of time.  $S(t)$  and  $d\Phi/dt$  from (C) and (D), respectively, were used in Eqs. 4.1 and 4.2 to calculate  $k_f(t)$  and  $k_b(t)$ , which are plotted in (E) and (F). The vertical green lines indicate when the dragging begins.

leave their current state at a nearly constant rate as seen in Figure 5.8(F). These two different responses to a sharp decrease in the serine concentration underlines the previously observed differences in the response functions  $R_f(t)$  and  $R_b(t)$ . Namely, the forward response function  $R_f(t)$  consists of a positive lobe in short times and a negative lobe in long times and therefore is biphasic. This type of response enables *V. alginolyticus* to make temporal comparisons, and functionally it behaves like an edge detector. On the other hand, the backward response is more gradual, and therefore is unable to perform temporal comparisons.

## 5.4 DISCUSSION

This experiment brings up a number of interesting issues that we wish to discuss below:

### 5.4.1 Important features of the response functions are predictable based on *V. alginolyticus* motility pattern

In this work we have taken an unusual approach, i.e., based on the macroscopic motility pattern of a bacterium, we make predictions about how the chemotaxis behavior of such cells is regulated. This outside-in approach is in sharp contrast with the traditional inside-out approach that brings us to the current understanding of chemotaxis response in enteric bacteria *E. coli* [1, 80, 53, 77, 89]. In retrospect, the latter approach is a remarkable journey starting from Adler’s important discovery of chemoreceptors for chemical detection [1], to the discovery of methylation of receptors as a means of network adaptation [80], and culminating at the identification of the phosphorylation step as the short-time excitation of the network. The latter, known as the two-component regulatory system, turns out to be universal for prokaryotic as well as eukaryotic cells [84]. The manifestation of this sophisticated internal biochemical network at the behavioral level was unraveled by the response measurement employed by Block et al. [18, 74].

Although our calculated response is not entirely identical to what we measured, the calculation has captured salient features of the actual bacterial response, notably the existence

of a biphasic response with a positive and a negative lobe for either shared or independent chemosensing. Interestingly, our calculated response function, which by necessity is parametrized by the macroscopic quantities, such as the mean forward  $\tau_f$  and backward  $\tau_b$  dwell times, has a remarkable resemblance to what is derived for *E. coli* based on detailed molecular interactions in the biochemical network [3, 30, 86]. In fact one can even borrow the response function  $R(t)$  of *E. coli* cells and use it to mimic our experimental data [4]. For *E. coli*, Tu et al. showed that the response function for a impulsive stimulus is given by [86],

$$R(t) = R_0 \left[ \frac{1}{\tau_e} \exp\left(-\frac{t}{\tau_e}\right) - \frac{1}{\tau_a} \exp\left(-\frac{t}{\tau_a}\right) \right], \quad (5.26)$$

where  $R_0$  is the amplitude of the response, and  $\tau_e$  and  $\tau_a$  are the excitation and the adaptation times, corresponding to the phosphorylation and the methylation times in the cell. In the limit of fast adaptation,  $\tau_a \simeq \tau_e$ , Eq. 5.26 reduces to the critically damped harmonic oscillator response as well, similar to Eq. 5.19. For the more general case when  $\tau_a \neq \tau_e$ , there is also a one-to-one match of the internal and external time scales, i.e.,  $\tau_e = \tau_b$  and  $\tau_a = \tau_f$ . This may be a coincidence, but the fact that they have such a similar functional form suggests that *E. coli*'s response is capable of regulating 3-step motility pattern for chemotaxis. Moreover, from an engineering point of view, the response function behaves like the response of a critical damped harmonic oscillator is sensible as it confers a fast response and is stable over a broad range of time or frequency scales [93].

It must be pointed out that our experimental finding is not identical to the theoretical prediction, which suggests instead that forward (backward) should be monophasic (biphasic). We believe that this discrepancy results from optimization of the drift velocity that demands the overlapping integral in Eq. 4.5 being maximized. While this simple approach is appealing [29, 27], its biological relevance is questionable. We think a more appropriate way for optimization is to calculate the drift velocity to higher orders. These high-order terms result from the coupling between diffusive motion and the deterministic drift and have a deteriorative effect of reducing the drift velocity. The balance of the linear and the high-order terms therefore can provide a strong motivation for optimization. This is a demanding calculation but is currently underway.

### 5.4.2 Independent sensing of 3-step swimmers enables an exploration-exploitation behavior

We believe that by virtue of backtracking and having the dwell times  $\tau_f$  and  $\tau_b$  to be close to each other ( $\tau_f \simeq \tau_b$ ), a 3-step swimmer has the innate ability to localize near a point source of attractant, and thus the chemo-response with a positive and a negative lobe is perhaps not directly useful for cell localization as suggested for peritrichously flagellated bacteria [27]. Rather such a response function, in our opinion, is primarily for rapid migration of cells in a chemical gradient with a large sensing range [18, 74].

A conspicuous feature of our measurements is that the biphasic response is primarily in the forward (CCW) interval, which has a large positive lobe and an extended negative lobe, whereas the response in the backward (CW) interval is more-or-less monophasic. We posit that this regulation scheme enables the bacterium to exploit nature using an exploration-exploitation strategy, which is common in animal kingdom [8]. Imagine that a bacterium pursues a local source of attractant by gradient sensing. The cells can go as far as possible (allowed by the Poisson time) in a positive gradient direction [53]. However, because of the negative lobe, the cell will not know if it has surpassed the peak of the gradient until some times later. For *E. coli* it is  $\sim 3 - 4$  s but for *V. alginolyticus* it is a fraction of second for small signals. Overshooting the peak is undesirable for any microorganism. However, for a 3-step swimmer executing the run-reverse-flick motility pattern this is not a problem; a motor reversal ensures that the cell will move up the gradient and back to its previous good territory. Hence, the way the response is implemented in *V. alginolyticus* appears to be more “purposeful” in that in the forward swimming phase, the bacterium explores the space by gradient sensing but in the backward interval, it exploits it. It is evident that for exploration a memory (or negative lobe) is required allowing the cell to compare chemical environments from one place to next in about one second, but for the exploitation phase, the signal comparison is unnecessary; the cell simply takes whatever is available based on information collected during the forward run. Mathematically, it can be shown that a long memory time in the swimming interval preceding a flick is not desirable because the information passes on to the next run interval cannot be used by the cell (or may even

interfere with its chemosensing) after the direction randomization [91]. This contributes to an unnecessarily large diffusivity of the bacterium, spoiling its ability to localize near a small source. Thus a short memory time preceding the flick step is beneficial to the cell, and we believe the long memory time in *E. coli* contributes to its inability to localize near a small chemical source [91].

### 5.4.3 The measured response has strong implications for how the chemotaxis network is wired in *V. alginolyticus*

Our observed responses in *V. alginolyticus* have interesting implications for the network structures and protein-protein interactions in the chemotaxis network of this bacterium. These will be discussed below:

(a) Existing experimental observation suggests that *E. coli* cells perform chemotaxis by comparing receptor coverage in the recent 1 s with those taking place 3-4 s earlier. The earlier status of receptor coverage is registered by the methylation level of the receptor complexes. Our experimental data in Figure 5.5 also exhibit behavior that is consistent with temporal comparison but it occurs only when the stimulation becomes strong enough. For weak stimulation, the response in both forward and backward swimming direction is monophasic. Without being tempered by the negative lobe in the response function, the chemotaxis network in this weak stimulation regime behaves like an amplifier rather than a comparator. We posit that this gives the bacterium the sensitivity it needs to perform chemotaxis in an environment with low levels of nutrients. This is perhaps evolutionarily advantageous because when the signal is weak and sporadic, signal amplification is more important than signal comparison; the latter tends to reduce the sensitivity of the network.

Our experiment also shows that the negative lobe is far more prominent in the forward response function than in the backward ones. While our current experiment implies that the backward swimming interval is non-adaptive, it certainly cannot exclude the possibility that this negative feedback loop would be engaged only when a stronger or more prolonged stimulation is present. The currently accepted paradigm is that the adaptive response is

due to a negative feedback loop, which is biochemically accomplished by (de)methylation of chemoreceptors. If *V. alginolyticus* use this same pathway, our measurements show that the negative feedback becomes engaged in a different way depending on bacterial swimming direction. This also implies that the control of the motor switch is not a “one-way street” as in *E. coli*. By an unknown mechanism, the receptor complex in *V. alginolyticus* knows the current state of the motor and reacts accordingly.

For *E. coli* cells, it is thought that the methylation step is independent of ligand binding; i.e. the rate of methylation  $F$  only depends on activity  $a$  or  $\dot{m} = F(a)$  [9, 86]. Our observation suggests that for *V. alginolyticus*,  $F$  not only depends on  $a$  but also the ligand concentration  $c$  and the direction of swimming, i.e.,  $\dot{m} = F_s(a, c)$ , where  $s = f, b$ . Thus, the  $F$  function is more sophisticated than that of *E. coli* and can give rise to interesting behavioral responses that are yet to be characterized and understood in future experiments.

(b) Our measurements also suggest that the relevant time scale in the network  $\tau$  may not be constant but changes with the stimulation level. In this regard, a single response (or Green’s) function that is capable of processing complexed chemical signals appears to be too simplistic. This may be the case for *E. coli* but for *V. alginolyticus*, we have witnessed a continuous change of time scales, particularly the adaption time, as  $c_0$  increases.

(c) In terrestrial bacteria, such as *E. coli* and *B. subtilis*, it is known that (de)phosphorylation dynamics in the chemotaxis network are among the most rapid and efficient processes in the two-component response systems [82, 19]. The processing time in *E. coli* is  $\sim 1$  s. Here, we have witnessed that in *V. alginolyticus*, this important regulation step is even faster, raising the interesting question about what is the intrinsic time limit for chemical communications inside a bacterium. We believe that this rapid processing time is required in ocean because such environment is characterized by low nutrient contents, where dissolved organic carbon is in the nanomolar range [65] and is rapidly dispersed due to turbulence. To survive, therefore, it is crucial for *V. alginolyticus* to have a fast response system, which is evident not only by its signal processing time delineated above but also in its swimming speed  $v_{sm}$ ;  $v_{sm}$  up to  $\sim 200 \mu\text{m/s}$  has been reported [57]. What would be the ultimate processing time given such a high swimming speed? Purcell postulates that for motility to be beneficial, a bacterium must out-swim the diffusion of nutrient molecules, which corresponds to a minimal distance

$L_c \simeq D/v_{sm}$  or a time  $t_c \simeq D/v_{sm}^2$ , where  $D$  is the diffusion coefficient of the molecule [69]. Taking serine as an example with  $D \simeq 900 \mu\text{m}^2/\text{s}$ , if  $v_{sm} \simeq 200 \mu\text{m}/\text{s}$ , it implies  $L_c \simeq 4.5 \mu\text{m}$ , which is only about 2-3 times the length of the bacterium or  $t_c \sim 23$  ms of processing time.

While we do not know at present how *V. alginolyticus* achieve such a rapid signal processing, the following considerations are relevant. First of all, the enzymes involved in phosphorylation and methylation in *V. alginolyticus* must be efficient with large rate constants. Moreover, since many biochemical reactions are diffusion limited, spatial arrangements of chemotaxis proteins inside the cells can also play a role. To shorten the reaction time, it may be important to make the “sink” and “source” next to each other. In *Vibrio* species, there is evident showing that receptors are clustered near cell poles where the flagellar motor locates [59, 36]. One can perform a back-of-the-envelope calculation to see how close the signal processing units, such as the receptor complex and the motor switching box, need to be in order to reach the observed reaction time. Intracellular measurements showed that the diffusion constant of CheY-P in *E. coli* is  $D \simeq 10 \mu\text{m}^2/\text{s}$ ; the same is to be expected in *V. alginolyticus* [28]. The minimum excitation time is then limited by the diffusion time  $L^2/2D$ . In our experiment with a weak stimulus, the excitation time is  $\sim 0.2$ s and this demands a distance no longer than  $L \simeq 2 \mu\text{m}$ , which is satisfied because the typical length of our bacteria is a few microns in size. For the minimum processing time  $t_c \sim 40$  ms, however, a much shorter distance is required, and it seems that in this case the receptor cluster and the motor have to be on the same pole.

#### 5.4.4 Chemotactic response is conserved in *V. alginolyticus* and in *E. coli*

It is remarkable that despite significant behavioral differences, one executing run-reverse-flick and the other run-tumble, and the different logical controls of their flagellar motors, the chemotaxis response functions in *V. alginolyticus* and in *E. coli* are nonetheless very similar. We are also impressed by the fact that such similarity exists in the presence of considerable divergence in the genes encoding the chemotaxis functions. For instance, sequence alignments for relevant *che* genes in *E. coli* and *V. alginolyticus* reveal that even for the closest match, *cheY*, the identity and similarity indexes are 64% and 84%, respectively. For other genes,

such as *cheA*, *cheB*, *cheR*, *cheW*, and *cheZ*, these indexes are much lower with identity inbetween 20 – 30% and similarity in 40 – 50%. Thus, it can be concluded that evolutionary forces are primarily acting on the functionality of the gene network rather than on the coding sequences. In the current study, it shows chemotaxis enabled by adaptation is remarkably conserved in the *V. alginolyticus* and in *E. coli*, indicating its importance in the survival of species. In future work, it will be helpful to clarify to what extent this property is preserved in other bacterial species adapted to different habitats.

## 5.5 CONCLUSION

Using optical trapping and conditional stimulation, we show that marine bacterium *V. alginolyticus* use different responses to regulate their forward and backward swimming intervals. Our measurements indicate that  $R_f(t)$  is biphasic but  $R_b(t)$  is monophasic in the concentration range used in the experiment, but the characteristics of the response functions, such as the short excitation time and the long adaptation time are not constant but appear to be continuous functions of the ligand (serine) concentrations. Compared to *E. coli*, a distinguishing feature of *V. alginolyticus* is its remarkably short adaption time, which, based on our measurement, is nearly identical to the excitation or (de)phosphorylation time. Such fast adaption may be crucial for bacterial chemotaxis in marine environment where competition between cells and localization around small nutrient patches all conspire to make the fast response favorable. Another distinguishing feature between the two species is that while *E. coli* regulates its motor bias, *V. alginolyticus* regulates its switching rate. For polar flagellated bacteria, controlling the switching rate makes biological sense because this type of cells produces motility in both forward and backward directions. This symmetry therefore determines that the motor bias in a steady state is  $\sim 50\%$  as seen in our experiment [92]. The symmetry still persists even under stimulation since a good (bad) stimulus will prolong (shorten) the duration of either interval. This rate regulation scheme however would be extremely awkward for chemotactic regulation of peritrichously flagellated bacteria as a simple gedanken experiment could readily demonstrate, and is therefore biologically unsound.

We are pleased to see that salient features of the response functions can be theoretically predicted, and the issue of whether the marine bacterium uses independent or shared chemosensing is finally clarified [6]. Remarkably, this biphasic response function was originally predicted based on the 3-step motility pattern with the sole requirement of optimal migration speed along a linear chemical gradient. This is in sharp contrast with the case of enteric bacteria *E. coli* for which motility pattern alone is insufficient to predict their response function as first pointed by de Gennes [29] and later confirmed by Clark and Grant [27]. We believe that the success in predicting *V. alginolyticus*' response relies on the fact that cell localization may never be a problem for the 3-step swimmer due to its back-tracking ability and because the ocean is a relatively simple habitat; quickly targeting the source of a nutrient perhaps is the most important attribute for survival and high fitness. It also demonstrates that for bacteria that inhabit more complicated environments that impose multiple demands on the cells, this outside-in approach would have much less predictive power. This however is commonly encountered in many ecological problems.

What we have not accomplished here is the clarification of how the switching logic and differential adaptive steps are implemented by the molecular machinery in *V. alginolyticus*. In future experiments, it would be extremely fruitful to investigate the internal chemical network and its reaction kinetics. In this way our measured chemotactic response functions can be built on the solid footing of molecular interactions. An inside-out approach is therefore urgently called for.

## 6.0 SYMMETRY PROPERTIES OF BACTERIAL POLAR FLAGELLAR MOTORS

### 6.1 INTRODUCTION

Motility is beneficial for all bacteria whose size exceeds roughly half a micron. For bacteria with size smaller than that the rotational diffusion of the cell body is too rapid for reliable taxis toward a chemical source [65]. An implication of this observation is that even for sizable bacteria, such as *E. coli*, their swimming paths need to be constantly corrected. Unlike higher-level organisms who use spatial sensing and a neural network to guide their motion, bacteria use temporal sensing and a stochastic approach to navigate in a noisy environment [81]. In the absence of a chemical signal, bacteria execute what one may call a random walk but in the presence of a chemical signal, this random motion is biased [13]. Evidently, random motion might be a bacterium's best or only choice given an environment that is completely stochastic and unpredictable, but it is not difficult to imagine that certain habitats are more-or-less structured. In this case, would the bacterium develop a different strategy to maximize its nutrient uptake? If so, how is this strategy carried out by the hardware (the propulsive apparatus) and the software (the chemotaxis network) of the bacterium? We wish that our experimental findings reported herein will shed some light on these interesting questions.

Symmetry plays a central role in physics. There are reasons to believe that the same holds true in biological systems. In physics symmetries imply conservation laws. In biological systems however the significance of symmetry is less clear but its manifestation at a behavioral level may give some useful clues. Let's take the bacterial flagellar motor as an example. In most peritrichously and polarly flagellated bacteria, the motors are bidirectional, capable of rotating either in the CCW or CW direction. For left-handed flagella, the CCW

rotation allows peritrichously flagellated bacteria, such as *E. coli* and *B. subtilis*, to form a bundle, providing a thrust to the cell body. When the motors turn in the CW direction, the flagellar bundle falls apart and the bacterium loses its ability to swim. But this seemingly futile (tumbling) interval serves an important biological function; it allows the bacterium to randomize its swimming direction and by chance it may head towards a more promising direction. Thus the two directions of motor rotation play different functional roles, one for swimming and other for reorientation. Hence, there is no compelling reason to expect that the CCW and CW rotation of the motor should be symmetrical, and in fact they are not. Existing experiments show that *E. coli*'s flagellar motor is asymmetrical in many different ways. For instance, the torque-speed relationship in the run interval is entirely different from that of the tumbling interval; in the former there exists two different regimes depending on the load but in the latter there is only a single linear regime [95]. Moreover, the motor is strongly biased toward CCW rotation, e.g., in a homogeneous medium without signals, *E. coli* spend  $\sim 90\%$  of their times swimming and other 10% randomizing their directions<sup>1</sup>. The preferential bias toward the CCW rotation in *E. coli* makes biological sense since CW interval is non-productive as no motility is produced. Lastly, measurements showed that in the absence of chemotaxis regulator CheY, *E. coli* motors run exclusively in the CCW direction, indicating that CCW rotation is the default state of the motor [72].

Let's now examine the swimming behavior of polar flagellated bacteria *V. alginolyticus*. This bacterium also has a left-handed flagellum. When the motor turns in the CCW direction, the flagellum pushes the cell body, which may be called forward swimming, but when the motor turns in the CW direction, the flagellum pulls the cell body, which may be called backward swimming. Due to low-Reynolds (Re) number hydrodynamics, CW rotation of the flagellar motor causes the bacterium to precisely backtrack its forward swimming trajectory when thermal noise is absent [69]. Recent studies have shown that cells of *V. alginolyticus* spend about the same amount of time swimming forward and backward [92]. The equal motor bias makes one wonder if there is a need or even it makes sense to specify the swimming direction. In a recent investigation however we found that forward and back-

---

<sup>1</sup>For individual motors, the CCW bias is smaller,  $\sim 60 - 80\%$ , indicating run and tumble are not determined by individual motors [72, 32].

ward symmetry in swimming of *V. alginolyticus* is broken in an unexpected way, i.e., the bacterium incorporates a flick movement of its flagellum during the transition from backward to forward swimming, causing the cell body to veer in a new random direction. Evidently, a flick is functionally equivalent to a tumble, and *V. alginolyticus*' swimming pattern therefore consists of a cyclic sequence of three steps, forward-backward-flick. During each swimming cycle, the swimming trajectories are strongly correlated, but there is no or little correlation between cycles. Very little is known about how the flick is initiated or for that matter its molecular components. The work reported below is our first attempt to address this issue.

## 6.2 RESULTS

### 6.2.1 Cell body and flagellar rotation frequencies in different swimming intervals

We found in our measurements that there is a large fraction of cells ( $\sim 80\%$ ) for which the  $+x_0$  and  $-x_0$  states (see Appendix A.2 for the definitions of the  $\pm x_0$  states) behave differently as a function of time. For the run presented in Figure 5.3, the  $-x_0$  state is more stable than the  $+x_0$  state, which is slanted as  $t$  increases in each interval. This difference between the  $+x_0$  and the  $-x_0$  states changes from cell to cell, suggesting that the orientations of the bacteria in the optical trap are random (see Figures 5.3(A-B)). The observed inclination in one of those states is therefore intrinsic to the flagellum dynamics of the bacteria and can be used to determine the sense of motor rotation. One also observes in Figure 5.3 that the transition rates from the lower to the upper state or vice versa are not the same; the former is faster than the latter. The above two characteristics are strongly correlated so long as these features could be identified in individual cells. Since the forward run is interrupted by a flick, it is reasonable to expect that the the slower transition is the switch from backward to forward (CW $\rightarrow$ CCW) swimming. Thus, the upper state in Figure 5.3 is the backward and the lower state is the forward interval. This designation of the rotation sense produces the same kind of dwell-time distributions (see Figure 5.4) as measured using free-swimming

cells, which indicates that our method is valid [5, 92].

Interestingly when analyzing the rotational angular frequencies in each swimming interval using power spectral analysis, we found that the spectral characteristics are also different for the  $+x_0$  and the  $-x_0$  state. This is illustrated in Figure 6.1 by the sequence of plots (I-VII) of the power spectra calculated using the windows specified in the time series  $x(t)$  (see the red boxes). We found that in the CW (backward) intervals, the cell body frequency  $\Omega_b$  is higher than that of the CCW (forward)  $\Omega_f$ ,  $\Omega_b > \Omega_f$ , but the trend is reversed for the flagellum rotations,  $\omega_b < \omega_f$ . This behavior is very peculiar considering that for swimming in low  $Re$ ,  $\omega$  and  $\Omega$  should be proportional to each other; when one increases, the other must also increase and vice versa. One can exclude the possibility that the anticorrelation is due to internal friction of the motor because in this case, say CCW is less frictional, we expect  $\Omega_b < \Omega_f$  and  $\omega_b < \omega_f$  and the frequency pair  $(\Omega_b, \omega_b)$  in Figure 6.1 should shift to the left uniformly relative to  $(\Omega_f, \omega_f)$ , but this is not what seen in *V. alginolyticus*. Because torque balance is required for free-body swimming, one can also exclude other internal mechanisms or processes that are energy conserving. Thus, whatever the cause of the anticorrelation, it must be due to an “external” agent. Running the time window continuously across the time series  $x(t)$ , the variations of  $\Omega(t)$  and  $\omega(t)$  with time can be calculated, and the result is displayed in Figure 5.3(D). The data show that  $\Omega(t)$  and  $\omega(t)$  are oscillating out of phase but are synchronous with the motor reversals.

We next investigated how the anticorrelation between  $\Omega$  and  $\omega$  observed in single cells behaves at the population level. For this purpose in Figure 6.2, a scattered plot is generated using pairs of  $(\Delta\Omega/\bar{\Omega}, \Delta\omega/\bar{\omega})$  collected from individual swimming intervals of many bacteria, where  $\Delta\Omega \equiv \Omega - \bar{\Omega}$ ,  $\Delta\omega \equiv \omega - \bar{\omega}$ , and  $\bar{\Omega}$  and  $\bar{\omega}$  are the mean values for the individual cell trapped. In the figure, each dot represents one of the swimming intervals for a trapped bacterium, and altogether  $n = 2117$  bacteria were used to generate the plot. We noticed that the data points are widely spread but the distribution is far from uniform. Specifically, most of the data points are clustered in the second and the fourth quadrants, corresponding to CCW and CW intervals, respectively. Thus, despite large cell to cell variations, the anticorrelation between  $\Omega$  and  $\omega$  is discernible even in a large population.

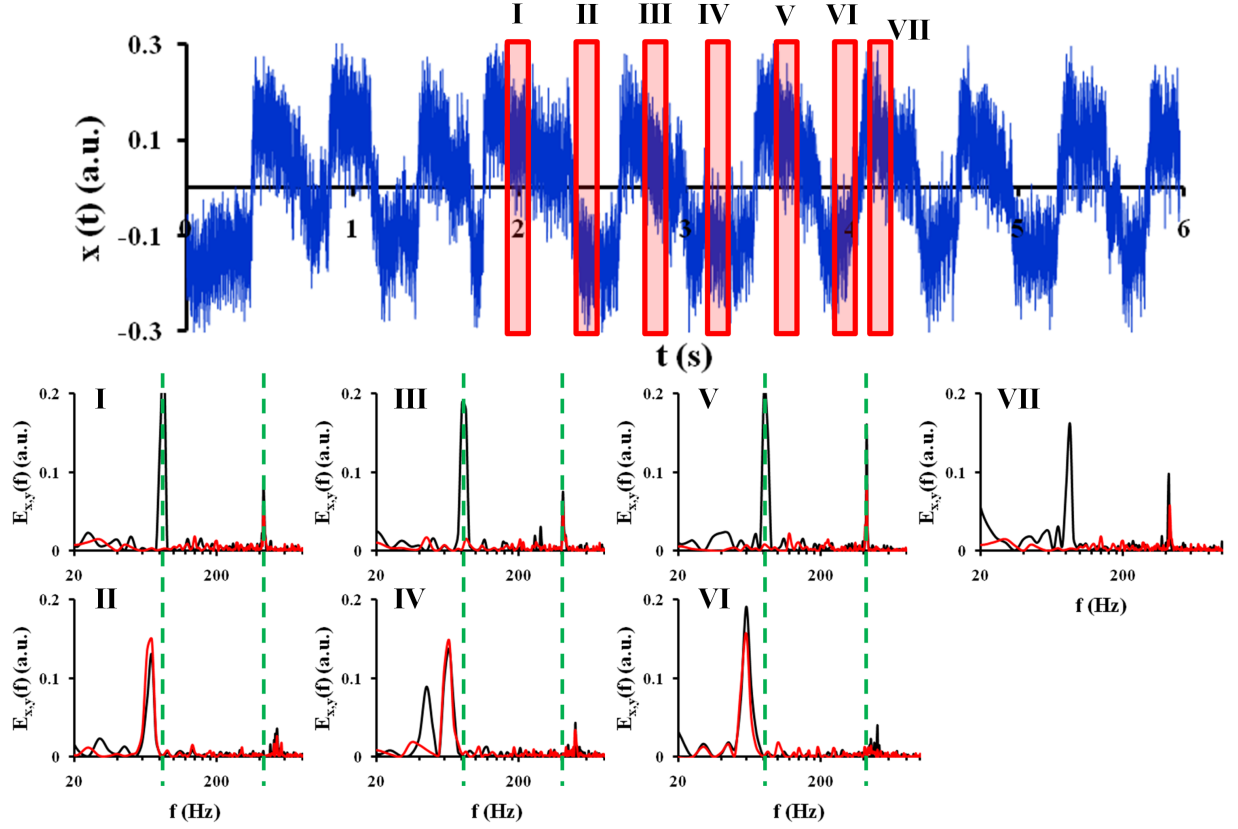


Figure 6.1: Simultaneous measurements of the cell-body  $\Omega(t)$  and the flagellar  $\omega(t)$  rotational frequencies. The consecutive CCW and CW intervals of the polar flagellum motor of a trapped *V. alginolyticus* are measured based on the time trace  $x(t)$ , which is plotted by the black line. To find the rotation frequencies  $\Omega(t)$  and  $\omega(t)$ , power spectra are calculated at different times  $t$  using a fixed window of 200 ms in width, which is delineated by the red boxes. Plots I-VII show the power spectra taken in different  $t$ , where the red and black curves correspond respectively to spectra calculated using the  $x$ - or the  $y$ -channel of PSD. As can be seen the spectra consist of two dominant peaks. The low frequency peak  $\Omega = 2\pi f_L$  corresponds to cell-body rotation and the high frequency peak  $\omega = 2\pi f_H$  corresponds to flagellum rotation. Note the anticorrelation between  $\Omega(t)$  and  $\omega(t)$  in consecutive swimming intervals, which are marked by the vertical green lines.

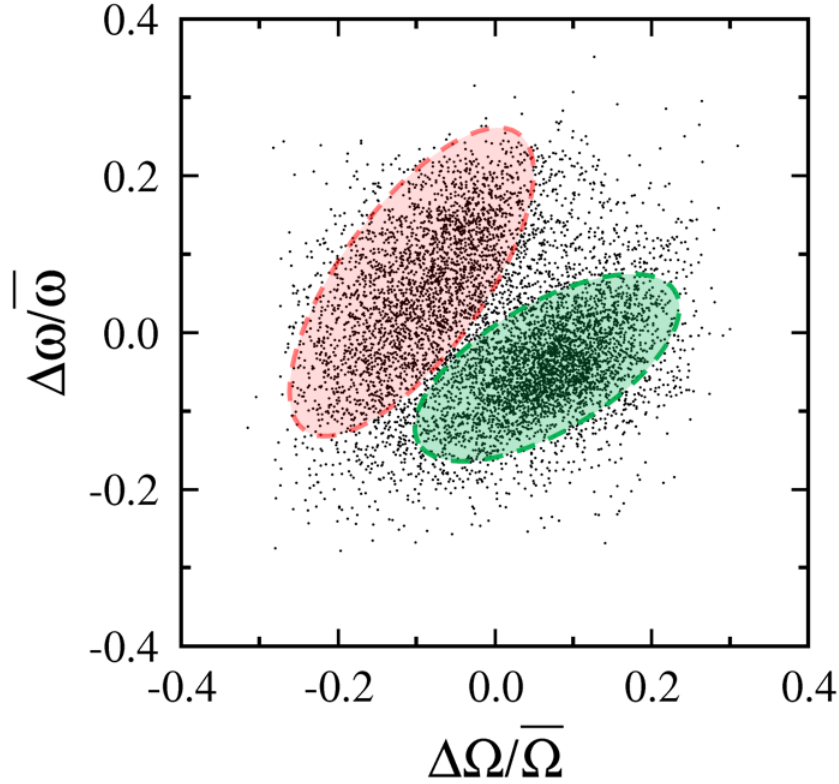


Figure 6.2: Correlations between cell-body and flagellum rotations. Each dot in the figure represents the relative change in the flagellum rotation frequency  $\Delta\omega/\bar{\omega}$  vs. the relative change in the cell-body frequency  $\Delta\Omega/\bar{\Omega}$  of a single swimming interval of a single bacterium, where  $\bar{\omega}$  and  $\bar{\Omega}$  are the mean values for the angular frequencies of the cell trapped. Altogether  $N = 7191$  intervals corresponding to  $n = 2117$  cells are presented in the plot. It is evident that  $(\Delta\Omega/\bar{\Omega}, \Delta\omega/\bar{\omega})$  are not distributed uniformly; they are clustered predominately in the upper-left and lower-right lobes, indicating anticorrelation between rotations of the cell-body  $\Omega$  and the flagellum  $\omega$ . As described in the main text, the lower-right and upper-left lobes are attributed to the bacterial backward (CW) and forward (CCW) swimming intervals, respectively.

Table 6.1: Statistics of rotation angular frequencies. The table shows the ensemble average of the cell-body  $\Omega$ , the flagellum  $\omega$ , and the motor  $\Omega^m$  angular velocity of a large number of bacteria ( $n = 1704$ ).

	$\Omega/2\pi$ (Hz)	$\omega/2\pi$ (Hz)	$\Omega^m/2\pi$ (Hz)
Forward	$73 \pm 18$	$493 \pm 78$	$566 \pm 82$
Backward	$84 \pm 19$	$452 \pm 62$	$535 \pm 64$

### 6.2.2 Asymmetries in the forward and the backward propulsion

Altogether  $n = 1704$  bacteria were measured and analyzed, each lasting for 6 s. All four angular frequencies,  $\Omega_f(t)$ ,  $\Omega_b(t)$ ,  $\omega_f(t)$ , and  $\omega_b(t)$ , were determined by time averaging for individual cells. We found in our experiment that some bacteria are more resistant to optical trapping (or “photo-damage”) than others. For instance, the bacterium shown in Figure 6.1 displays little laser effect but for the one in Figure 5.3(C), trapping causes it to stop switching after some time. In those latter cases, the last long period is ignored and is not included in the time average. Figures 6.3(A-C) display probability density functions (PDFs) for the cell-body  $\Omega_f$ , the flagellum  $\omega_f$ , and the flagellar motor  $\Omega_f^m \equiv \Omega_f + \omega_f$  angular frequencies for the forward swimming intervals. The corresponding PDFs for backward swimming intervals are displayed in Figures 6.3(D-F). We found that all these PDFs are broadly distributed and can be adequately fit by Gaussian functions,  $P(x) = \frac{1}{\sqrt{2\pi}\sigma} \exp\left[-\frac{(x-x_0)^2}{2\sigma^2}\right]$ , which are delineated by the green lines in the plots. For convenience, the results of the fitting procedure are listed in Table 6.1. It is conspicuous that the backward (CW) motor frequency  $\Omega_b^m$  is narrower than that of forward  $\Omega_f^m$ , and consequently the backward flagellum rotation frequency  $\omega_b$  is also narrow since  $\omega_b \gg \Omega_b$ . Despite broadness of the PDFs, however, the shifts in the ensemble means of forward and backward rotation frequencies are discernible and are consistent with anticorrelation,  $\bar{\Omega}_f < \bar{\Omega}_b$  and  $\bar{\omega}_f > \bar{\omega}_b$ , seen in individual cells.

Statistics of anticorrelation for individual cells can be analyzed more stringently by plotting the PDFs of the frequency ratios  $P(\Omega_f/\Omega_b)$ ,  $P(\omega_f/\omega_b)$ , and  $P(\Omega_f^m/\Omega_b^m)$ , which are displayed in Figures 6.3(G-I). Here the ratios were calculated based on the time average of

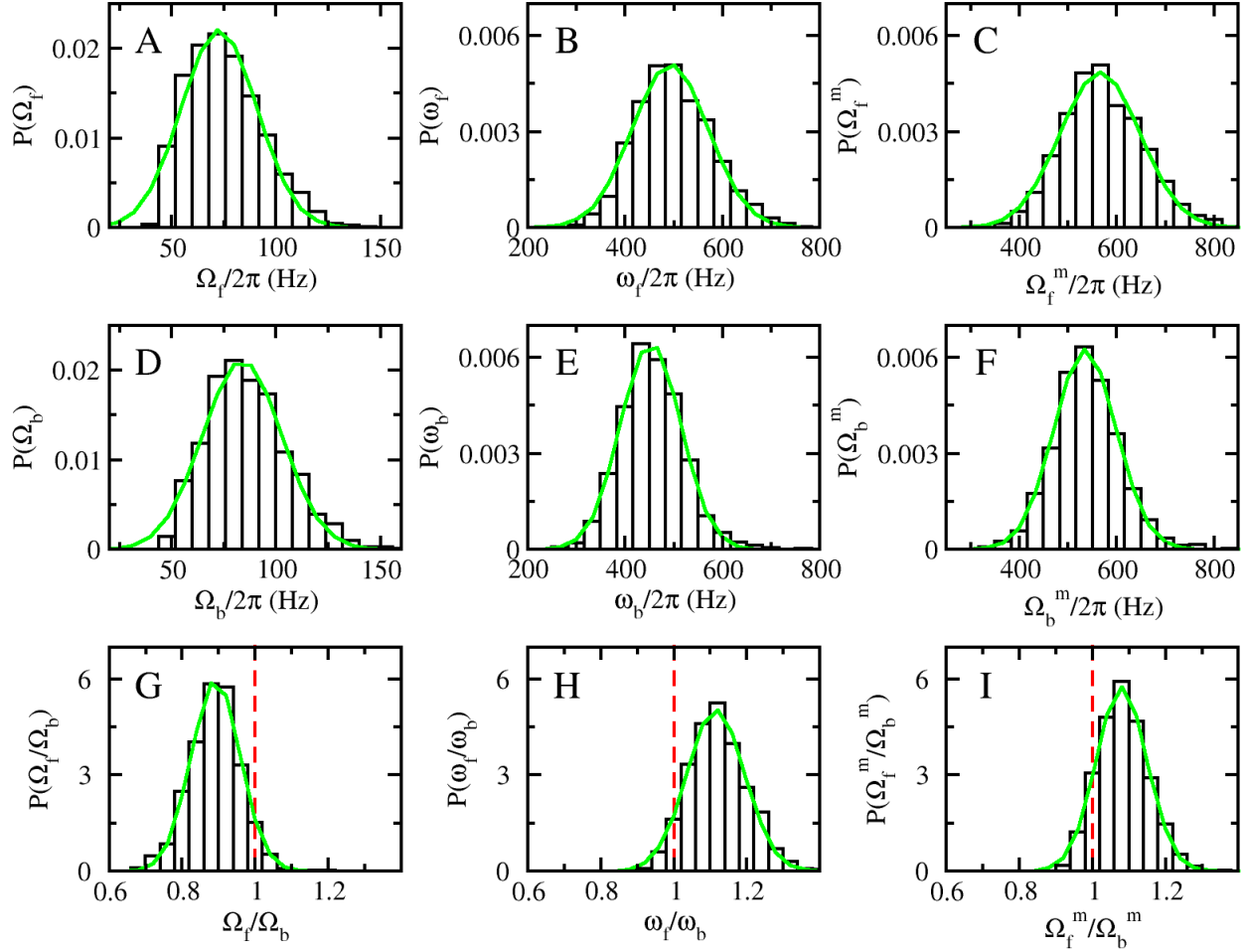


Figure 6.3: Probability density functions (PDFs) of angular frequencies and their ratios. The plots (A) and (D) show that overwhelming number of bacteria having their forward cell-body rotation slower than the backward cell-body rotation rate. On the other hand, the opposite is true for the flagellum rotation rates (see (B) and (E)). Plots also show that the motor speed in the forward direction (C) is slightly higher than in the backward direction (F). This indicates that for cells of *V. alginolyticus* the propulsion efficiency in the forward direction may not be as high as in the backward direction; it is as if in the forward interval, the motor is running empty with a lower load than backward. If the propulsive device (motor and flagellum) is symmetric, the frequency ratios,  $\Omega_f/\Omega_b$ ,  $\omega_f/\omega_b$ , and  $\Omega_f^m/\Omega_b^m$ , should be distributed with the peak at unity. However, this is clearly not the case as delineated by in (G-I) by the vertical red lines. Green lines in the plots are fits to a Gaussian distribution, where the mean and the standard deviations are listed in Tables 6.1 and 6.2.

frequencies of individual bacteria. For symmetrical swimmers, it is expected that these PDFs should peak at unity (see the red dashed lines) because for  $Re \rightarrow 0$ , the streamlines would not change but the velocity vectors associated with them simply reverse directions. The asymmetry in the PDFs is striking because the overwhelming number of cells are strongly biased, which is consistent with the scattered plot in Figure 6.2. One observes that for the cell-body,  $\Omega_b$  is  $\sim 10\%$  higher than  $\Omega_f$  and for the flagellum,  $\omega_b$  is  $\sim 10\%$  lower than  $\omega_f$ . However, for the flagellar motor,  $\Omega_f^m$  is only  $\sim 5\%$  faster than  $\Omega_b^m$  on the average. A higher forward motor speed suggests the following possibilities: (a) the motor is more powerful or (b) the load is smaller in the CCW direction. The latter could be the case if say the flagellum has two different conformations as a result of different motor directions, and one conformation is more efficient in propelling than the other. To differentiate these possibilities, it is helpful to determine the motor output power  $W_s = D_0 \Omega_s \Omega_s^m$ , where  $D_0$  is the rotational drag coefficient of the cell body, for the forward  $s = f$  and backward  $s = b$  intervals. It is fortuitous that our measurements also allow us to calculate the power ratio  $W_f/W_b \equiv \Omega_f \Omega_f^m / \Omega_b \Omega_b^m$  for individual cells. This distribution acquired from the large number of cells is plotted in Figure 6.4(B). It shows that the power output of the motor is higher, by  $\sim 5\%$ , in the backward than in the forward direction, which is contradictory to the possibility (a) but consistent with (b) above. Our experiment also allows us to determine the rotational drag of the flagellum in the fluid, which constitutes a major portion of the swimming load. Let us assume that during forward and backward swimming, the cell-body and flagellar axes are coaxial so that the torque balance demands  $D_s = D_0 \Omega_s / \omega_s$ , where  $D_s$  is rotational drag coefficient of the flagellum when the motor is in the rotation state  $s$ . Since the drag coefficient of the cell body  $D_0$  is expected to be constant, it follows that the ratio of the drag coefficient is given by  $D_f/D_b = \Omega_f \omega_b / (\Omega_b \omega_f)$  and can be determined for each bacterium. The PDF  $P(D_f/D_b)$  is presented in Figure 6.4(C). We were surprised to find that the mean value  $D_b$  is larger than  $D_f$  by as much as  $\sim 20\%$ , which is more than twice the standard deviation as shown in Table 6.2. The change in  $D_s$  is substantial if the effect is entirely due to flagellum deformation as will be discussed later.

In free-swimming bacteria of *V. alginolyticus*, our measurements have shown that the swimming speed in the backward direction is  $\sim 6\%$  higher than in the forward direction,

Table 6.2: Statistics of the asymmetry in polar flagellar motors of *V. alginolyticus*. For a symmetric cell, the means of these ratios should all be unity, but in the polar flagellum of *V. alginolyticus*, the deviation from this expected value is large as judged by the shift from unity in most of cases is greater than one standard deviation, except for the power  $W_f/W_b$  and the velocity  $V_f/V_b$  ratios.

$\Omega_f/\Omega_b$	$\omega_f/\omega_b$	$\Omega_f^m/\Omega_b^m$	$W_f/W_b$	$D_f/D_b$	$V_f/V_b$
$0.89 \pm 0.07$	$1.12 \pm 0.08$	$1.08 \pm 0.07$	$0.94 \pm 0.10$	$0.82 \pm 0.08$	$0.94 \pm 0.19$

which is delineated in Figure 6.4(A). This is consistent with the energy rate measurement above, showing  $W_b$  is greater than  $W_f$  by about the same amount. This is also consistent with the above torque measurement  $P(\Omega_f, \Omega_b)$ , showing  $\Omega_b > \Omega_f$ . Since the energetic argument is sufficient to account for the rotational bias, it appears unnecessary to appeal to flagellar deformation as a mechanism for the motor asymmetry seen in this experiment. This point will be elaborated further below.

### 6.2.3 Bias of flagellar motors in de-energized bacteria

Aside from the (a)symmetrical properties of flagellar motors, there is also the interesting issue concerning which motor state has a lower free energy. In wild-type bacteria the flagellar motor is regulated by the chemotaxis regulator (CheY) via a two-component system [83]. However, evidence shows that a flagellar motor switch is also influenced by factors such as membrane potential and the hydrodynamic load on the motor. In the pioneering work of Khan and Macnab, it was found that for *E. coli* and *B. subtilis* when the motor rotation frequency is about  $\sim 80\%$  of its maximum, it preferentially rotates in the CCW direction that rarely reverses [45]. These investigators went to a great length to rule out possibilities other than membrane potential that causes the observed behavior. Specifically, they found that the oxygen level, the ATP concentrations, the pH difference inside and outside bacteria, and the swimming load are irrelevant. However, recent findings due to H. Berg’s group at Harvard appear to be more complicated and summarized in Appendix D.

To see if this is also the case in *V. alginolyticus*, we examined our data set ( $5 \mu\text{M}$

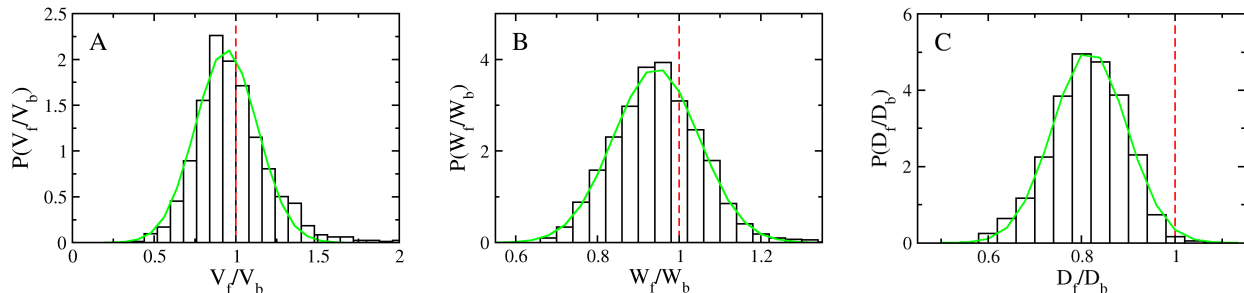


Figure 6.4: Swimming velocity, motor power, and rotation load PDFs. In (A), the PDF for the ratio of the forward and backward swimming speed is plotted for ( $n \sim 1000$ ) swimming cells. The velocity  $V_s$  here is the average velocity in the swimming interval  $s = f$  or  $s = b$ . The data is consistent with the power ratio  $W_f/W_b$  in (B) and the rotational load ratio  $D_f/D_b$  in (C) in that both an increase in the rotation power and a higher torque ( $N_b = D_0\Omega_b$ ) in the backward direction can yield a higher backward swimming velocity. However, unlike (B) and (C), the PDF for the velocity ratio has a much larger variance. This perhaps due to a large variation in the cell body sizes.

serine, no-delay) obtained in the optical trap. As mentioned above, there is a great deal of heterogeneity in the way the bacteria responded to laser trapping, while some show little or no laser effect, the others display what one may call de-energizing symptom. Specifically, we found that the motor speed and switching rate of these de-energized cells decrease with time while being trapped and once released from the trap, their swimming is not as vigorous as before they are trapped. A typical time trace  $x(t)$  of one of those cells is displayed in Figure 5.3(C). It is seen that for the first 3-4 s, the bacterium displays frequent motor reversals, then it slows down and becomes paralyzed at a particular rotation state. Studying ten randomly selected de-energized cells, we found that all of them become locked in the CCW direction if a long pause can be identified at the end of run. Thus we conclude that for de-energized *V. alginolyticus*, CCW rotation has a lower free energy, which is the same as *E. coli* motors. Why de-energized motors always locked in a CCW state and why de-energized cells do not switch their motors? Are these two phenotypes related to each other or just a coincidence? The answer to these questions will certainly shed light on how the flagellar motor of *V. alginolyticus* works and how its rotation is regulated. However, these interesting

and important questions are beyond the scope of current investigation and will be addressed in future experiments.

#### 6.2.4 Unusual motions of tethered *V. alginolyticus* bacteria

We observed that very small number of wild-type *V. alginolyticus* can stick to glass surfaces in such a way that the base of their flagellum appears to be glued to the surface. Some of these stuck cells move in a very peculiar way that may give hints on the asymmetry of bacterium swimming and the mechanism of flicking at the transition from backward to forward swimming.

A common feature of these stuck cells is that they protrude (or project) their cell body forward and remain in this extended position for a short period of time before retracting to their stuck position. Observations showed that the dwell time in the extended or contracted state is comparable or longer than CCW or CW intervals typically seen in free swimming cells, and in all the cases we observed the stuck positions are located at the base of the bacteria. We present and discuss below three cases (see video files CaseI, CaseII, CaseIII), among several, that were recorded by video imaging microscopy.

In case I, the tethered cell can roll on the glass surface with one of its poles as a pivot, which is delineated in Figure 6.6. Here, the center of the cell body moves in a small circle in the CCW direction as viewed from above the glass coverslip. When protruded, the cell body now moves in a large circle, but this time the motion can be in either CW or CCW direction. The precision by which the cell returns to its original position suggests that the tether must be very short, certainly not caused by an intact or partially sheared flagellum. In case II, the cell body is more or less stationary when not extended. Hence, it is difficult to judge its rotation direction. From video microscopy, it appears to be in an upright position when not extended. However, when projected, its body is parallel to the surface as shown in Figure 6.7. The cell body protrudes erratically in time but the distance it covered is rather consistent. In case III, which is displayed in Figure 6.8, the contraction and extension are more periodic in time. Similar to case II, in the contracted state the cell body is upright and appears motionless, but in the extended state, the cell body has limited lateral motions. A

common feature of these tethered cells, not restricted to the three reported here, is that the projection and contraction occur rapidly and is always along a straight line, which is clearly seen from the trajectories plotted. For the above three cases, we measured the x-y position of the cell body as a function of time, taking the tethering point as the origin. These x-y time traces are displayed by the black and red lines respectively in the corresponding plots. For convenience, we also plot the time trace of the radial positions  $r(t) = \sqrt{x^2(t) + y^2(t)}$  as a function of time, which is displayed by the black line.

Why do different tethered cells exhibit different behaviors? We believe that it all has to do with how close is the cell body to the glass surface. If the cell body is horizontal, parallel to the glass surface, the non-slip boundary condition dictates that the cell body must roll, which is case I. However, when the bacterium is projected away from the glass surface, the cell body and the surface hydrodynamic interactions become weak, and consequently the motion of the cell body simply follows a straight line as in case III. Using 100x immersion objective, which has a small depth of view, we confirmed that this was indeed the case for the cells observed. However, presently we are unable to tell the motor rotation direction when the cell body is extended or contracted.

Because bacterial flagella are tenuous, one of the possible explanations for what we observed is the unwinding of the left-handed helix [17]. However, this is not a satisfactory answer because (a) it is not consistent with the observation that the tethering point is at the pole of the bacterium, suggesting that the amount that could be unwind is limited, and (b) even unwinding of the full length of the flagellum is still short compared to the extension seen in our experiment. Here is a simple calculation of the length that can be liberated by unwinding the flagellum of *V. alginolyticus*. According to our early measurements [24], the flagellum is parametrized by the pitch  $\lambda = 1.2 \pm 0.2 \mu\text{m}$ , the radius  $R = 0.140 \pm 0.001 \mu\text{m}$ , and the length  $\ell = 3.7 \pm 1.0 \mu\text{m}$ . From these, one can easily calculate the contour length of the flagellum to be  $L = \ell / \cos \phi \simeq 4.6 \mu\text{m}$ , where the pitch angle  $\Psi = \tan^{-1}(2\pi R/\lambda) \simeq 36.24^\circ$ . Thus the maximum stretching possible for this bacterium is  $\Delta\ell (= L - \ell) \sim 0.9 \mu\text{m}$ , which is significantly shorter than our observed  $\Delta r \simeq 2 - 4 \mu\text{m}$  seen in Figures 6.6-6.8 .

Hence, the protrusion of the cell body could be due to an organelle, other than the flagellum, inside the cell that is flexible and can be extended over a large distance. One of

the possibilities is that the tethered cells possess a flagellum at each pole, with one stuck at its base, and the cell body is subject to pulling by the flagellum at the opposite pole as delineated in Figure 6.5. Since cells with flagella on both poles are not common and flagella tend to entangle, the proposed scenario can explain the rarity of tethered cells that can project and contract on surfaces and the fact why most of them are near other stuck cells. If the above picture holds, the organelle must have the remarkable property that it can rapidly change its conformation upon pulling and it is stiff enough not to break on tension. It remains an intriguing possibility that the native conformation of the organelle is also a left-handed coil, similar to the flagellum, and it is hidden inside the cell in the free swimming state (see Figure 6.5). To explain our observation, this organelle is not as stiff as the flagellum in that when in the CCW rotation, it winds up tightly forming a rigid joint, keeping the flagellum coaxial with the cell-body axis while forward swimming. However, when in CW rotation, the coil becomes somewhat loose forming a flexible joint so that the flagellum and the cell body may not be strictly coaxial. Implication of such flexible joint for a kink formation at the base of the flagellum and swimming direction randomization [92] will be further delineated in Section 6.4.

It is helpful at this point to analyze the force produced during the projection and the contraction phases of the tethered cells. Our data shows that the speed of projection is faster than contraction, indicating that the thrust in projection is larger than that of contraction. As an estimate we use case III as an example. Based on video microscopy, this bacterium extends radially outwards by  $\Delta r = 4 \mu\text{m}$  in about  $\tau_{ext} = 0.07\text{s}$ . This gives a velocity  $V \simeq 57 \mu\text{m/s}$  and is close to the free-swimming speed of the bacteria. The thrust is therefore  $F_{thrust} \sim 1 \text{pN}$  based on our earlier measurement [24]. However, proximity of the cell body to the surface and the resistance to pulling by the unknown organelle may alter the above thrust force estimate somewhat.

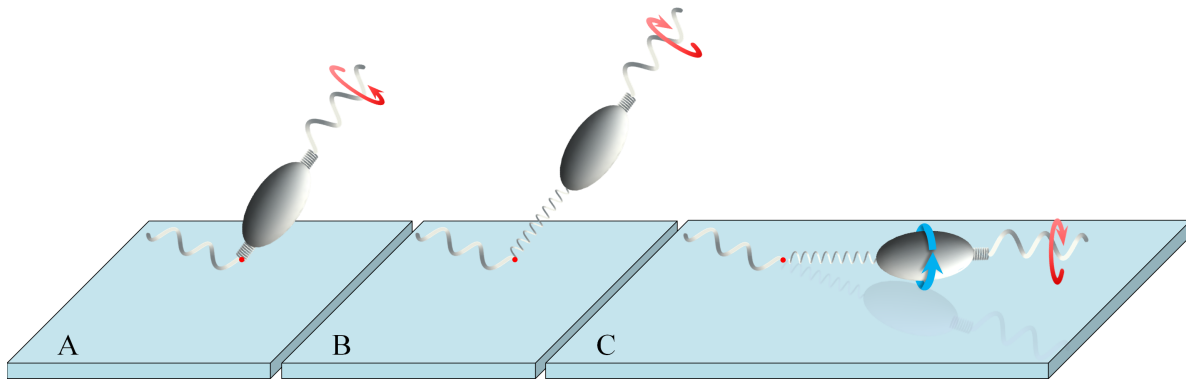


Figure 6.5: An hypothetical stretchable component in the flagellar motor of *V. alginolyticus*. To explain our experimental observation, we postulate that the polar flagellum is attached to the motor via a soft coil-like joint that has the same helicity as the flagellum itself. Our observed stretchable cells have the phenotype that they possess flagella on both poles. One of the flagellum is attached to the surface at a location indicated by the red dot. If the cell body is upright as drawn, it can be pushed (A) or pulled (B) by the flagellum on the other pole, if this flagellum is mature and functional. When pushed (CCW), the soft joint stiffens and the cell body appears to be attached to the surface, and when pulled (CW), the soft joint lengthens (or unwinds) and the cell body moves away from the tethering point as shown. If the cell body is pushed or pulled (C) near the surface, aside from lengthening the tether, the cell body can also roll on the surface, giving rise to circular paths as seen in Figure 6.6.

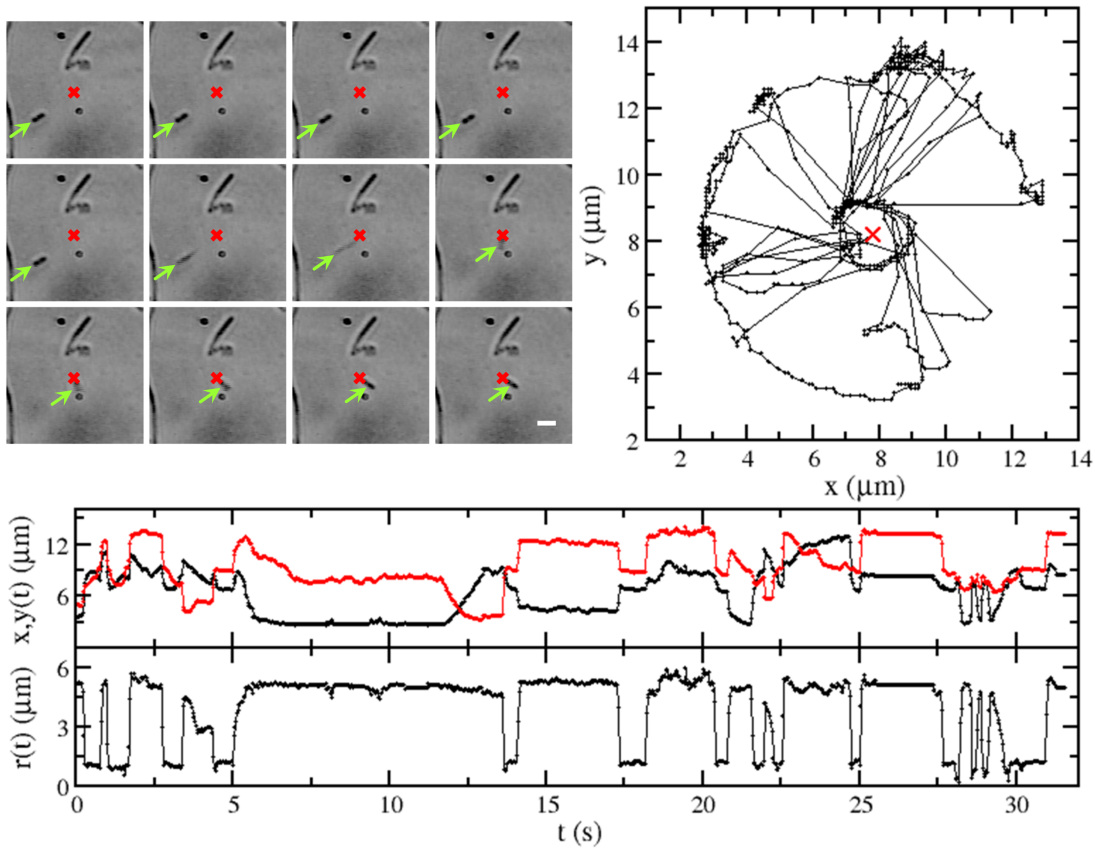


Figure 6.6: Case I: A horizontally tethered cell. The tethering point is marked by the red cross and the position of the bacterium itself is marked by the green arrows in the set of video images. It is evident that in both contracted and extended state, the bacterial cell body is horizontal, parallel to the glass surface. In both the contracted and the extended state, cell body rolls on the surface giving rise to the circular paths as shown in the bacterial track in the upper right corner. The plot in the middle is the  $x(t)$  (black) and the  $y(t)$  (red) position of the cell body as a function of time. The plot in the bottom is the radial position  $r(t) = \sqrt{x^2(t) + y^2(t)}$  of the cell from the tethering point.

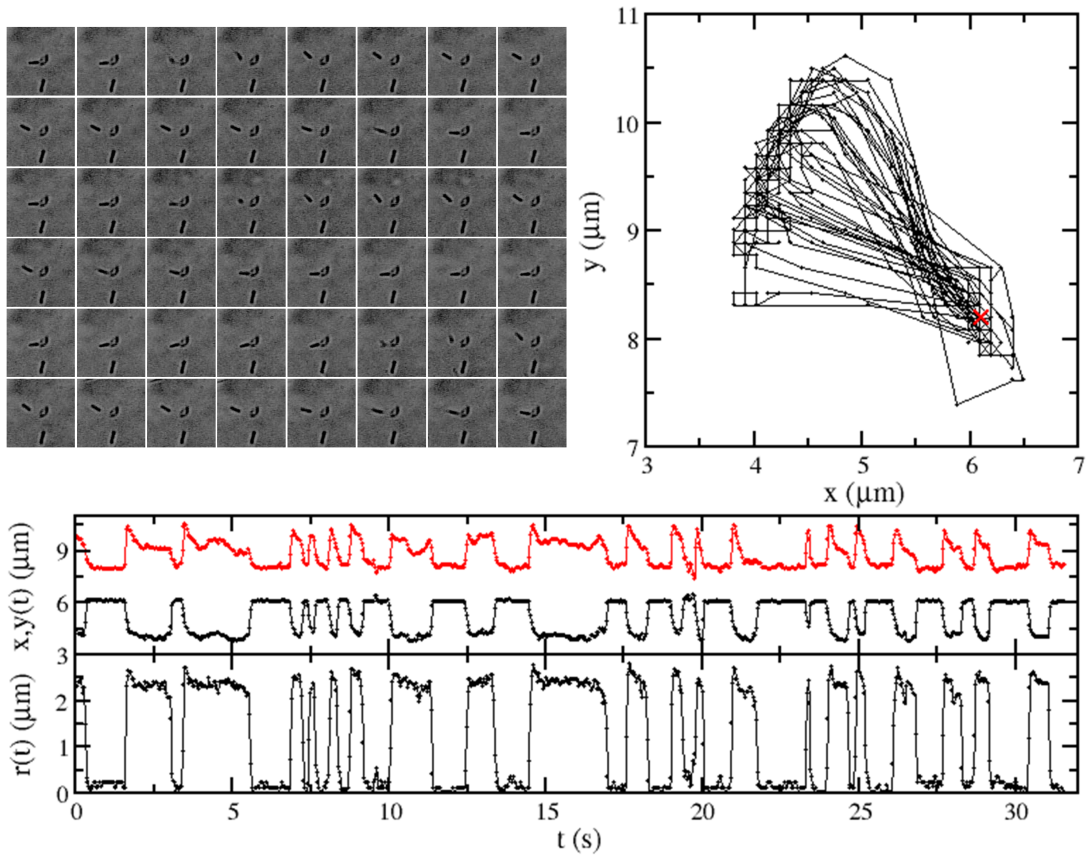


Figure 6.7: Case II: A nearly vertically tethered bacterium. This bacterium is nearly vertically tethered so that when in the contracted state, the cell body has a limited motion. The cell projects along a straight path and remains extended and moves about at a large distance from the tethering point. When retracted, it typically follows a different path from the projecting path as seen in the particle track depicted in the upper right corner. The middle and lower plots are respectively for the  $x(t)$  (black) and  $y(t)$  (red) positions, and for the  $r(t)$  positions of the bacterium as a function of time.

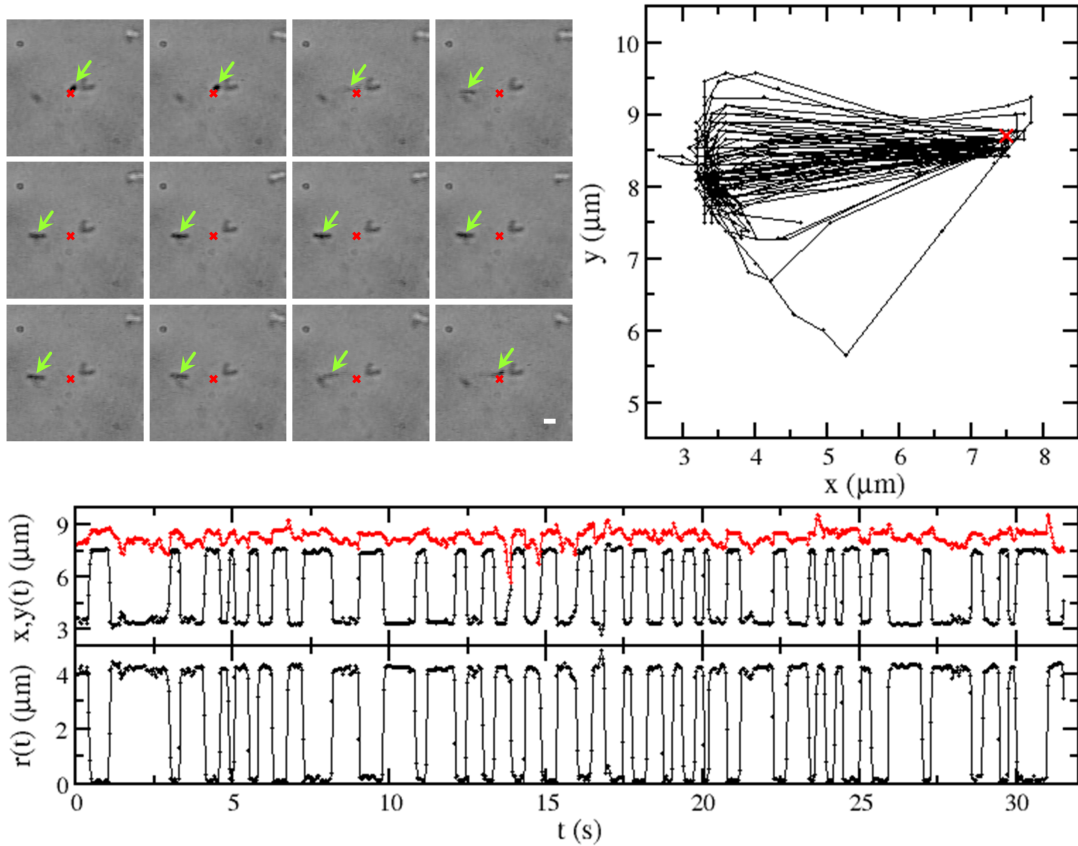


Figure 6.8: Case III: A vertically tethered bacterium. This bacterium is vertically tethered and when in the contracted state, the cell body appears motionless. The cell projects along a straight path and retracts along a path that is close-by. This suggests that in the extended state, the cell body is far away from the surface and hence it cannot roll (see the particle track in the upper right corner). The middle and lower plots are respectively for the  $x(t)$  (black) and  $y(t)$  (red) positions, and for the  $r(t)$  positions of the bacterium as a function of time.

## 6.3 THEORETICAL ANALYSIS

### 6.3.1 Deformation of flagellum in *V. alginolyticus* cannot account for the large difference in $D_f$ and $D_b$

A simple way to explain the large difference in  $D_f$  and  $D_b$  seen in our experiment is perhaps due to the conformational change when the motor changes its rotation direction. Morphological transformations in bacterial flagella are not uncommon and have been reported in *E. coli* and *Salmonella* [38, 88]. These transformations can be induced by motor reversals and are often accompanied by a strikingly large change in the overall shape of the flagellum. The effect was also investigated in polar flagella of *V. alginolyticus* [39, 66]. These latter studies were motivated by the original observations of Magariyama et al. who discovered the large asymmetry in the swimming speeds when the motor rotates in the CCW (forward) and the CW (backward) directions [56]. To characterize the asymmetry, the Magariyama et al. defined a velocity index  $I_v \equiv (V_f - V_b)/(V_f + V_b)$  for each bacterium, and the distribution  $P(I_v)$  for a group of 150 cells were measured. They found that  $P(I_v)$  was approximately normally distributed with the mean and standard deviation given by  $\bar{I}_v = -0.17 \pm 0.14$ . The PDF is strongly biased in the negative  $I_v$  (by more than one standard deviation), suggesting that  $V_b$  is greater than  $V_f$  by  $\Delta V/V \sim 37\%$ . This ratio is substantially higher than our experimental observations, which we found to be  $\bar{I}_v = -0.04 \pm 0.11$  in neutral TMN buffer,  $\bar{I}_v = -0.08 \pm 0.13$  in TMN+10 mM phenol, and  $\bar{I}_v = -0.05 \pm 0.10$  near a micropipette filled with 10 mM serine. Thus in our experiment,  $\bar{I}_v$  is at least a factor of two smaller. We suspect that the large discrepancy could result from the fact that our measurements were conducted in a bulk fluid but theirs were in a chamber with only  $\sim 1 \mu\text{m}$  gap. It may be that hydrodynamic interactions with surfaces are strongly asymmetrical in the forward and backward swimming directions, giving rise to the large difference seen in their experiment.

Using dark-field optical microscopy, Nishitoba et. al. studied the flagellum deformation of free-swimming *V. alginolyticus* [66, 39]. For a left handed helix, the CCW (forward) swimming causes the helix to tighten up, resulting in a slightly reduced pitch  $\lambda$  and CW (backward) swimming causes the helix to unwind, resulting in a slightly increased pitch.

Quantitatively,  $\lambda_0 = 1.27 \mu\text{m}$  for a non-swimming cell,  $\lambda_f = 1.23 \mu\text{m}$  and  $\lambda_b = 1.31 \mu\text{m}$  for a forward and backward swimming cell, respectively. Thus, the total deformation  $\Delta\lambda \equiv \lambda_b - \lambda_f \simeq 0.08 \mu\text{m}$  is  $\sim 6.3\%$  of the mean  $\lambda_0$ . Moreover, they found that the radius  $R$  of the helix does not change noticeably and they speculated that this is perhaps due to the fact that the pitch angle remains constant. For a fixed length of the flagellum, lengthening or shortening of  $\lambda$  results in the number of turns  $N$  in the helix to be changed; for the forward case,  $N$  changes from 2.84 to 2.92 and for the backward case, it changes from 2.84 to 2.77.

Nishitoba et al.'s measurement suggests that for *V. alginolyticus*, the flagellum deformation is considerably smaller than those seen in peritrichously flagellated bacteria. Essentially, unlike *E. coli* or *Salmonella*, there is no morphological transformation in *V. alginolyticus* and is consistent with our own experience. The small change in flagellum conformation due to different swimming directions was also confirmed by a theoretical calculation conducted by Takano et al. using a linear elastic theory [85]. The question we attempt to address below is whether the observed changes in flagellum pitch  $\lambda$  during forward and backward swimming is sufficient to explain the large change in  $D$  seen in our experiment. For convenience, we used the parameters used by Takano et al. since their modeling is for *V. alginolyticus* YM4 strain, which we used. For convenience, these parameters are listed in Table 6.3.

For a free swimming cell, the force and the torque balance equations are given by

$$-A_0V = AV - B\omega, \quad (6.1)$$

$$-D_0\Omega = -BV + D\omega, \quad (6.2)$$

where  $A_0 = 4\pi\eta b / [\ln(2b/a) - 0.5]$  and  $D_0 = 16\pi\eta a^2 b / 3$  are the linear and rotational drag coefficients of the bacterial cell body with the semi-major axis  $b$  and semi-minor axis  $a$ , and  $A$  and  $D$  are the linear and the rotational drag coefficients for the helical flagellum, and  $B$  is responsible for the propulsion of the cell body. The set of coefficients  $A$ ,  $B$ , and  $D$ , is positive definite and forms what is known as the propulsion matrix, which is symmetrical

[70]. Simple calculations show that they are given by,

$$A = K_n L (1 - \alpha^2) \left[ 1 + \gamma_k \frac{\alpha^2}{1 - \alpha^2} \right], \quad (6.3)$$

$$B = K_n L \left( \frac{\lambda}{2\pi} \right) (1 - \alpha^2) [1 - \gamma_k], \quad (6.4)$$

$$D = K_n L \left( \frac{\lambda}{2\pi} \right)^2 (1 - \alpha^2) \left[ 1 + \gamma_k \frac{1 - \alpha^2}{\alpha^2} \right], \quad (6.5)$$

where  $L$  is the total contour length of the flagellum,  $\lambda$  is the pitch measured along the  $z$ -axis of the flagellum,  $\alpha$  is the directional cosine of the pitch angle  $\Psi$  defined as  $\alpha \equiv \cos(\Psi)$  and  $\Psi = \tan^{-1}(2\pi R/\lambda)$ ,  $R$  is the radius of the flagellar helix, and  $\gamma_k (\equiv K_t/K_n)$  is the ratio of the tangential  $K_t$  to the normal  $K_n$  drag coefficient of a small segment of the flagellum filament. Following Lighthill's parametrization scheme [52], one obtains,

$$K_t = \frac{2\pi\eta}{\ln [0.18\lambda / (\alpha a_0)]}, \quad (6.6)$$

and

$$K_n = \frac{4\pi\eta}{\ln [0.18\lambda / (\alpha a_0) + 0.5]}, \quad (6.7)$$

where  $\eta$  is the viscosity of the fluid and  $a_0$  is the radius of the flagellar filament.

For  $L$  and  $R$  to be fixed, we rewrite Eqs. 6.3-6.5 in non-dimensional forms and they are functions of the wavenumber  $k = 2\pi/\lambda$  only. This yields

$$A/K_n L = \frac{R^2 k^2}{1 + R^2 k^2} \left( 1 + \frac{\gamma_k}{R^2 k^2} \right), \quad (6.8)$$

$$B/K_n L R = \frac{R k}{1 + R^2 k^2} (1 - \gamma_k), \quad (6.9)$$

$$D/K_n L R^2 = \frac{1}{1 + R^2 k^2} (1 + \gamma_k R^2 k^2). \quad (6.10)$$

This set of equations produces the anticipated results in the limits of  $k \rightarrow 0$  (a fully stretched helix) and  $k \rightarrow \infty$  (a fully compressed helix). In particular,  $B \rightarrow 0$  in both limits, indicating these types of flagellum morphologies are not capable of generating thrust, which is expected.

Table 6.3: Parameters for calculating flagellar deformation. We used the bacterial parameters, the fluid viscosity  $\eta$ , the semi-minor  $a$ , the semi-major  $b$ , the flagellum contour length  $L$ , the pitch  $\lambda$ , the radius  $R$ , and the filament radius  $a_0$  from Ref. [85]. The calculated flagellum drag coefficients in different swimming states are listed in the last column.

$\eta$ (kg/m · s)	$2a$ ( $\mu\text{m}$ )	$2b$ ( $\mu\text{m}$ )	$L$ ( $\mu\text{m}$ )	$a_0$ ( $\mu\text{m}$ )	$v$ ( $\mu\text{m/s}$ )	$\lambda$ ( $\mu\text{m}$ )	$R$ ( $\mu\text{m}$ )	$D$ ( $\times 10^{-21}$ kg · m <sup>2</sup> /s)
$1.3 \times 10^{-3}$	1	2	5.5	0.016	0	1.27	0.233	1.04
					100	1.23	0.232	1.02
					-100	1.31	0.235	1.05

Using the given  $R = 0.23 \mu\text{m}$  and approximating  $\gamma_k \approx 0.5$ , we plot Eqs. 6.8-6.10 in Figure 6.9. It is seen that as the wavenumber  $k$  increases, the propulsive coefficient  $B$  (black curve) becomes large first, passes through a maximum before it slowly declines. Thus, for this simple resistive force model, the maximum  $B$  occurs at  $Rk = 1$ . It is also seen that  $A$  (blue curve) and  $D$  (green curve) depend on  $k$  differently with  $A$  increases monotonically but  $D$  decreases monotonically with  $k$ . Based on the measured pitches given in Table 6.3, we found that for YM4, the wavenumber during forward swimming is slightly greater than in the backward swimming, which are delineated by the vertical dotted lines in the figure. It is evident from their intersections with the green curve, which is for  $D$  vs.  $k$ , we found that there is only a marginal change in  $D$  or  $D_f/D_b \approx 0.97$ , which is significantly smaller than that measured in the optical trap with  $D_f/D_b \approx 0.82$ . Hence, we conclude that conformational change in the pitch of polar flagellum is insufficient to account for the large rotational load observed in our current experiment.

Based on the above calculation, we can also compute the ratio of the swimming speeds in the two motor states. The swimming speed is given by,

$$V_s = B_s \omega_s / (A_0 + A_s), \quad (6.11)$$

where  $s = (f, b)$ . Thus the ratio is given by  $V_f/V_b = (\frac{B_f}{B_b})(\frac{\omega_f}{\omega_b})\frac{A_0+A_b}{A_0+A_f}$ . Our measurements ( $\omega$ 's) and calculations ( $B$ 's and  $A$ 's) show that  $\omega_f/\omega_b$  is by far the largest compared to  $B_f/B_b$  and  $(A_0 + A_b)/(A_0 + A_f)$ . We therefore expect  $V_f/V_b \simeq \omega_f/\omega_b > 1$ . However, this

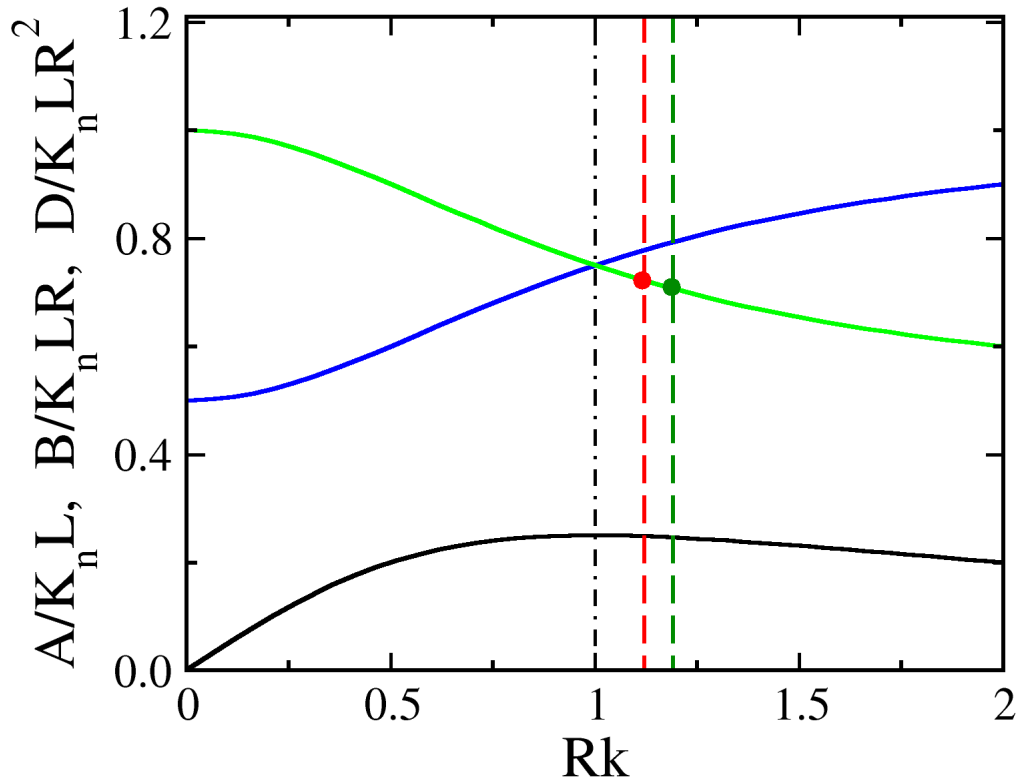


Figure 6.9: Effect of flagellum deformation on bacterial swimming. In the figure, non-dimensional linear drag coefficient  $A$  (blue), the propulsive coefficient  $B$  (black), the rotational drag coefficient  $D$  (green) of a helical coil are plotted. Here, the helix radius  $R$  is fixed but the wavenumber  $k = 2\pi/\lambda$  is varied. The vertical black line corresponds to the flagellar conformation with the maximum thrust force. The green and red vertical lines correspond to the flagellar conformations of *V. alginolyticus* (YM4) in the forward and backward swimming directions, respectively. We noticed that upon transition from the forward to the backward swimming,  $B$  hardly changes,  $A$  decreases slightly, and  $D$  (see the solid dots) also increases slightly. Quantitatively, the change in  $D$  is only a few percent instead of 20% as seen our measurements.

result is inconsistent with the velocity ratio measured in free swimming cells as delineated in Figure 6.4(A). This suggests that either the above resistive force theory is inadequate in predicting bacterial swimming in *V. alginolyticus* or there are other “degrees of freedom” in the bacterial swimming that has not been taken into account appropriately.

In the above calculation, we have used the set of parameters obtained when the bacteria are in the free-swimming state. The question is whether trapping of a bacterium in the optical tweezers introduces additional stresses, causing a greater flagellum deformation than we calculated. We think this is not likely because the major energy expenditure is in the rotation of the cell body and the flagellum, which dissipates most of heat ( $\sim 98\%$  of the total power generated by the motor [23]) and is the main cause of the stress. The linear motion of the cell only contribute a small amount in the torque equation via the  $BV$  term. A simple back-of-the-envelope estimate quickly shows that  $|Bv|/|D_0\Omega| \ll 1$  and more precisely for *V. alginolyticus* who swims at  $V = 50 \mu\text{m/s}$ , the ratio is only about two percent. Thus, we conclude that a suppression of the linear motion of the bacterium can only contribute minimally to the flagellum deformation compared to the cell rotation. We note in passing that a detailed calculation based on Takano et al’s work [85] is feasible but it is beyond the scope of this thesis.

### 6.3.2 Precession of flagellum during backward swimming

If flagellum deformation is insufficient to account for the increased rotational load when the motor is CW, an alternative is for the flagellum to precess about its cell body axis as delineated in Figure 6.10(B). Because of a large hydrodynamic resistance for this motion, which is to be analyzed below, even a small precession angular velocity  $\omega_p$  will contribute a non-negligible torque  $\vec{N}_p \cdot \hat{z}$  along the cell body axis, making the body rotate faster than when the flagellum is coaxial with the cell body.

Let’s consider flagellar motion at the instance depicted in Figure 6.10(B). It experiences two rotations, one about its local  $z'$ -axis (self rotation) with an angular velocity  $\omega_b$  and a torque  $\vec{N}_\omega = D_b\omega_b\hat{z}'$ , and the other about the cell-body axis  $\hat{z}$  (precession) with an angular velocity  $\omega_p$  and a torque  $\vec{N}_p = D_p\omega_p\hat{y}'$ , where  $\hat{y}'$  is an instantaneous rotation axis in the

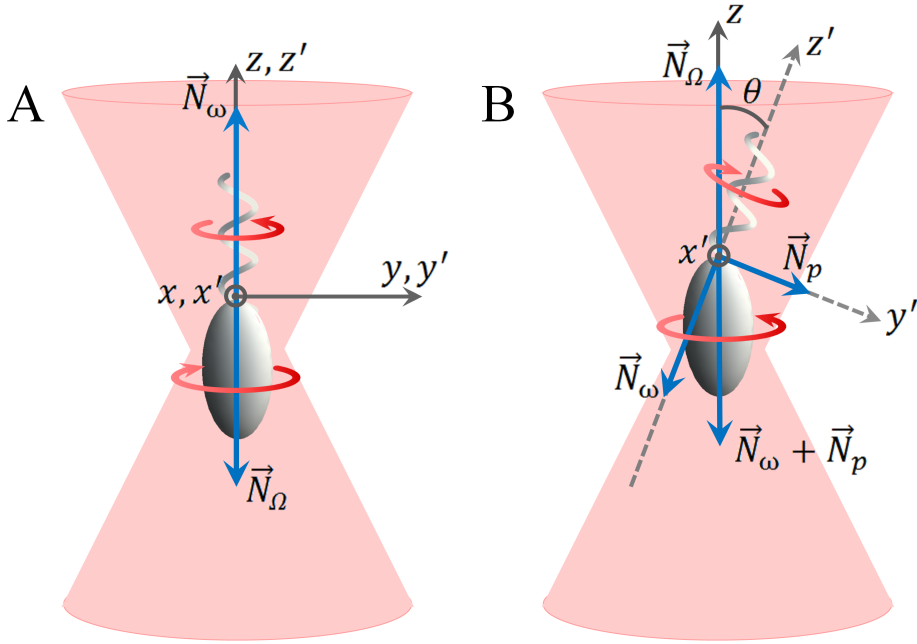


Figure 6.10: States of flagellum rotation in optical trap. The anticorrelation seen our measurements can be quantitatively explained if one assumes that during forward swimming (CCW), the flagellum and the cell body are coaxial as shown in (A) but during backward swimming (CW), the flagellum precesses about the fixed (cell-body)  $z$  axis with a tilting angle  $\theta$  as shown in (B). Since the laser trap is axially symmetric, it cannot exert a torque about the trapping  $z$  axis, and consequently the  $z$ -components of the torque generated by flagellar self rotation  $\vec{N}_\omega$  and the precession torque  $\vec{N}_p$  should sum to zero.

moving coordinates ( $x'$ ,  $y'$ , and  $z'$ ). Calculations in Appendix E show that  $D_p$  is given by

$$D_p = \frac{1}{3}K_n L^3 \alpha^2 \left(1 - \frac{1}{2}(1 - \gamma_k)(1 - \alpha^2)\right). \quad (6.12)$$

We note that since  $D_p$  scales with the flagellum length  $L$  as  $L^3$  whereas  $D_b$  scales as  $LR^2$ , the ratio  $D_b/D_p \propto (R/L)^2 \sim 10^{-3}$  is very small. In other words the precession angular velocity must be correspondingly small to produce a torque comparable to that due to flagellar self rotation. For the precession angle  $\theta$ , one can write the torque balance as,

$$D_0\Omega_b = N_\omega \cos \theta + N_p \sin \theta, \quad (6.13)$$

$$N_p \cos \theta = N_\omega \sin \theta + N_{ext}, \quad (6.14)$$

where  $N_{ext}$  is the torque due to the optical trap. In the above equations, there are three unknowns,  $N_p$ ,  $N_{ext}$ , and  $\theta$  and therefore we can solve  $\theta$  and  $N_p$  in terms of  $N_{ext}$ . A straight forward calculation shows,

$$\cos(\theta + \theta_0) = \frac{N_\omega}{\sqrt{(D_0\Omega_b)^2 + N_{ext}^2}} \quad (6.15)$$

$$N_p = D_0\Omega_b \sin \theta + N_{ext} \cos \theta \quad (6.16)$$

where  $\theta_0 = \cos^{-1} \left( D_0\Omega_b / \sqrt{(D_0\Omega_b)^2 + N_{ext}^2} \right)$ . For the given torque produced by the laser trap  $N_{ext}$ ,  $\theta_0$  can be evaluated and so is the precession angle  $\theta$ . Using  $N_{ext}$  and  $\theta$ , Eq. 6.16 yields the torque that drives the precession of the flagellum.

In order to evaluate Eqs. 6.15 and 6.16 we need to know  $N_\Omega = D_0\Omega_b$ ,  $N_\omega = D_b\omega_b$ , and  $N_{ext}$ . The torque of cell-body rotation can be readily evaluated using Tables 6.1 and 6.3, yielding  $N_\Omega \simeq 2.87 \text{ pN} \cdot \mu\text{m}$ . To evaluate the torque  $N_\omega$  on the flagellum, we assume that the flagellum is rigid and is coaxial with the cell body in the forward interval ( $D_0\Omega_f = D_f\omega_f$ ), which yields  $N_\omega = (\Omega_f/\omega_f)D_0\omega_b \simeq 2.29 \text{ pN} \cdot \mu\text{m}$ . Finally,  $N_{ext}$  can be evaluated using the experimentally observed rate of change of the cell-body orientation  $\theta$  when the bacterium is trapped by the optical tweezers, i.e.  $N_{ext} = D_0\Delta\theta/\Delta t$ . From the time trace  $x(t) \propto \Delta I_x$  in Figure 2.2(B), we found that a horizontally swimming cell becomes aligned with the

trapping axis ( $\Delta\theta = \pi/2$ ) in about  $\Delta t \simeq 10$  ms. This gives  $N_{ext} \approx 0.86$  pN  $\mu\text{m}$ . It follows from Eqs. 6.15 and 6.16  $\theta \simeq 24^\circ$  and the torque about the instantaneous rotation axis  $\hat{y}'$ ,  $N_p \simeq 1.94$  pN  $\mu\text{m}$ . Using the calculated  $D_p \sim 0.11$  pN  $\mu\text{m s}$  and projecting the rotation onto the cell-body  $\hat{z}$ -axis, we found the precession angular frequency about this axis is  $\sim 3$  Hz, which corresponds to one full rotation in an average backward interval.

This calculation is consistent with our proposed model (see Figure 6.5) that when the bacterium swims forward, the joint at the flagellar base is rigid so that the pair of the torques, one due to the flagellum rotation and one due to the cell-body rotation, is coaxial with a zero net torque. However, when the bacterium swims backward, the joint is no longer rigid and fluctuations, such as thermal noise, can cause the flagellum to tilt and to precess about the cell-body axis. Because the hydrodynamic resistance is significantly larger for precession than for flagellar self rotation about its own axis, the rotational load on the cell body increases, causing the cell body to rotate faster ( $\Omega_b > \Omega_f$ ) but the flagellum to rotate slower ( $\omega_b > \omega_f$ ) than the corresponding forward interval. It remains to be investigated how the bacterial swimming speed and efficiency are affected by the soft joint at the base of the flagellum, in particular why the backward swimming speed is higher than forward as seen in our measurement.

## 6.4 DISCUSSION

The anti-correlation reported here raises an interesting question about the torque-speed relationship in this marine bacterium. For *V. alginolyticus*, this relation has been measured by Kawagishi et al. [42] and Sowa [79] but only for the CCW rotation. The experiment was carried out using a bead assay in which the cell body was fixed to a glass surface, the polar flagellum was sheared off, and a micron-sized bead (poly-L-lysine modified) was attached to the fragmented flagellum. The torque-speed curve has the generic shape as that of *E. coli*, i.e., there exists two different regimes separated by the cross-over flagellum angular velocity  $\omega = \omega_C$ . In the high-load regime,  $\omega < \omega_C$ , the torque is approximately constant but declines slightly with  $\omega$ . In the low-load regime,  $\omega > \omega_C$ , the torque decreases rapidly,

in a linear fashion, with  $\omega$  and reaches the zero torque at a characteristic speed  $\omega_0$ . It was found that the stall-torque  $N_0$  (measured when  $\omega \rightarrow 0$ ), the  $\omega_C$ , and  $\omega_0$  are function of the sodium concentration, and the motor is more powerful as the salt concentration increases. For instance at 50 mM Na, which is comparable to our measurements,  $N_0 \simeq 3800$  pN nm,  $\omega_C/2\pi \simeq 450$  Hz with  $N(\omega_C) \simeq 3500$  pN nm, and  $\omega_0/2\pi \simeq 700$  Hz. A schematic drawing is given in Figure 6.11, where the slopes in the high- and low-load regimes are given respectively by  $g = 2\pi\Delta N/\Delta\omega = 0.67$  and  $14$  pN · nm/Hz. In light of these facts, we wonder what kind of torque-speed curve the cell must have in order to account for the anticorrelation we observed. Can we say something about whether for *V. alginolyticus* there is a unique torque-speed relationship or our measurements demand two such relationships, one for each rotation state?

We noticed that since the torque-speed curve has negative slopes in both high- and low-load regimes, a reduction in the flagellum rotation speed implies a shift to a higher load. This is consistent with our observations when the motor switches from CCW (forward) to CW (backward) direction, which is delineated by the solid green and dashed red lines in the figure. However, it is evident that if *V. alginolyticus* operates in the high-load regime (see the first set of the loading lines to the left), the fractional change in the torque  $\delta N/N = g(\omega_f - \omega_b)/(2\pi N) \simeq 0.7\%$  (using  $N = 3600$  pN · nm), according to Figure 6.11, would be too small as compared to our measured  $\delta N/N = 2(\omega_f - \omega_b)/(\omega_f + \omega_b) \simeq 14\%$ . However, if *V. alginolyticus* operates in the low-load regime (see the second set of the loading lines to the right), the fractional change in the torque is now  $\delta N/N = g(\omega_f - \omega_b)/(2\pi N) \simeq 15\%$ , which is very close to what we have observed. Interestingly, the crossover frequency  $\omega_C$  is very close to our measured  $\omega_b$  and consequently  $\omega_f$  is in the low-load regime. Hence, it is highly likely that for *V. alginolyticus* the torque-speed relation is identical in the forward and backward swimming intervals, which is different from what we know about *E. coli*'s motors. For a bi-directional swimmer, which is capable of performing chemotaxis in both swimming direction, this is reasonable.

Non-axis rotation of the polar flagellum, though appears as an unnecessary oddity of bacterial motion, it may play an important role for the flick movement seen in our earlier experiment [92]. Functionally, a flick in *V. alginolyticus* is like a tumble in *E. coli* and

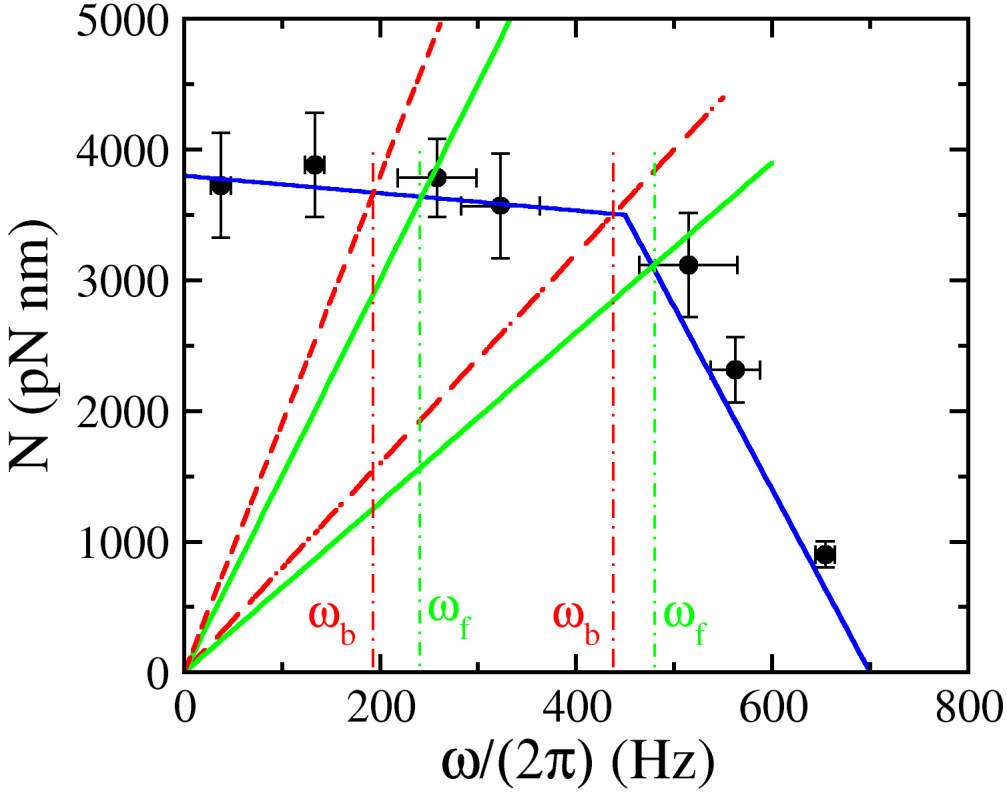


Figure 6.11: Torque-speed relation and motor asymmetry of *V.alginolyticus*' polar flagellar motor. For the CCW rotation, the torque-speed relation has been measured using different sodium salt concentrations [79]. Their data is duplicated above (solid circles) for 50 mM sodium chloride in TMN buffer, which is similar to our measurement. Their measurement displays a high-load and a low-load regime, which are similar to *E. coli*, separated by a corner frequency  $\omega_C/2\pi \simeq 450$  Hz, which is much higher than *E. coli*. The operating points are determined by the intersection between the loading lines, green for the forward and red for the backward swimming, and the torque-speed curve (blue lines). Note in our experiment, the average change in the motor frequency is  $(\omega_f - \omega_b)/2\pi \simeq 40$  Hz, which according to Sowa et al.' measurement will produce a very small change in the torque if the motor is operated in the high-load regime. However, if the motor operates in the low-load regime, the change in torque is comparable to what we observed in our experiment. Interestingly, the motor frequency in the backward interval,  $\omega_b/2\pi$ , turns out to be close to  $\omega_C/2\pi$  as delineated in the figure, the second set of loading lines to the right.

therefore is an important phenotype for efficient chemotaxis. Mechanistically, the precession generates a kink at the base of the flagellum. Upon switching to the forward direction this kink can be amplified since the bacterial body is now being pushed off-axis. If our proposed soft-joint model is correct, the CCW motor rotation tightens the joint, making it more stiff. This causes the re-alignment of the flagellum and the cell-body axis, which signals the end of a flick and the beginning of a new forward run interval. Unlike a tumble in *E. coli*, a flick in *V. alginolyticus* is brief lasting no more than 70 ms based on our early measurement [92].

## APPENDIX A

### MATERIALS AND METHODS

#### A.1 BACTERIAL STRAINS AND CULTURE CONDITIONS

The bacterial strain *V. alginolyticus* YM4 (Pof<sup>+</sup>, Laf<sup>-</sup>) was a kind gift of Michio Homma. The cells were grown overnight in 2 ml of VC (0.5% polypeptone, 0.5% yeast extract, 0.4% K<sub>2</sub>HPO<sub>4</sub>, 3.0% NaCl, 0.2% glucose) at 30 °C with shaking at 200 rpm. The overnight culture was then diluted 1 : 100 in VPG (1.0% polypeptone, 0.4% K<sub>2</sub>HPO<sub>4</sub>, 3.0% NaCl, 0.5% glycerol) and incubated for 3 – 4 hrs at 30 °C with shaking at 200 rpm. For chemotaxis studies, the cells were washed twice in TMN motility buffer (50 mM Tris-HCl (pH 7.5), 5 mM MgCl<sub>2</sub>, 5 mM glucose, 30 mM NaCl, 250 mM KCl) by gentle centrifugation (900 *g*, 2 mins) and resuspended in fresh TMN. They were incubated at 25 °C with shaking at 200 rpm for at least 8 hrs before measurements. We found that the last stage of the preparation, i.e., gentle washing and a long incubation time, is essential for obtaining highly motile bacteria. For optical trapping, the bacteria were diluted 1:100 to avoid multiple cells being captured during a measurement.

#### A.2 OPTICAL TRAP AND MEASUREMENT PROCEDURES

The optical trap was formed by focusing an IR laser (1064 nm, ~ 50 mW at the laser output; Suwtech, LDC-2500) into an open-top chamber with a 100× oil immersion objective (see

Figure 2.2(A)). To avoid hydrodynamic interactions with boundaries, the cells were trapped at  $100\ \mu\text{m}$  above the bottom surface of the chamber. At this large distance a bacterium is always trapped with its cell body along the optical axis of the trap as depicted in Figure 2.2(C-F). The scattered light from the trapped bacterium was collected by a high numerical aperture (N.A. = 1.25) condenser and projected on a silicon position-sensitive detector (PSD) (Pacific Silicon Sensor, DL100-7PCBA). The position of the trapped bacterium was monitored by a PC equipped with an analog-digital converter (National Instruments, AT-MIO-16E-2) and digitized at 10 kHz with a 12-bit resolution. Also incorporated in this setup is a CCD camera (MTI, CCD72), which allows us to visualize bacteria in the sample chamber. As reported earlier [23], this optical trap-microscope setup allows the cell-body  $\Omega$  and the flagellar  $\omega$  rotation speeds to be independently measured for individual bacteria.

To stimulate a trapped cell, a micropipette was mounted on an x-y stage that holds the sample chamber. In this way, the micropipette can move together with the chamber while the optical trap remains fixed in space. The simultaneous movement of the sample chamber and the micropipette relative to the trap is crucial, because in this way the chemoattractant profile remains unperturbed. The x-y movements were controlled by DC actuators (Newport, 850A) whereas the z movement was controlled by a piezo-actuator (Physik Instrumente, P.841.60). Both the x-y and the z actuators are interfaced to the PC via the data acquisition board (National Instruments, AT-MIO-16E-2). The computer controlled x-y and z movements make it possible to automate our measurements, which will be discussed below.

When a bacterium swims far from a boundary, its body wobbles around the swimming axis and can be readily seen by optical microscopy. Such a wobbly motion can be a result of a slight asymmetry between the flagellum and the cell body axes or the length of the cell body being not an integer multiple of the half wavelength that the cell body undulates because of flagellum rotation. This wiggly motion manifests itself in the optical trap as well and allows us to simultaneously determine the cell-body and the flagellum rotation angular frequencies,  $\Omega$  and  $\omega$ , as a function of time  $t$  as delineated in Figure 2.3 [23]. However, for a highly symmetric cell, the  $x(t)$  and  $y(t)$  signals in the detector become small, making a motor reversal hard to detect. To make our measurement reliable, the trap beam was slightly tilted,  $\sim 3^\circ$ , as depicted in Figure 2.2(G). In this case, a cell trapped in the tail-up position

with its flagellum rotating CCW is stabilized slightly below the beam waist, causing a small shift in its  $x$ -position towards the positive side. Likewise if the flagellum is rotating CW, the cell body will be shifted towards positive  $z$  and its  $x$ -position will be slightly negative. Thus, depending on rotation directions, the cell will be preferentially located in the  $+x_0$  and  $-x_0$  positions in the optical trap, which is seen by the two lobes in Figure 2.3(A) and Figure 2.5(A and B). The transition from one state to the other is rapid with an average transition time of  $\sim 20$  ms. The tilted optical trap significantly improves the detection efficiency of motor reversals.

A drawback of our current setup is that a bacterium can be trapped either in the tail-down (C and E) or tail-up (D and F) configurations as displayed in Figure 2.2. For each of these configurations, the cell can swim forward (C and F) or backward (D and E), leading to four possibilities. Even though one can measure  $\Omega$  and  $\omega$ , (C) and (D) or (E) and (F) are degenerate, i.e., an experimenter cannot tell if the cell is swimming forward or backward. This degeneracy persists even when the optical trap is tilted. As a result of this deficiency, initially, we were only able to measure the bacterial switching rate  $S(t)$  but not the CCW bias  $\Phi(t)$ .

For the time-dependent switching rate measurements, the optical trap was positioned  $3\ \mu\text{m}$  away from the serine-filled micropipette using the computer controlled x-y stage. For an appropriate cell concentration,  $\sim 10^6\ \text{ml}^{-1}$ , the typical waiting time was about 5 minutes before a single *V. alginolyticus* was captured by the optical trap. Too high a cell density increased the chance of trapping multiple cells during a measurement; such events were discarded from our data set. Since timing is important in this measurement, the entire procedure was essentially computer controlled. We found that the optical signal detected by the PSD is quiescent when no bacterium is present in the trap. However, when a bacterium is captured, the signal  $\Delta I_x(t)$  and  $\Delta I_y(t)$  fluctuates wildly, where  $\Delta I_x(t)$  and  $\Delta I_y(t)$  are proportional to the cell-body displacement  $(x, y)$  with respect to the trapping center. A typical event is registered in a time series depicted in Figure 2.2(B), where we noticed that a swimming cell falls into the trap rapidly within  $\sim 10$  ms, causing a large spike in  $\Delta I_x(t)$ . Once the cell becomes stably trapped,  $\Delta I_x(t)$  fluctuates with a large amplitude and frequency. The red line in Figure 2.2(B) indicates the moment just before the bacterium fell

into the trap. We used the rms value of  $\Delta I_x(t)$  to monitor the status of the optical trap. If the rms value surpasses a pre-determined threshold, the movement of the x-y stage starts and this defines  $t = 0$  in a measurement. In the subsequent episode, the bacterium was forced to move  $180 \mu\text{m}$  against the chemical gradient direction  $(-\vec{\nabla}c)$  in 6 s while the rotation of the flagellar motor was continuously monitored by the PSD. From the bacterium's perspective, it experiences an initial increase (while it is swimming into the trap) and subsequent decrease in chemoattractant concentration (while the stage is being moved relative to the trap). The speed of the movement,  $v = 30 \mu\text{m/s}$ , was close to the swimming speed  $v_{sw} \simeq 45 \mu\text{m/s}$  of the bacterium. One can define a chemical exposure time  $\tau_0 \equiv 2\rho_0/v \simeq 0.4\text{s}$ , where  $\rho_0$  is the characteristic width of the concentration profile. For each serine concentration in the micropipette, at least a few hundreds of bacteria were trapped, resulting in several thousand switching events.

To find the cell-body and flagellum angular frequencies,  $\Omega(t)$  and  $\omega(t)$ , a moving time window of 200 ms was used to calculate power spectra from the time trace  $x(t)$  and  $y(t)$ . This time window is comparable to the mean switching time but is long compared to the cell-body rotation period so that the low-frequency of the cell-body motion can be resolved. The power spectrum typically consists of a prominent low frequency component, which is due to the cell body rotation  $\Omega(t)$ , and a prominent high frequency component, which is due to the flagellum rotation  $\omega(t)$ . These two outstanding frequencies are well separated so that there is no ambiguity in assigning cell body and flagellar rotation angular frequencies. Sometimes there are satellite peaks around the prominent ones in the power spectrum. In this case,  $\Omega(t)$  and  $\omega(t)$  were calculated by averaging over the three highest peaks from each channel weighted by their corresponding spectral heights. Figure 5.3(D) displays the rotation angular frequencies of the cell body  $\Omega(t)$  and the flagellum  $\omega(t)$  for the time series given in Figure 5.3(C).

In the measurements we identified individual swimming intervals. Within each swimming interval we determined the rotation direction  $s = (f, b)$  of the flagellar motor and the angular frequencies of the flagellum  $\omega_s(t)$  and the cell body  $\Omega_s(t)$ . From these measurements, dynamically useful information, such as the motor speed  $\Omega_s^M(t) = \Omega_s(t) + \omega_s(t)$ , the motor torque  $N_s(t) = D_0\Omega_s(t)$ , the power generated by the motor  $W_s(t) = N_s(t)\Omega_s^M(t)$ , the

rotational load of the flagellum  $D_s(t) = D_0\Omega_s(t)/\omega_s(t)$  in different swimming intervals  $s$  can be determined for individual cells.

### A.3 CREATION OF A LOCALIZED CHEMICAL GRADIENT

We created a sharp concentration gradient using a micropipette prepared by a microelectrode puller (Narishige, PP-830). The inner diameter of the micropipette is less than  $1\ \mu\text{m}$  so that bacteria cannot accumulate inside the capillary. The micropipette was filled with serine of concentration  $c_0$  up to a level beyond which a capillary effect vanishes. A small hydrostatic pressure was applied via a plastic tubing by a water column of height  $H$  as illustrated in Figure 2.2. To calibrate the serine profile, fluorescein dye at 10 mM concentration was used, and the fluorescence intensity profile was measured using an electron-multiplying CCD camera (Hamamatsu, C9100-12) and analyzed by SimplePCI (Compix Inc.). We found that for a given  $H$ , the concentration profile can be established almost instantaneously, in less than 1 s, and it is stable over a long period of time, indicating that a quasi-steady state has been reached.

### A.4 TRACKING OF FREE-SWIMMING CELLS

For comparison with the steady-state measurements in the optical trap, we also collected switching statistics of free-swimming cells. The bacterial swimming trajectories were observed under an inverted microscope (Nikon, TE300) with a 20x objective. The cells were confined between two glass coverslips with a spacing  $\sim 100\ \mu\text{m}$ . Video images were captured at 30 fps by the CCD camera, and the images were analyzed using ImageJ (National Institutes of Health). The mean forward  $t_f$  and backward  $t_b$  swimming times were measured using an ensemble of 61 cells, totaling 617 switching events. This yields the mean switching rate  $S_0 = 2/(t_f + t_b) \simeq 3.25 \pm 0.03\ \text{s}^{-1}$ , which is consistent with the observation made in the optical trap.

## A.5 VIDEO IMAGING OF STUCK CELLS

Swimming bacteria were placed in an open chamber with the bottom surface made of a thin glass coverslip. Over time, some bacteria became stuck to the surface. Most of the stuck cells laid horizontally on the glass surface and were motionless. However, in rare occasions one can find cells that move erratically by protruding and then contracting their cell bodies from the same fixed point. These motions are quite unusual since we never found such a case in stuck *E. coli* cells. In Chapter 6 we will call those that exhibit erratic motions tethered cells.

Our observation showed that most of the tethered cells are close to the other stuck cells, indicating that flagellar entanglement between different cells may be a major cause of tethering and immobilization. However, isolated tethered cells can also be found on the glass coverslip and they also exhibit projection and contraction on the glass surface.

Motion of the tethered cells was captured by a video card in a PC computer and were manually tracked using the centering correction option of ImageJ, which is set to find the local minimum in a 10 pixels x 10 pixels box.

## APPENDIX B

### CALCULATION OF THE MEAN DISPLACEMENT

In the following we provide a more detailed derivation of the mean displacement  $\bar{x}_i = \bar{x}_{fi} + \bar{x}_{bi}$  in a single 3-step cycle. The displacement is made in the two time intervals,  $\Delta_f$  and  $\Delta_b$ , and is represented by Eq. 4.5. The concentration sensed by the bacterium is piecewise continuous according to Figure 4.2 and is given by,

$$c(t) = \begin{cases} c_0 + \nabla c v'_{bi} t, & t < 0 \\ c_0 + \nabla c v_{fi} t, & 0 \leq t < \Delta_f \\ c_0 + \nabla c v_{fi} \Delta_f + \nabla c v_{bi} (t - \Delta_f), & \Delta_f \leq t < \Delta_f + \Delta_b \end{cases}$$

where the subscript  $i$  designates the component of the velocity along the gradient direction. The primed and unprimed velocities correspond to  $t < 0$  (regime I') and  $t \geq 0$  (regimes I and II), respectively.

The first part of Eq. 4.5 is readily calculated by integration by parts,

$$\bar{x}_{fi} \equiv \left\langle \int_0^\infty d\Delta_f \left( -\frac{\partial P_f(\Delta_f)}{\partial \Delta_f} \right) v_{fi} \Delta_f \right\rangle = \left\langle \int_0^\infty d\Delta_f P_f(\Delta_f) v_{fi} \right\rangle \quad (\text{B.1})$$

where  $P_f(\Delta_f)$  is given by Eq. 4.3, which contains an integration in time  $t$  over the range:  $-\theta \leq t \leq \Delta_f - \theta$ . Since  $\Delta_f$  varies from 0 to  $\infty$ , we have to distinguish two cases in the

integration: (i)  $\Delta_f - \theta < 0$  and (ii)  $\Delta_f - \theta > 0$ . One can deal with these two mutually exclusive cases by the use of Heaviside functions  $H(x)$ , i.e., we write,

$$\int_0^\infty d\Delta_f(\dots) \equiv \int_0^\infty d\Delta_f [H(\theta - \Delta_f) + H(\Delta_f - \theta)](\dots). \quad (\text{B.2})$$

The first Heaviside function confines the integral to  $t < 0$ , and since  $\langle v'_{bi} v_{fi} \rangle = 0$ , there is no contribution from this term. The integration constrained by the second Heaviside function yields,

$$\bar{x}_{fi} = \alpha_f \nabla c \langle v_{fi}^2 \rangle \tau_f^2 \exp\left(-\frac{\theta}{\tau_f}\right). \quad (\text{B.3})$$

This equation is identical to that found by de Gennes when he calculated the drift velocity for *E. coli* cells [29].

The second part of Eq. 4.5 is more complicated because one has to take into account more possibilities. Again, we used integration by parts to obtain,

$$\begin{aligned} \bar{x}_{bi} &\equiv \left\langle \int_0^\infty d\Delta_f \int_0^\infty d\Delta_b \left( -\frac{\partial P_f(\Delta_f)}{\partial \Delta_f} \right) \left( -\frac{\partial P_b(\Delta_b, \Delta_f)}{\partial \Delta_b} \right) v_{bi} \Delta_b \right\rangle \\ &= \left\langle P_f(0) \int_0^\infty d\Delta_b P_b(\Delta_b, 0) v_{bi} \right\rangle + \left\langle \int_0^\infty d\Delta_f \int_0^\infty d\Delta_b P_f(\Delta_f) \frac{\partial P_b(\Delta_b, \Delta_f)}{\partial \Delta_f} v_{bi} \right\rangle. \end{aligned} \quad (\text{B.4})$$

Let the first term in the above equation be  $\bar{x}_{bi}^{(bb)}$  and the second term be  $\bar{x}_{bi}^{(bf)}$ . Since  $P_f(0) = 1$  and  $P_b(\Delta_b, 0) = P_f(\Delta_b)$ , it follows that the integration in the first term is identical to Eq. B.1 with the replacement of the subscript  $f$  by  $b$ . This yields,

$$\bar{x}_{bi}^{(bb)} = \alpha_b \nabla c \langle v_{bi}^2 \rangle \tau_b^2 \exp\left(-\frac{\theta}{\tau_b}\right). \quad (\text{B.5})$$

Now, let's examine the anti-correlation term  $\bar{x}_{bi}^{(bf)}$ , which corresponds to the situation when the bacterium swims down the gradient but it still keeps its ‘‘old good memory’’. Dropping the nonlinear terms in concentration  $c$ , we found,

$$\bar{x}_{bi}^{(bf)} = \frac{\alpha_b}{\tau_b} \left\langle \int_0^\infty d\Delta_f \int_0^\infty d\Delta_b \exp\left(-\frac{\Delta_f}{\tau_f}\right) \exp\left(-\frac{\Delta_b}{\tau_b}\right) \frac{\partial}{\partial \Delta_f} \int_{\Delta_f - \theta}^{\Delta_f + \Delta_b - \theta} dt c(t) v_{bi} \right\rangle. \quad (\text{B.6})$$

When integrating over  $\Delta_f$ , there are two possibilities for the lower limit of the  $t$ -integration, i.e. either  $\Delta_f - \theta < 0$  or  $\Delta_f - \theta \geq 0$ . These will be delimited by the Heaviside functions as before. For each of these cases, while integrating over  $\Delta_b$ , there are additional possibilities for the upper limit of the  $t$ -integration. For the first case, when  $\Delta_f - \theta < 0$ , there are three possibilities: (i)  $\Delta_f - \theta \leq \Delta_f + \Delta_b - \theta \leq 0$ , (ii)  $0 \leq \Delta_f + \Delta_b - \theta \leq \Delta_f$ , and (iii)  $\Delta_f \leq \Delta_f + \Delta_b - \theta \leq \Delta_f + \Delta_b$ , corresponding to the regimes I', I, and II in Figure 4.2, respectively. However, since motion is uncorrelated after a flick or  $\langle v'_{bi} v_{bi} \rangle = 0$ , the first possibility does not contribute to the displacement. In the second case, when  $\Delta_f - \theta \geq 0$ , there are two additional possibilities: (iv)  $\Delta_f - \theta \leq \Delta_f + \Delta_b - \theta \leq \Delta_f$  and (v)  $\Delta_f \leq \Delta_f + \Delta_b - \theta \leq \Delta_f + \Delta_b$ , corresponding to the regimes I and II in Figure 4.2, respectively. The corresponding time integrals for the above four possibilities (ii-v) are given by

$$\int_{\Delta_f - \theta}^{\Delta_f + \Delta_b - \theta} dt c(t) = \begin{cases} c_0 (\Delta_f + \Delta_b - \theta) + \frac{1}{2} \nabla c v_{fi} (\Delta_f + \Delta_b - \theta)^2, & (ii) \\ c_0 \Delta_f + \frac{1}{2} \nabla c v_{fi} \Delta_f^2 + c_1 (\Delta_b - \theta) \\ \quad + \frac{1}{2} \nabla c v_{bi} (\Delta_b - \theta)^2, & (iii) \\ c_0 \Delta_b + \nabla c v_{fi} \Delta_b (\Delta_f + \frac{1}{2} \Delta_b - \theta), & (iv) \\ c_0 \theta + \nabla c v_{fi} \theta (\Delta_f - \frac{\theta}{2}) + c_1 (\Delta_b - \theta) \\ \quad + \frac{1}{2} \nabla c v_{bi} (\Delta_b - \theta)^2, & (v) \end{cases} \quad (\text{B.7})$$

where  $c_1 \equiv c_0 + \nabla c v_{fi} \Delta_f$ . Using the above expressions, we take the derivative with respect to  $\Delta_f$  to obtain,

$$\frac{\partial}{\partial \Delta_f} \int_{\Delta_f - \theta}^{\Delta_f + \Delta_b - \theta} dt c(t) = \begin{cases} c_0 + \nabla c v_{fi} (\Delta_f + \Delta_b - \theta), & (ii) \\ c_0 + \nabla c v_{fi} (\Delta_f + \Delta_b - \theta), & (iii) \\ \nabla c v_{fi} \Delta_b, & (iv) \\ \nabla c v_{fi} \Delta_b. & (v) \end{cases} \quad (\text{B.8})$$

Again, using the Heaviside functions to represent these four non-trivial possibilities, we have the following identity

$$\begin{aligned} \int_0^\infty d\Delta_f \int_0^\infty d\Delta_b(\dots) &= \int_0^\infty d\Delta_f \int_0^\infty d\Delta_b \\ &\quad \{H(\theta - \Delta_f) [H(\Delta_f + \Delta_b - \theta)H(\theta - \Delta_b) + H(\Delta_b - \theta)H(\theta)] \\ &\quad + H(\Delta_f - \theta) [H(\Delta_b)H(\theta - \Delta_b) + H(\Delta_b - \theta)H(\theta)]\} (\dots). \end{aligned} \quad (\text{B.9})$$

Substituting this equation into Eq. B.6, we found,

$$\begin{aligned} \bar{x}_{bi}^{(bf)} &= \frac{\alpha_b}{\tau_b} \left\langle \int_0^\infty d\Delta_f \int_0^\infty d\Delta_b \exp\left(-\frac{\Delta_f}{\tau_f}\right) \exp\left(-\frac{\Delta_b}{\tau_b}\right) \right. \\ &\quad \times \{H(\theta - \Delta_f) [H(\Delta_f + \Delta_b - \theta)H(\theta - \Delta_b)(ii) + H(\Delta_b - \theta)H(\theta)(iii)] \\ &\quad \left. + H(\Delta_f - \theta) [H(\Delta_b)H(\theta - \Delta_b)(iv) + H(\Delta_b - \theta)H(\theta)(v)]\} v_{bi} \right\rangle, \end{aligned} \quad (\text{B.10})$$

where (ii), (iii), (iv), and (v) are the terms given in Eq. B.8. The four integrations in the above equation are delimited by different combinations of Heaviside functions, yielding different lower and upper integration limits for each integral. Designating these integrals as  $\left(\bar{x}_{bi}^{(bf)}\right)_{ii}$ ,  $\left(\bar{x}_{bi}^{(bf)}\right)_{iii}$ ,  $\left(\bar{x}_{bi}^{(bf)}\right)_{iv}$ , and  $\left(\bar{x}_{bi}^{(bf)}\right)_v$ , we found,

$$\begin{aligned} \left(\bar{x}_{bi}^{(bf)}\right)_{ii} &= \frac{\alpha_b}{\tau_b} \nabla c \langle v_{fi} v_{bi} \rangle \int_0^\theta d\Delta_f \int_{\theta - \Delta_f}^\theta d\Delta_b \exp\left(-\frac{\Delta_f}{\tau_f}\right) \exp\left(-\frac{\Delta_b}{\tau_b}\right) (\Delta_f + \Delta_b - \theta) \\ &= \alpha_b \nabla c \langle v_{fi} v_{bi} \rangle \frac{\tau_f}{\tau_f - \tau_b} \exp\left[-\theta \left(\frac{1}{\tau_b} + \frac{1}{\tau_f}\right)\right] \\ &\quad \times \left\{ \tau_b^2 \left[ \exp\left(\frac{\theta}{\tau_b}\right) - 1 \right] - \tau_f^2 \left[ \exp\left(\frac{\theta}{\tau_f}\right) - 1 \right] + \theta(\tau_f - \tau_b) \right\}, \end{aligned} \quad (\text{B.11})$$

$$\begin{aligned} \left(\bar{x}_{bi}^{(bf)}\right)_{iii} &= \frac{\alpha_b}{\tau_b} \nabla c \langle v_{fi} v_{bi} \rangle \int_0^\theta d\Delta_f \int_\theta^\infty d\Delta_b \exp\left(-\frac{\Delta_f}{\tau_f}\right) \exp\left(-\frac{\Delta_b}{\tau_b}\right) (\Delta_f + \Delta_b - \theta) \\ &= \alpha_b \nabla c \langle v_{fi} v_{bi} \rangle \tau_f \left[ \tau_f + \tau_b - (\tau_f + \tau_b + \theta) \exp\left(-\frac{\theta}{\tau_f}\right) \right] \exp\left(-\frac{\theta}{\tau_b}\right), \end{aligned} \quad (\text{B.12})$$

$$\begin{aligned}
\left(\bar{x}_{bi}^{(bf)}\right)_{iv} &= \frac{\alpha_b}{\tau_b} \nabla c \langle v_{fi} v_{bi} \rangle \int_{\theta}^{\infty} d\Delta_f \int_0^{\theta} d\Delta_b \exp\left(-\frac{\Delta_f}{\tau_f}\right) \exp\left(-\frac{\Delta_b}{\tau_b}\right) \Delta_b \\
&= \alpha_b \nabla c \langle v_{fi} v_{bi} \rangle \tau_f \left[ \tau_b - (\theta + \tau_b) \exp\left(-\frac{\theta}{\tau_b}\right) \right] \exp\left(-\frac{\theta}{\tau_f}\right), \quad (\text{B.13})
\end{aligned}$$

$$\begin{aligned}
\left(\bar{x}_{bi}^{(bf)}\right)_v &= \frac{\alpha_b}{\tau_b} \nabla c \langle v_{fi} v_{bi} \rangle \int_{\theta}^{\infty} d\Delta_f \int_{\theta}^{\infty} d\Delta_b \exp\left(-\frac{\Delta_f}{\tau_f}\right) \exp\left(-\frac{\Delta_b}{\tau_b}\right) \Delta_b \\
&= \alpha_b \nabla c \langle v_{fi} v_{bi} \rangle \tau_f (\tau_b + \theta) \exp\left(-\frac{\theta}{\tau_f}\right) \exp\left(-\frac{\theta}{\tau_b}\right). \quad (\text{B.14})
\end{aligned}$$

In the above calculation, the terms involving  $c_0$  do not contribute since  $\langle v_{bi} \rangle = 0$ . The anti-correlation term due to all the above contributions is then given by,

$$\begin{aligned}
\bar{x}_{bi}^{(bf)} &= \left(\bar{x}_{bi}^{(bf)}\right)_{ii} + \left(\bar{x}_{bi}^{(bf)}\right)_{iii} + \left(\bar{x}_{bi}^{(bf)}\right)_{iv} + \left(\bar{x}_{bi}^{(bf)}\right)_v \\
&= \alpha_b \nabla c \langle v_{fi} v_{bi} \rangle \frac{\tau_f^2 \tau_b^2}{\tau_b - \tau_f} \left[ \frac{1}{\tau_f} \exp\left(-\frac{\theta}{\tau_b}\right) - \frac{1}{\tau_b} \exp\left(-\frac{\theta}{\tau_f}\right) \right]. \quad (\text{B.15})
\end{aligned}$$

Combining Eqs. B.3, B.5, and B.15, we finally obtain the mean displacement in a given cycle for the 3-step swimmer,

$$\begin{aligned}
\bar{x}_i &= \alpha_f \nabla c \langle v_{fi}^2 \rangle \tau_f^2 \exp\left(-\frac{\theta}{\tau_f}\right) + \alpha_b \nabla c \langle v_{bi}^2 \rangle \tau_b^2 \exp\left(-\frac{\theta}{\tau_b}\right) \\
&\quad + \alpha_b \nabla c \langle v_{fi} v_{bi} \rangle \frac{\tau_f^2 \tau_b^2}{\tau_b - \tau_f} \left[ \frac{1}{\tau_f} \exp\left(-\frac{\theta}{\tau_b}\right) - \frac{1}{\tau_b} \exp\left(-\frac{\theta}{\tau_f}\right) \right]. \quad (\text{B.16})
\end{aligned}$$

## APPENDIX C

### OPTIMIZATION OF THE DRIFT VELOCITY

For the first chemotactic strategy,  $R_f(t)$  and  $R_b(t)$  in Eq. 4.9 are independently optimized. The procedure requires to constrain a family of response functions  $R_s(t)$ , where  $s = f, b$ . We followed Clark and Grant's approach [27] and assumed that  $R_s(t)$  is finite, continuous, and decays to zero for large  $t$ . The simplest way to impose the constraint is to assume a finite variance

$$\int_0^{\infty} R_s^2(t) dt = \sigma_s^2 / \tau_s \quad (\text{C.1})$$

that is to be satisfied by all curves in the family. Optimizing  $\kappa (= V/\nabla c)$ , which is given by Eq. 4.9, with the above constraint is equivalent to

$$\frac{\delta}{\delta R_s(t)} \int_0^{\infty} dt \left[ R_s(t) K_s(t) - \lambda \left( R_s^2(t) - \frac{\sigma_s^2}{\tau_s} \right) \right] = 0 \quad (\text{C.2})$$

where  $K_s(t)$  is the kernel that weights the forward ( $s = f$ ) and the backward ( $s = b$ ) response functions,

$$K_f(t) = \exp\left(-\frac{t}{\tau_f}\right), \quad (\text{C.3})$$

$$K_b(t) = \exp\left(-\frac{\theta}{\tau_b}\right) - \frac{\tau_f^2}{\tau_f - \tau_b} \left( \frac{1}{\tau_b} \exp\left(-\frac{\theta}{\tau_b}\right) - \frac{1}{\tau_f} \exp\left(-\frac{\theta}{\tau_b}\right) \right). \quad (\text{C.4})$$

Aside from normalization constants, the optimized response functions are given in Eqs. 4.10 and 4.11.

A similar procedure can also be applied to the second chemotactic strategy, resulting in the optimized response function given by Eq. 4.13.

## APPENDIX D

### WHAT DO WE KNOW ABOUT FLAGELLAR MOTOR SWITCHES?

Khan and Macnab initiated this line of research, and some of their original findings were delineated in the main text [45]. However, recent detailed studies, at least for *E. coli*, the physical picture is different. Specifically, in recent studies by the Howard Berg group at Harvard, a number of physical effects would show to cause a rotation bias other than pH alone. It was found that in the absence of chemotaxis regulator protein CheY-P, the motor is exclusively in the CCW direction at room temperature. However, motor reversal can be induced in this cheY-P deficient *E. coli* strain simply by reducing temperature below 10 °C and at −2 °C the motor is exclusively in the CW direction [87]. Fahrner et al. [32] discovered that a hydrodynamic load also has a strong influence on the motor bias, similar to the action of fumarate [68]. Specifically, in the high-load regime (normal swimming), the motor has a strong CCW bias, however, when the load increases so that the motor speed decreases (to  $\omega < 50$  Hz), the CW bias increases significantly [32]. Aside from the bias, the switching rate is also altered [94, 95]. In the high-load regime, the motor switching frequency decreases with the load but in the low-load regime, the motor switching frequency increases. These observations together suggest that the motor switch, aside from being regulated by CheY-P, also senses the load or proton ion fluxes. However, since in the high-load regime, the torque changes only about 5% in the speed range  $0 < \omega < 50$  Hz, it was conjectured that the ion flux may be the main cause of the effect. (Note this conclusion is based on the Meister, Lowe, Berg's observation in 1987 when they found that the number of ions flowing through the motor per revolution is approximately constant [62].) However, if this latter finding is

contradictory to the pH measurement of Khan and Macnab [\[45\]](#).

## APPENDIX E

### FORCE AND TORQUE DUE TO TILTING OF THE BACTERIAL FLAGELLUM

We assume that in the lab coordinates  $(x, y, z)$  the cell body is along the  $z$ -axis, and the misaligned flagellum rotates about the  $z$ -axis with a constant angular velocity  $\omega_p$  at an angle  $\theta$  as shown in Figure 6.10(B). We define a fixed local coordinate system  $(x', y', z')$  such that the  $z'$ -axis coincides with the tilted flagellar axis. At the instance of consideration, let the  $x'$ -axis be parallel to the  $x$ -axis. In this local moving coordinate system the flagellum can be parametrized as

$$\vec{h}(s) = \left( R \cos(Ks + \phi), R \sin(Ks + \phi), \sqrt{1 - K^2 R^2} s \right), \quad (\text{E.1})$$

where  $R$  is the radius of the helix,  $K = 2\pi/\Lambda$  is the wavenumber measured along the contour with wavelength  $\Lambda$ ,  $s$  is the contour length along the flagellum, and  $\phi$  is a random phase which will be averaged over  $2\pi$  at the end of calculation. Note also the pitch  $\lambda$  along  $z$  axis and along  $s$  are related by the directional cosine,  $\cos \Psi = \alpha = \sqrt{1 - R^2 K^2} = \lambda/\Lambda$ . The tangential unit vector  $\hat{t}$  of  $\vec{h}(s)$  is,

$$\hat{t}(s) = \left( -RK \sin(Ks + \phi), RK \cos(Ks + \phi), \sqrt{1 - K^2 R^2} \right). \quad (\text{E.2})$$

We will calculate the torque based on this instantaneous configuration, but the result holds for other angular positions of the flagellum as well. Since we are only interested in precession about  $z$ -axis, there is no need to consider flagellum self rotation about the local  $z'$ -axis. Let

the instantaneous rotation axis being along  $\hat{y}'$  or  $\vec{\omega}_p = \omega_p \hat{y}'$ . The velocity of the flagellar segment located at  $s$  to  $s + ds$  in the local coordinates can be readily calculated as

$$\vec{v}(s) = \vec{\omega}_p \times \vec{h}(s) = \omega_p(\sqrt{1 - K^2 R^2} s, 0, -R \cos(Ks + \phi)). \quad (\text{E.3})$$

One can decompose this velocity into the longitudinal  $v_t$  and the transverse  $v_n$  component with the result,

$$\vec{v}_t(s) = (\vec{v}(s) \cdot \hat{t}(s)) \hat{t}(s), \quad (\text{E.4})$$

$$\vec{v}_n(s) = \vec{v}(s) - \vec{v}_t(s). \quad (\text{E.5})$$

The force density acting on the segment  $ds$  located at  $s$  is then given by  $\vec{f}(s) = K_t \vec{v}_t(s) + K_n \vec{v}_n(s)$ . The total force  $\vec{F}_p$  and the torque  $\vec{N}_p$  can then be calculated by straight forward integration:

$$\vec{F}_p = \frac{1}{2\pi} \int_0^{2\pi} d\phi \int_0^L \vec{f}(s) ds = \frac{1}{2} K_n L \alpha \omega_p \left[ \frac{L}{2} ((1 + \alpha^2) + \gamma_k (1 - \alpha^2)), R \sqrt{1 - \alpha^2} (1 - \gamma_k), 0 \right], \quad (\text{E.6})$$

$$\begin{aligned} \vec{N}_p &= \frac{1}{2\pi} \int_0^{2\pi} \int_0^L \vec{h}(s) \times \vec{f}(s) ds = \frac{1}{3} K_n L^3 \alpha^2 \omega_p \left[ 0, 1 + \frac{1 - \alpha^2}{2\alpha^2} (\gamma_k - 1) \right. \\ &\quad \left. + \frac{3}{2\alpha^2} \left( \frac{R}{L} \right)^2 \gamma_k + \frac{(1 - \alpha^2)}{2\alpha^2} (1 - \gamma_k) \left( \frac{R}{L} \right)^2 \left( 3 + (1 - \alpha^2) \left( \frac{L}{R} \right)^2 \right), 0 \right]. \quad (\text{E.7}) \end{aligned}$$

In the limit of small  $R/L$ , the above expression can be simplified with the result,

$$\vec{N}_p \simeq \frac{1}{3} K_n L^3 \alpha^2 \omega_p \left[ 0, 1 - \frac{1 - \alpha^2}{2} (1 - \gamma_k), 0 \right]. \quad (\text{E.8})$$

Thus, the precession of the flagellum will generate a net force  $\vec{F}_p$  and a torque  $\vec{N}_p$  given above. For free-swimming, all forces and torques should be balanced on a bacterium. When trapped in the optical tweezers, the force  $\vec{F}_{ext}$  and torque  $\vec{N}_{ext}$  generated by the optical trap should also be taken into account.

## BIBLIOGRAPHY

- [1] J. Adler. Chemoreceptors in bacteria. *Science*, 166:1588–1597, 1969.
- [2] R. D. Allen and P. Baumann. Structure and arrangement of flagella in species of the genus *Beneckea* and *Photobacterium fischeri*. *J. Bacteriol.*, 107:295–302, 1971.
- [3] U. Alon, M. G. Surette, N. Barkai, and S. Leibler. Robustness in bacterial chemotaxis. *Nature*, 397:168–171, 1999.
- [4] T. Altindal, S. Chattopadhyay, and X. L. Wu. Bacterial chemotaxis in an optical trap. *PLoS ONE*, 6(4):e18231, 2011.
- [5] T. Altindal and X. L. Wu. On biphasic response of bacterial chemotaxis (unpublished).
- [6] T. Altindal, L. Xie, and X. L. Wu. Implications of three-step swimming patterns in bacterial chemotaxis. *Biophys. J.*, 100:32–41, 2011.
- [7] K. H. Ang, G. Chong, and Y. Li. PID control system analysis, design, and technology. *IEEE Trans. Control Syst. Technol.*, 13:559–576, 2005.
- [8] E. Balkovsky and B. I. Shraiman. Olfactory search at high Reynolds number. *Proc. Natl. Acad. Sci. USA.*, 99:12589–12593, 2002.
- [9] N. Barkai and S. Leibler. Robustness in simple biochemical networks. *Nature*, 387:913–917, 1997.
- [10] H. C. Berg. How to track bacteria. *Rev. Sci. Instrum.*, 42:868–871, 1971.
- [11] H. C. Berg. *Random Walks in Biology*. Princeton University Press, 1. edition, 1993.
- [12] H. C. Berg and R. A. Anderson. Bacteria swim by rotating their flagellar filaments. *Nature*, 245:380–382, 1973.
- [13] H. C. Berg and D. A. Brown. Chemotaxis in *Escherichia coli* analysed by three-dimensional tracking. *Nature*, 239:500–504, 1972.
- [14] H. C. Berg and E. M. Purcell. Physics of chemoreception. *Biophys. J.*, 20:193–219, 1977.

- [15] H. C. Berg and P. M. Tedesco. Transient response to chemotactic stimuli in *Escherichia coli*. *Proc. Natl. Acad. Sci. USA.*, 72:3235–3239, 1975.
- [16] W. Bialek and S. Setayeshgar. Physical limits to biochemical signaling. *Proc. Natl. Acad. Sci. USA*, 102:10040–10045, 2005.
- [17] S. M. Block, D. F. Blair, and H. C. Berg. Compliance of bacterial flagella measured with optical tweezers. *Nature*, 338:514–518, 1989.
- [18] S. M. Block, J. E. Segall, and H. C. Berg. Adaptation kinetics in bacterial chemotaxis. *J. Bacteriol.*, 154:312–323, 1983.
- [19] K. A. Borkovich and M. I. Simon. The dynamics of protein phosphorylation in bacterial chemotaxis. *Cell*, 63:1339–1348, 1990.
- [20] D. Bray, M. D. Levin, and C. J. Morton-Firth. Receptor clustering as a cellular mechanism to control sensitivity. *Nature*, 393:85–88, 1998.
- [21] A. Bren, M. Welch, Y. Blat, and M. Eisenbach. Signal termination in bacterial chemotaxis: CheZ mediates dephosphorylation of free rather than switch-bound CheY. *Proc. Natl. Acad. Sci. USA*, 93:10090–10093, 1996.
- [22] A. Celani and M. Vergassola. Bacterial strategies for chemotaxis response. *Proc. Natl. Acad. Sci. USA*, 107:1391–1396, 2010.
- [23] S. Chattopadhyay, R. Moldovan, C. Yeung, and X. L. Wu. Swimming efficiency of bacterium *Escherichia coli*. *Proc. Natl. Acad. Sci. USA*, 103:13712–13717, 2006.
- [24] S. Chattopadhyay and X. L. Wu. The effect of long-range hydrodynamic interaction on the swimming of a single bacterium. *Biophys. J.*, 96:2023–2028, 2009.
- [25] X. Chen and H. C. Berg. Torque-speed relationship of the flagellar rotary motor of *Escherichia coli*. *Biophys. J.*, 78:1036–1041, 2000.
- [26] F. D. Ciccarelli, T. Doerks, C. von Mering, C. J. Creevey, B. Snel, and P. Bork. Toward automatic reconstruction of a highly resolved tree of life. *Science*, 311:1283–1287, 2006.
- [27] D. A. Clark and L. C. Grant. The bacterial chemotactic response reflects a compromise between transient and steady-state behavior. *Proc. Natl. Acad. Sci. USA*, 102:9150–9155, 2005.
- [28] P. Cluzel, M. Surette, and S. Leibler. An ultrasensitive bacterial motor revealed by monitoring signaling proteins in single cells. *Science*, 287:1652–1655, 2000.
- [29] P. G. de Gennes. Chemotaxis: the role of internal delays. *Eur. Biophys. J.*, 33:691–693, 2004.

- [30] R. G. Endres and N. S. Wingreen. Precise adaptation in bacterial chemotaxis through “assistance neighborhoods”. *Proc. Natl. Acad. Sci. USA*, 103:13040–13044, 2006.
- [31] R. G. Endres and N. S. Wingreen. Accuracy of direct gradient sensing by single cells. *Proc. Natl. Acad. Sci. USA*, 105:15749–15754, 2008.
- [32] K. A. Fahrner, W. S. Ryu, and H. C. Berg. Bacterial flagellar switching under load. *Nature*, 423:938, 2003.
- [33] E. A. C. Follett and J. Gordon. An electron microscope study of *Vibrio* flagella. *J. Gen. Microbiol.*, 32:235–239, 1963.
- [34] R. P. Futrelle and H. C. Berg. Specification of gradients used for studies of chemotaxis. *Nature*, 239:517–518, 1972.
- [35] L. F. Garrity and G. W. Ordal. Chemotaxis in *Bacillus subtilis*: how bacteria monitor environmental signals. *Pharmacol. Ther.*, 68:87–104, 1995.
- [36] J. E. Gestwicki, A. C. Lamanna, R. M. Harshey, L. L. McCarter, L. L. Kiessling, and J. Adler. Evolutionary conservation of methyl-accepting chemotaxis protein location in bacteria and archaea. *J. Bacteriol.*, 182:6499–6502, 2000.
- [37] M. Homma, H. Oota, S. Kojima, I. Kawagishi, and Y. Imae. Chemotactic responses to an attractant and a repellent by the polar and lateral flagellar systems of *Vibrio alginolyticus*. *Microbiol.*, 142:2777–2783, 1996.
- [38] H. Hotani. Micro-video study of moving bacterial flagellar filaments: III. Cyclic transformation induced by mechanical force. *J. Mol. Biol.*, 156:791–806, 1982.
- [39] N. Imai, S. Kudo, and Y. Magariyama. Observation of helical pitch of rotating bacterial flagella. *J. Visualization Society of Japan*, 20:31–32, 2000.
- [40] A. Ishihara, J. E. Segall, S. M. Block, and H. C. Berg. Coordination of flagella on filamentous cells of *Escherichia coli*. *J. Bacteriol.*, 155:228–237, 1983.
- [41] Y. V. Kalinin, L. Jiang, Y. Tu, and M. Wu. Logarithmic sensing in *Escherichia coli* bacterial chemotaxis. *Biophys. J.*, 96:2439–2448, 2009.
- [42] I. Kawagishi, M. Imagawa, Y. Imae, L. McCarter, and M. Homma. The sodium-driven polar flagellar motor of marine *Vibrio* as the mechanosensor that regulates lateral flagellar expression. *Mol. Microbiol.*, 20:693–699, 1996.
- [43] J. E. Keymer, R. G. Endres, M. Skoge, Y. Meir, and N. S. Wingreen. Chemosensing in *Escherichia coli*: Two regimes of two-state receptors. *Proc. Natl. Acad. Sci. USA*, 103:1786–1791, 2006.

- [44] S. Khan, K. Amoyaw, J. L. Spudich, G. P. Reid, and D. R. Trentham. Bacterial chemoreceptor signaling probed by flash photorelease of a caged serine. *Biophys. J.*, 62:67–68, 1992.
- [45] S. Khan and R. M. Macnab. The steady-state counterclockwise/clockwise ratio of bacterial flagellar motors is regulated by protonmotive force. *J. Mol. Biol.*, 138:563–597, 1980.
- [46] C. Kim, M. Jackson, R. Lux, and S. Khan. Determinants of chemotactic signal amplification in *Escherichia coli*. *J. Mol. Biol.*, 307:119–135, 2001.
- [47] M. Kojima, R. Kubo, T. Yakushi, M. Homma, and I. Kawagishi. The bidirectional polar and unidirectional lateral flagellar motors of *Vibrio alginolyticus* are controlled by a single CheY species. *Mol. Microbiol.*, 64:57–67, 2007.
- [48] E. Korobkova, T. Emonet, J. M. G. Vilar, T. S. Shimizu, and P. Cluzel. From molecular noise to behavioural variability in a single bacterium. *Nature*, 428:574–578, 2004.
- [49] D. E. Koshland, Jr. Bacterial chemotaxis in relation to neurobiology. *Annu. Rev. Neurosci.*, 3:43–75, 1980.
- [50] L. D. Landau and E. M. Lifshitz. *Fluid Mechanics*. Tarrytown: Pergamon Press. 539 p, 1982.
- [51] M. N. Levit and J. B. Stock. Receptor methylation controls the magnitude of stimulus-response coupling in bacterial chemotaxis. *J. Biol. Chem.*, 277:36760–36765, 2002.
- [52] J. Lighthill. Flagellar hydrodynamics: the john von neumann lecture, 1975. *SIAM Rev.*, 18:161–230, 1976.
- [53] R. Macnab and D. E. Koshland, Jr. The gradient-sensing mechanism in bacterial chemotaxis. *Proc. Natl. Acad. Sci. USA*, 69:2509–2512, 1972.
- [54] R. M. Macnab and M. K. Ornston. Normal-to-curly flagellar transitions and their role in bacterial tumbling. Stabilization of an alternative quaternary structure by mechanical force. *J. Mol. Biol.*, 112:1–30, 1977.
- [55] J. R. Maddock and L. Shapiro. Polar location of the chemoreceptor complex in the *Escherichia coli* cell. *Science*, 259:1717–1723, 1993.
- [56] Y. Magariyama, S. Masuda, Y. Takano, T. Ohtani, and S. Kudo. Difference between forward and backward swimming speeds of the single polar-flagellated bacterium, *Vibrio alginolyticus*. *FEMS Microbiol. Lett.*, 205:343–347, 2001.
- [57] Y. Magariyama, S. Sugiyama, K. Muramoto, I. Kawagishi, Y. Imae, and S. Kudo. Simultaneous measurement of bacterial flagellar rotation rate and swimming speed. *Biophys. J.*, 69:2154–2162, 1995.

- [58] Y. Magariyama, S. Sugiyama, K. Muramoto, Y. Maekawa, I. Kawagishi, Y. Imae, and S. Kudo. Very fast flagellar rotation. *Nature*, 371:752, 1994.
- [59] N. Maki, J. E. Gestwicki, E. M. Lake, L. L. Kiessling, and J. Adler. Motility and chemotaxis of filamentous cells of *Escherichia coli*. *J. Bacteriol.*, 182:4337–4342, 2000.
- [60] H. B. Mao, P. S. Cremer, and M. D. Manson. A sensitive, versatile microfluidic assay for bacterial chemotaxis. *Proc. Natl. Acad. Sci. USA*, 100:5449–5454, 2003.
- [61] L. L. McCarter. Polar flagellar motility of the *Vibrionaceae*. *Microbiol. Mol. Biol. Rev.*, 65:445–462, 2001.
- [62] M. Meister, G. Lowe, and H. C. Berg. The proton flux through the bacterial flagellar motor. *Cell*, 49:643–650, 1987.
- [63] B. A. Mello and Y. Tu. An allosteric model for heterogeneous receptor complexes: Understanding bacterial chemotaxis responses to multiple stimuli. *Proc. Natl. Acad. Sci. USA*, 102:17354–17359, 2005.
- [64] R. Mesibov, G. W. Ordal, and J. Adler. The range of attractant concentrations for bacterial chemotaxis and the threshold and size of response over this range. *J. Gen. Physiol.*, 62:203–223, 1973.
- [65] J. G. Mitchell. The influence of cell size on marine bacterial motility and energetics. *Microb. Ecol.*, 22:227–238, 1991.
- [66] M. Nishitoba, N. Imai, Y. Magariyama, and S. Kudo. Observation of bacterial flagellar deformation with laser dark-field microscope. *47th Spring Meeting of Japan Soc. Appl. Phys. and Related Soc. (in Japanese)*, 30a-D-5, 2000.
- [67] S. L. Porter, G. H. Wadhams, and J. P. Armitage. *Rhodobacter sphaeroides*: complexity in chemotactic signalling. *Trends Microbiol.*, 16:251–260, 2008.
- [68] K. Prasad, S. R. Caplan, and M. Eisenbach. Fumarate modulates bacterial flagellar rotation by lowering the free energy difference between the clockwise and counterclockwise states of the motor. *J. Mol. Biol.*, 280:821–828, 1998.
- [69] E. M. Purcell. Life at low Reynolds number. *Am. J. Phys.*, 45:3–11, 1977.
- [70] E. M. Purcell. The efficiency of propulsion by a rotating flagellum. *Proc. Natl. Acad. Sci. USA*, 94:11307–11311, 1997.
- [71] A. D. T. Samuel and H. C. Berg. Fluctuation analysis of rotational speeds of the bacterial flagellar motor. *Proc. Natl. Acad. Sci. USA*, 92:3502–3506, 1995.
- [72] B. E. Scharf, K. A. Fahrner, L. Turner, and H. C. Berg. Control of direction of flagellar rotation in bacterial chemotaxis. *Proc. Natl. Acad. Sci. USA*, 95:201–206, 1998.

- [73] M. J. Schnitzer, S. M. Block, H. C. Berg, and E. M. Purcell. Strategies for chemotaxis. *Symp. Soc. Gen. Microbiol.*, 46:15–34, 1990.
- [74] J. E. Segall, S. M. Block, and H. C. Berg. Temporal comparisons in bacterial chemotaxis. *Proc. Natl. Acad. Sci. USA*, 83:8987–8991, 1986.
- [75] M. Silverman and M. Simon. Flagellar rotation and the mechanism of bacterial motility. *Nature*, 249:73–74, 1974.
- [76] R. E. Sockett, J. P. Armitage, and M. C. W. Evans. Methylation-independent and methylation-dependent chemotaxis in *Rhodobacter sphaeroides* and *Rhodospirillum rubrum*. *J. Bacteriol.*, 169:5808–5814, 1987.
- [77] V. Sourjik and H. C. Berg. Binding of the *Escherichia coli* response regulator CheY to its target measured *in vivo* by fluorescence resonance energy transfer. *Proc. Natl. Acad. Sci. USA*, 99:12669–12674, 2002.
- [78] V. Sourjik and H. C. Berg. Functional interactions between receptors in bacterial chemotaxis. *Nature*, 428:437–441, 2004.
- [79] Y. Sowa, H. Hotta, M. Homma, and A. Ishijima. Torque-speed relationship of the Na<sup>+</sup>-driven flagellar motor of *Vibrio alginolyticus*. *J. Mol. Biol.*, 327:1043–1051, 2003.
- [80] M. S. Springer, M. F. Goy, and J. Adler. Protein methylation in behavioural control mechanisms and in signal transduction. *Nature*, 280:279–284, 1979.
- [81] J. L. Spudich and D. E. Koshland, Jr. Quantitation of the sensory response in bacterial chemotaxis. *Proc. Natl. Acad. Sci. USA*, 72:710–713, 1975.
- [82] R. C. Stewart, K. Jahreis, and J. S. Parkinson. Rapid phosphotransfer to CheY from a CheA protein lacking the CheY-binding domain. *Biochemistry*, 39:13157–13165, 2000.
- [83] A. M. Stock, V. L. Robinson, and P. N. Goudreau. Two-component signal transduction. *Annu. Rev. Biochem.*, 69:183–215, 2000.
- [84] J. B. Stock, A. M. Stock, and J. M. Mottonen. Signal transduction in bacteria. *Nature*, 344:395–400, 1990.
- [85] Y. Takano, K. Yoshida, S. Kudo, M. Nishitoba, and Y. Magariyama. Analysis of small deformation of helical flagellum of swimming *Vibrio alginolyticus*. *JSME International Journal, Series C*, 46:1241–1247, 2003.
- [86] Y. Tu, T. S. Shimizu, and H. C. Berg. Modeling the chemotactic response of *Escherichia coli* to time-varying stimuli. *Proc. Natl. Acad. Sci. USA.*, 105:14855–14860, 2008.
- [87] L. Turner, S. R. Caplan, and H. C. Berg. Temperature-induced switching of the bacterial flagellar motor. *Biophys. J.*, 71:2227–2233, 1996.

- [88] L. Turner, W. S. Ryu, and H. C. Berg. Real-time imaging of fluorescent flagellar filaments. *J. Bacteriol.*, 182:2793–2801, 2000.
- [89] A. Vaknin and H. C. Berg. Single-cell FRET imaging of phosphatase activity in the *Escherichia coli* chemotaxis system. *Proc. Natl. Acad. Sci. USA*, 101:17072–17077, 2004.
- [90] G. H. Wadhams and J. P. Armitage. Making sense of it all: bacterial chemotaxis. *Nat. Rev. Mol. Cell Bio.*, 5:1024–1037, 2004.
- [91] X. L. Wu, T. Altindal, and L. Xie. Bacterial diffusivity of a three-step swimmer (unpublished).
- [92] L. Xie, T. Altindal, S. Chattopadhyay, and X. L. Wu. Bacterial flagellum as a propeller and as a rudder for efficient chemotaxis. *Proc. Natl. Acad. Sci. USA*, 108:2246–2251, 2011.
- [93] T. M. Yi, Y. Huang, M. I. Simon, and J. Doyle. Robust perfect adaptation in bacterial chemotaxis through integral feedback control. *Proc. Natl. Acad. Sci. USA*, 97:4649–4653, 2000.
- [94] J. Yuan, K. A. Fahrner, and H. C. Berg. Switching of the bacterial flagellar motor near zero load. *J. Mol. Biol.*, 390:394–400, 2009.
- [95] J. Yuan, K. A. Fahrner, L. Turner, and H. C. Berg. Asymmetry in the clockwise and counterclockwise rotation of the bacterial flagellar motor. *Proc. Natl. Acad. Sci. USA*, 107:12846–12849, 2010.